Density Fluctuations and Machine Learning in Active Matter

Thesis by
Austin Dulaney

In Partial Fulfillment of the Requirements for the
Degree of
Doctor of Philosophy in Chemical Engineering

CALIFORNIA INSTITUTE OF TECHNOLOGY
Pasadena, California

2021
Defended December 16, 2020

© 2021

Austin Dulaney
ORCID: 0000-0002-2428-8913

All rights reserved.

ACKNOWLEDGEMENTS

First and foremost, I would like to thank my advisor, John Brady. John's physical insight and mathematical prowess are unmatched, and I have been privileged to work alongside him. I am exceptionally grateful for his unending professionalism, his open-mindedness, and genial demeanor. I am most grateful for his encouragement and fostering of my independence as a researcher as it allowed me to dramatically shape my own development.

I would like to thank the members of my thesis committee: Tom Miller, Julie Kornfield, and Rick Flagan. I thank Professor Miller for his support and enthusiasm towards my research; his genuine excitement has been a continual source of encouragement. I thank Professor Kornfield for her passion and for challenging me as a researcher to adequately defend my work. Lastly, I thank Professor Flagan for his service as my committee chair and for helping me consider how my work relates to an experimental context.

I owe a special thanks to the Chemical Engineering staff who keep the department running, for making my time at Caltech substantially easier. I would like to thank Martha Hepworth for helping me keep track of everyone in the Brady group and our resources. I thank Suresh Guptha for being a constant source of enjoyable conversation ranging from computers to our monthly fitness goals. Without his help, I would not have been able to rebuild the Brady group's computational resources. I want to give a special thanks to Allison Kinard for being incredibly helpful with all of my endeavors, acting as a sounding board, and being such a compassionate individual. The care and commitment she shows to the department are truly remarkable and the students benefit dramatically from her presence.

My time in John's group was vastly more enjoyable thanks to Eric Burkholder, Kevin Marshall, Charlie Slominski, Sho Takatori, Camilla Kjeldbjerg, Stewart Mallory, Zhiwei Peng, Hyeongjoo Row, and Alec Glisman. Eric's grounded nature helped keep me level in times of distress and tempered my loftier expectations. I would also like to thank our visitors Dr. Mario Sandoval and Karol Makuch. Karol once told me that coffee was the best tool for a scientist as it fosters discussion and community. Many of my best discussions on life and statistical physics took place with Karol over a cup of coffee early in the morning, and these are memories I will cherish. Ahmad Omar and Stewart Mallory were wonderful office mates who filled my life

with countless discussions on science, life, entertainment, music, etc. They are both terrific friends and mentors who truly made my office an exceptional place to work.

Above all, I would like to thank the friends I've made at Caltech as they have become like family to me. Thank you, Tina and Brad Boville, for being such supportive friends. My time here would not have been the same without you. I want to thank Patrick Almjhell for introducing me to the sport of snowboarding and for getting me involved in rock climbing, an activity that has become a strong passion of mine. I would like to thank Bruce Wittmann for being a loyal friend and exercise partner throughout my time at Caltech and for being a source of interesting scientific discussion. I would also like to thank Anders Knight, Silken Jones, and Nick Porter for being incredible people and joining me on many adventures.

Thank you to my family for their love and support. Thank you, Brantley Henson, for seeing the potential in me and for encouraging me to continue to push myself. Thank you, Todd and Allison, for welcoming me into your family. Thank you Mom and Dad for listening to me complain about work, for believing in me, and for showing your love.

To Ella Watkins-Dulaney—my partner, most avid supporter, and best friend—I owe all of my accomplishments and successes at Caltech. Thank you for your undying love and support even when times were hard. I can't express how much I appreciate you and how proud I am to be your partner.

ABSTRACT

Active matter is a class of materials that has constituents capable of self-propulsion through the conversion of energy into mechanical motion. The origin or specific details of their method of locomotion is a rich area of research, but is not important for understanding some aspects of their dynamics. Our interest is in the single-particle dynamics and the large-scale collective motion observed in these systems. Thus, we use the minimal active Brownian particle (ABP) model to model self-propulsion. The ABP model consists of particles of radius a that swim with an intrinsic speed U_0 in some direction $\mathbf{q}$ and reorients on a timescale τ_R. Active motion is persistent in that a particle will continue to swim in a direction until it reorients itself, giving rise to a swim or persistence length $\ell = U_0\tau_R$. This persistence leads to directed motion at short times but has been shown to become diffusive at long times with a diffusivity that originates from the random swim steps. I show that while these particles do become diffusive at steady state, they display wavelike dynamics while relaxing from an initial point source, which is shown by fluctuations in the number density. The strength of these fluctuations is determined by the ratio of the swim diffusivity to thermal diffusivity. Our resulting theory predicts these dynamics in other instances where spatial gradients in number density are present. This motivated me to look into fluctuations in interacting suspensions of ABPs by studying the “isothermal" compressibility. Our theoretical perspective and simulation results show that the compressibility behaves just like a thermodynamic response function, even though these suspensions are driven far from equilibrium. As such, the compressibility is capable of predicting the critical point for the motility induced phase separation (MIPS). We then developed a machine learning (ML) model to predict particle phase identity near the MIPS critical point in the coexistence region—where fluctuations are large—to recreate the binodal. Our successful recreation of the binodal and understanding of compressibility resulted in our attempt to define a Widom line (an extension of the coexistence line) for ABPs. The Widom line is the collection of points where density fluctuations are maximized and marks where supercritical behavior goes from being more gas-like to more liquid-like. I conclude by discussing current works in progress to further our understanding of the MIPS transition by using ML to identify particles in the interface of the coexisting phases. From the work on compressibility, we believe the interface plays a crucial role in describing active phase behavior.

PUBLISHED CONTENT AND CONTRIBUTIONS

[1] A. R. Dulaney and J. F. Brady, “Waves in active matter: The transition from ballistic to diffusive behavior”, Phys. Rev. E **101**,
A.R.D. participated in the conception of the project, performed the calculations, analyzed the data, performed the simulations, and participated in the writing of the manuscript., 052609 (2020),
DOI:10.1103/PhysRevE.101.052609.

[2] A. R. Dulaney and J. F. Brady, “Machine Learning for Phase Behavior in Active Matter Systems”,
A.R.D. participated in the conception of the project, developed the models, analyzed the data, and participated in the writing of the manuscript. (2020),
arxivId:2011.09458.

[3] A. R. Dulaney, S. A. Mallory, and J. F. Brady, “The "isothermal" compressibility of active matter”,
A.R.D. participated in the conception of the project, performed the calculations, analyzed the data, and participated in the writing of the manuscript. (2020),
arxivId:2009.11439.

TABLE OF CONTENTS

LIST OF ILLUSTRATIONS

LIST OF TABLES

Chapter 1

INTRODUCTION

This introductory chapter provides an overview of the basic concepts related to active systems and their vast array of applications. We outline some of the open questions which motivated this work and provide the necessary background to begin to answer these questions. Subsequent chapters present our theoretical developments, computational evidence, and machine learning frameworks which motivate our continuum and molecular perspectives on fluctuations and phase behavior in colloidal-scale active matter systems.

1.1 Active Matter

The foundation of motion—whether in an artificial or biological context—is rooted in mechanics. The distinction between motion in biological and artificial systems is not predicated on the context of life but rather results from the method of locomotion used by constituents of each system. Active matter is a class of materials in which the constituents undergo self-propulsion by converting energy into mechanical motion through some internal physicochemical processes. This generates internal stresses driving the system far from equilibrium (in the absence of applied external forces) [1] and results in a myriad of interesting phenomena such as spontaneous self-assembly [2–6], phase separation [7–9], and other emergent collective behavior [10–14]. Active matter spans a large range of length scales from bacteria and colloidal Janus particles to flocks of birds and schools of fish. We will focus on those at the colloidal scale. (Some examples of which are depicted in Fig. 1.1.) These driven systems have become increasingly enticing to biologists, chemists, material scientists, and engineers alike for their potential to perform autonomous work [15], assist in drug delivery [16, 17], and clean environmental hazards [18–25].

1.2 Active Dynamics

The distinction between colloidal-scale active matter and its passive counterpart results from the differences in the forces that drive their motion. While passive colloidal particles are driven strictly by thermal motion (in the absence of external forces), active colloids possess an additional driving force from their internally generated activity. This can be modeled simply using the minimal active Brownian particle (ABP) model, where a particle of radius a swims in direction $\mathbf{q}$ with an intrinsic speed U_0 and reorients itself on a timescale τ_R. An example of this model is depicted in Fig. 1.2.

This active motion is persistent since the particle will swim consistently in one direction until it reorients itself, giving rise to a persistence or run length $\ell = U_0\tau_R$. Active reorientation can be modeled as a stochastic process governed by some rotary diffusivity $D_R = \tau_R^{-1}$, similar to rotational Brownian motion though it need not be thermal in origin. The propulsion direction creates an asymmetry in the particle, even if the body itself is symmetric. At short times the active swimming motion is directed, but if we look at sufficiently long timescales $t \gg \tau_R$, each run length looks like a step in a random walk process and the motion becomes diffusive with diffusivity $D^{swim} = U_0^2\tau_R/[d(d-1)]$ where d is the number of rotational dimensions [27–29]. We can then define an energy scale—in analogy to thermal energy—for

the activity $k_s T_s = \zeta D^{swim}$ using a Stokes-Einstein-Sutherland relationship [27, 30]. This gives rise to dimensionless parameters not seen in passive systems through a ratio of energy scales $k_s T_s / k_b T$ or through a ratio of length scales $Pe_R \equiv a/\ell$, which measure how active or persistent the system is, respectively.

From this model, we can provide a microscopic framework to describe particle dynamics by using the overdamped Langevin equations for the forces and torques in the system. At the colloidal scale, self-propelled particles are in the Stokes regime, meaning that inertial forces are dominated by viscous forces in the equations of motion. This results in force-free ($\sum \mathbf{F} = \mathbf{0}$) and torque-free ($\sum \mathbf{L} = \mathbf{0}$) motion. The forces acting on an ABP are balanced by the drag force $0 = \mathbf{F}^{drag} + \mathbf{F}^{swim} + \mathbf{F}^{B}$, where $\mathbf{F}^{swim} = \zeta U_0 \mathbf{q}$ is the swim force, $\mathbf{F}^{B}$ is the Brownian force, and ζ is the translational drag coefficient [29]. The torques acting on an ABP are $0 = \mathbf{L}^{drag} + \mathbf{L}^{R}$, where the drag torque is balanced by the stochastic rotary torque from activity. This stochastic torque can be the thermally driven Brownian torque or can come from an alternative internal mechanism (such as the unwinding and bundling of flagella seen in some biological systems).

A probabilistic description of the active dynamics is provided by the Smoluchowski equation in position and orientation space [31–34]:

$$\frac{\partial P}{\partial t} + \nabla \cdot \mathbf{j}_T + \nabla_R \cdot \mathbf{j}_R = 0, \tag{1.1}$$

where $P(\mathbf{x}, \mathbf{q}, t)$ is the probability distribution for a particle being located at position $\mathbf{x}$ with orientation $\mathbf{q}$ at time t, $\mathbf{j}_T$ is the translational flux, $\mathbf{j}_R$ is the rotational flux, and $\nabla_R = \mathbf{q} \times \nabla_q$ is the appropriate rotational gradient operator. For the simple case of ABPs with no external forces or torques, we use constitutive laws for the translational flux $\mathbf{j}_T = U_0 \mathbf{q} P - D_T \nabla P$ and rotational flux $\mathbf{j}_R = -\tau_R^{-1} \nabla_R P$, with thermal diffusivity D_T giving an exact descroption for ideal ABPs.

Even in the simplest cases, Eq. (1.1) is not analytically tractable and must be solved either numerically or through approximations. If one averages the probability density over the orientations at steady-state, we see that the resulting equation for the number density takes on the form of an advection-diffusion equation. This advection-diffusion equation shows that active motion does become diffusive at long times [34, 35].

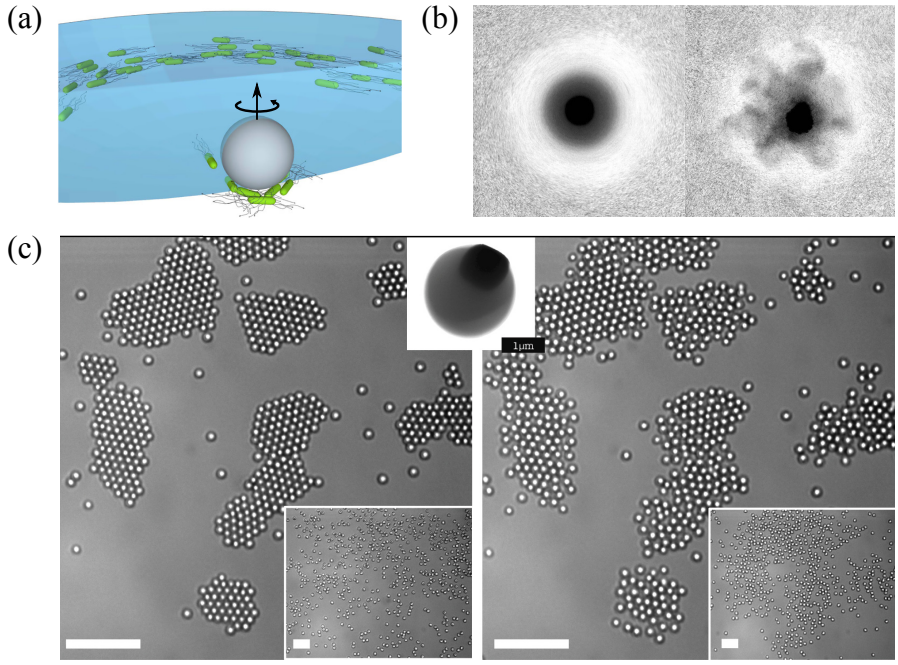

Figure 1.1: (**a**) A schematic of motile bacteria *Bacillus subtilis* swimming around a rotating particle [26]. (**b**) Stable bacterial concentration around the rotating particle (left) and the concentration one second after cessation of rotation (right) (adapted from Sokolov et al. [26]). (**c**) A suspension of light-activated, synthetic colloidal hematite particles (middle inset) forming clusters while active (left) and melting when activity is turned off (right) (adapted from Palacci et al. [8]).

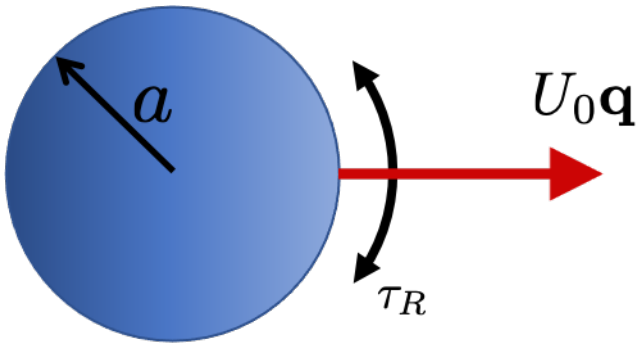

Figure 1.2: An active Brownian particle of size a that swims with speed U_0 in direction $\mathbf{q}$ and reorients itself on a timescale τ_R.

1.3 Motility-Induced Phase Separation

In addition to altering dynamic behavior, the persistent nature of active motion gives rise to additional stresses. An ABP confined to a given volume will push against the containing wall until it reorients and swims away from the boundary. While it is oriented towards the container boundary it is imparting its swim force on the wall generating a novel pressure, the swim pressure [27–29, 36]. The swim pressure $\Pi^{swim} = n\zeta U_0^2 \tau_R$ is the trace of the swim stress $\boldsymbol{\sigma}^{swim} = -n\langle \mathbf{x}\mathbf{F}^{swim} \rangle$ (the first moment of the force), where $\mathbf{x}$ is the absolute position of the particle [27, 36].

If activity is sufficiently large and the suspension is dense enough, then active particles will spontaneously separate into a dense and dilute phase, even in the absence of attractive forces [7, 8, 10, 14, 30]. This motility-induced phase separation (MIPS) results solely from the activity, but it is strikingly similar to vapor-liquid coexistence seen in traditional equilibrium fluids. These similarities have led to a large push from the active matter community to characterize this active phase behavior by building phase diagrams [30, 37–42] and constructing nonequilibrium thermodynamic frameworks for active matter [30, 42–46]. An example of the MIPS phase diagram for two-dimensional ABPs on the $Pe_R - \phi$ plane is presented in the bottom of Fig. 1.3, where $Pe_R \equiv a/\ell$ is the ratio of length scales mentioned in section 1.2 and $\phi = n\pi a^2$ is the packing fraction in two dimensions. The top portion of the figure shows representative snapshots of Brownian dynamic (BD) simulations at labeled parts of the phase diagram: (a) dense, (b) dilute, (c) near critical, and (d) deep within the coexistence region.

While special attention has focused on thermodynamic analogues to quantities such as entropy [30, 47, 48] and chemical potential [30, 43, 45], there is still debate as to whether the current *definitions* are correct. For example, a chemical potential can be defined for active systems and accurately describes the homogeneous supercritical region, but it implies a Maxwell construction that overestimates the coexistence pressure in the two-phase region [30], requiring alternative criterion for determining coexistence [49]. Few studies extend beyond the coexistence region and focus on the supercritical behavior of active systems to better characterize these systems through critical phenomena and scaling exponents [50, 51] or through understanding response functions [52].

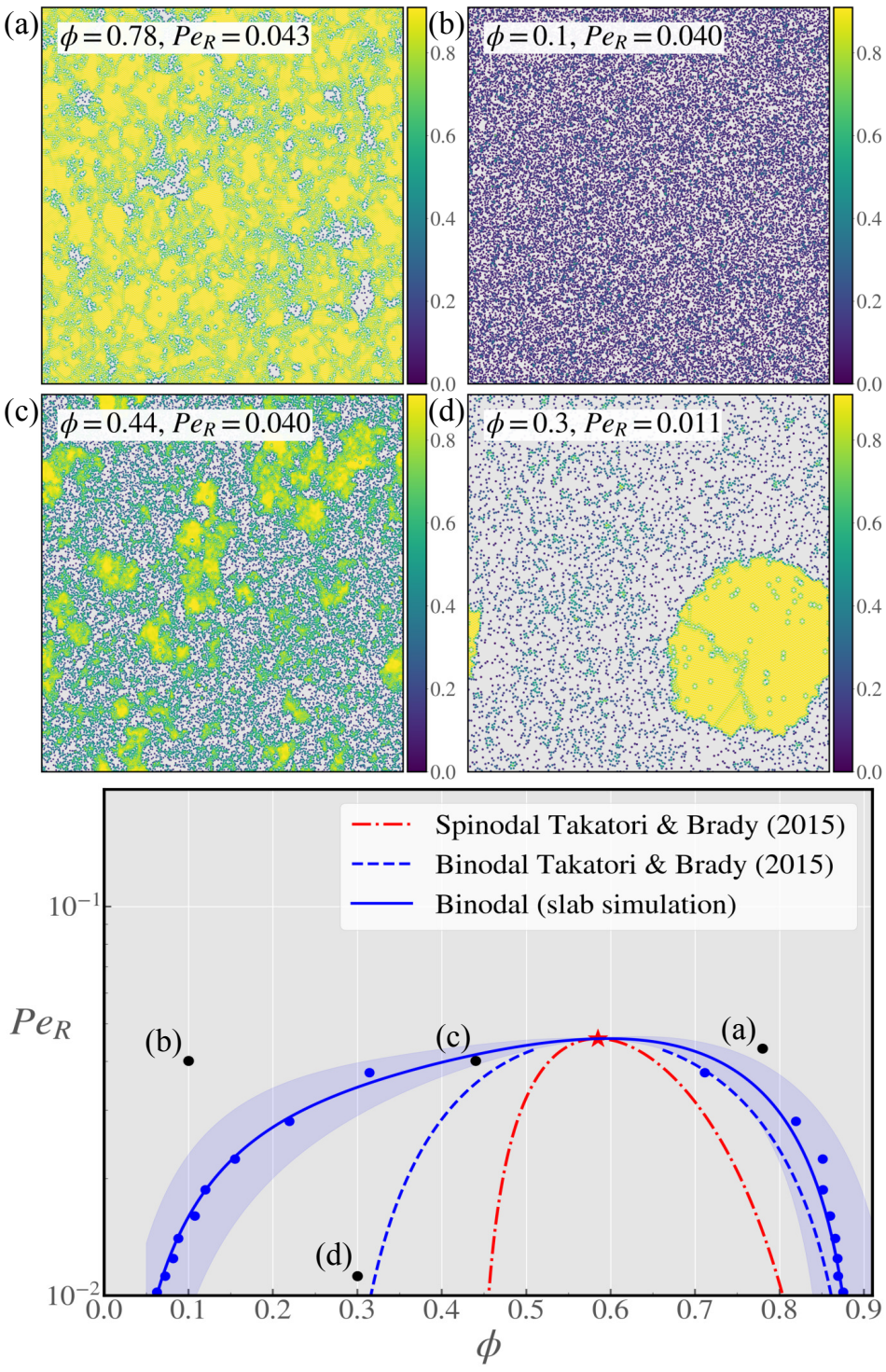

Figure 1.3: The active matter phase diagram (**Bottom**) for motility-induced phase separation on the $Pe_R - \phi$ plane. The spinodal (dashed red) and binodal (dashed blue) from Takatori and Brady [30] are shown along with the binodal computed from slab simulations (blue solid). The labeled points correspond to simulation snapshots (**Top**) at different points of the phase diagram.

1.4 Machine Learning in the Physical Sciences

Machine learning is widely used in computer vision, recommendation systems, and autonomous applications [53–57]. Recently, machine learning has grown in popularity in the physical sciences as well [58–66] thanks to its ability to find complex nonlinear correlations between system variables and learn patterns. Developments in deep learning methodologies like convolutional neural networks (CNNs) and graphical neural networks (GNNs) have made it possible to draw information from spatial structure in data. This makes machine learning an enticing tool for studies in phase behavior [58, 62, 63, 67, 68]. The motility-induced phase transition in active matter is difficult to predict using traditional means due to the fact that these systems are far-from-equilibrium and traditional thermodynamic frameworks do not apply. Additionally, it can be difficult to obtain analytic solutions for the dynamics in these systems due to the active motion. Machine learning provides a way to overcome these obstacles and gain insights into collective behavior through understanding single particle features and local spatial structure.

1.5 Thesis Outline

In Chapter 2 of this thesis, I present our theoretical framework for predicting the unique interplay between active and thermal motion in the relaxation behavior of active colloidal suspensions. Using a simple theoretical model, we study the classical problem of diffusion from a point source to better understand how directed active motion affects short-time dynamics in active Brownian systems. We show that activity results in wavelike dynamics at short times (see Fig. 2.3). Our theoretical framework captures the ballistic motion at short times and the transition to diffusive motion on timescales greater than the reorientation time. We corroborate our theory with Brownian dynamic simulations and further investigate how this transition can be delayed through the application of an external orienting field. We have shown that the orientation autocorrelation is the dominant factor in producing wavelike dynamics. The ballistic nature is dampened out as particle orientation begins to decorrelate. As such, we find that the orientation can be recorrelated through instantaneous density fluctuations—as is the case in the diffusion from a point source and formation of noncritical nuclei in MIPS.

We expand on the notion of density fluctuations in Chapter 3 by shifting focus to the compressibility of active systems. Using large-scale computer simulations our study reveals that compressibility behaves like a “thermodynamic” response function in active systems. Here, we show that compressibility computed via the mechanical

definition or through the structure of the suspension is identical, as is the case for equilibrium suspensions. We develop an active equivalent to the compressibility equation via the collective diffusivity which gives our relationship between compressibility and suspension structure. The equivalence in compressibility definitions lends support to the notion of an analogue to chemical potential and subsequently, free energy in active systems. It is known that a chemical potential derived via the Gibbs-Duhem equation does not yield the correct coexistence pressure for MIPS, but this does not preclude the existence of an alternative relationship between free energy and compressibility.

The divergence of the compressibility near the critical point motivated us to examine the coexistence region of MIPS near the critical point. In Chapter 4, I use machine learning to predict which phase a particle belongs to in the coexistence region. Taking structural and dynamic particle quantities gives information to determine the phase identity and ultimately allow for the recreation of the binodal of the MIPS transition. Our method uses graph-based learning to incorporate local structure into our prediction allowing for more confident predictions in the region near the critical point where density fluctuations are large. The machine-learned binodal is compared to the binodal computed from slab simulations and illustrates that the local state of a particle can be determined in this fashion.

In Chapter 5, I present the Widom line in active systems, which marks the extension of the coexistence curve into the supercritical region. In equilibrium fluids, the Widom line is defined as the collection of points of maximum isothermal compressibility. I use computer simulations and our results from Chapter 3 to compute the Widom line from our definition for “isothermal" compressibility, defined from pressure and the fluid structure. The Widom line in equilibrium Lennard-Jones fluids can additionally be defined as the collection of points of equal phase fraction. From this perspective, the supercritical fluid is treated as a heterogeneous mixture of liquid-like and gas-like microphases, and the point of equal phase fraction corresponds to a maximum in the density fluctuations. We compare this to the behavior in active suspensions using a machine learning model, similar to that used in Chapter 4. We use a nonequilibrium free energy argument to motivate what the balance of phases should be for active systems and present the Widom line predicted from our machine learning algorithm.

Finally, in Chapter 6 I conclude with my work studying the contribution of the interface to MIPS. I extend our machine learning framework from Chapter 4 to

predict which particles are a part of the phase interface for suspensions below the MIPS critical point—in the coexistence region. From Chapter 3, we have evidence to suspect that the interface is important for developing an accurate binodal. This idea is further developed through a flux argument showing the necessary contribution of the swim pressure. I present some initial predictions which show our progress in capturing interfacial particles. I conclude by discussing the remaining steps necessary to validate this work.

References

[1] S. Ramaswamy, "The Mechanics and Statistics of Active Matter", en, Annual Review of Condensed Matter Physics **1**, 323–345 (2010).

[2] S. Ebbens, R. A. L. Jones, A. J. Ryan, R. Golestanian, and J. R. Howse, "Self-assembled autonomous runners and tumblers", en, Physical Review E **82**, 015304 (2010).

[3] S. A. Mallory and A. Cacciuto, "Activity-assisted self-assembly of colloidal particles", Physical Review E **94** (2016).

[4] G. S. Redner, C. G. Wagner, A. Baskaran, and M. F. Hagan, "Classical Nucleation Theory Description of Active Colloid Assembly", Physical Review Letters **117**, 1–7 (2016).

[5] S. A. Mallory and A. Cacciuto, "Activity-Enhanced Self-Assembly of a Colloidal Kagome Lattice", Journal of the American Chemical Society **141**, 2500–2507 (2019).

[6] A. K. Omar, Y. Wu, Z.-g. Wang, and J. F. Brady, "Swimming to Stability : Structural and", ACS Nano **13**, 560–572 (2018).

[7] Y. Fily and M. C. Marchetti, "Athermal Phase Separation of Self-Propelled Particles with No Alignment", Physical Review Letters **108**, 235702 (2012).

[8] J. Palacci, S. Sacanna, A. P. Steinberg, D. J. Pine, and P. M. Chaikin, "Living Crystals of Light-Activated Colloidal Surfers", en, Science **339**, 936–940 (2013).

[9] G. Liu, A. Patch, F. Bahar, D. Yllanes, R. D. Welch, M. C. Marchetti, S. Thutupalli, and J. W. Shaevitz, "Self-Driven Phase Transitions Drive Myxococcus xanthus Fruiting Body Formation", Physical Review Letters **122**, 248102 (2019).

[10] F. Ginelli, F. Peruani, M. Bär, and H. Chaté, "Large-scale collective properties of self-propelled rods", Physical Review Letters **104**, 1–4 (2010).

[11] S. Ebbens, "Active colloids: Progress and challenges towards realising autonomous applications", Current Opinion in Colloid & Interface Science **21**, 14–23 (2016).

[12] A. Zöttl and H. Stark, "Emergent behavior in active colloids", Journal of Physics: Condensed Matter **28**, 253001 (2016).

[13] L. Barberis and F. Peruani, "Large-Scale Patterns in a Minimal Cognitive Flocking Model: Incidental Leaders, Nematic Patterns, and Aggregates", Physical Review Letters **117**, 248001 (2016).

[14] C. Bechinger, R. Di Leonardo, H. Löwen, C. Reichhardt, G. Volpe, and G. Volpe, "Active Particles in Complex and Crowded Environments", Reviews of Modern Physics **88**, 045006 (2016).

[15] R. Di Leonardo, L. Angelani, D. Dell'Arciprete, G. Ruocco, V. Iebba, S. Schippa, M. P. Conte, F. Mecarini, F. De Angelis, and E. Di Fabrizio, "Bacterial ratchet motors", Proceedings of the National Academy of Sciences **107**, 9541–9545 (2010).

[16] W. Gao, R. Dong, S. Thamphiwatana, J. Li, L. Zhang, and J. Wang, "Artificial Micromotors in the Mouse's Stomach: A Step toward in Vivo Use of Synthetic Motors", en, ACS Nano **9**, 117–123 (2015).

[17] Z. Wu, L. Li, Y. Yang, P. Hu, Y. Li, S.-Y. Yang, L. V. Wang, and W. Gao, "A microrobotic system guided by photoacoustic computed tomography for targeted navigation in intestines in vivo", Science Robotics **4**, eaax0613 (2019).

[18] O. N. Ruiz, D. Alvarez, G. Gonzalez-Ruiz, and C. Torres, "Characterization of mercury bioremediation by transgenic bacteria expressing metallothionein and polyphosphate kinase", en, BMC Biotechnology **11**, 82 (2011).

[19] R. M. Atlas and T. C. Hazen, "Oil Biodegradation and Bioremediation: A Tale of the Two Worst Spills in U.S. History", Environmental Science & Technology **45**, 6709–6715 (2011).

[20] M. Guix, J. Orozco, M. García, W. Gao, S. Sattayasamitsathit, A. Merkoçi, A. Escarpa, and J. Wang, "Superhydrophobic Alkanethiol-Coated Microsubmarines for Effective Removal of Oil", en, ACS Nano **6**, 4445–4451 (2012).

[21] W. Gao, X. Feng, A. Pei, Y. Gu, J. Li, and J. Wang, "Seawater-driven magnesium based Janus micromotors for environmental remediation †", This journal is [a] The Royal Society of Chemistry **4696**, 4696–4700 (2013).

[22] J. Orozco, V. García-Gradilla, M. D'Agostino, W. Gao, A. Cortés, and J. Wang, "Artificial Enzyme-Powered Microfish for Water-Quality Testing", en, ACS Nano **7**, 818–824 (2013).

[23] W. Gao and J. Wang, "The Environmental Impact of Micro/Nanomachines: A Review", ACS Nano **8**, 3170–3180 (2014).

[24] L. Soler and S. Sánchez, "Catalytic nanomotors for environmental monitoring and water remediation", en, Nanoscale **6**, 7175–7182 (2014).

[25] B. Jurado-Sánchez and J. Wang, "Micromotors for environmental applications: a review", en, Environmental Science: Nano **5**, 1530–1544 (2018).

[26] A. Sokolov, L. D. Rubio, J. F. Brady, and I. S. Aranson, "Instability of expanding bacterial droplets", en, Nature Communications **9**, 1322 (2018).

[27] S. C. Takatori, W. Yan, and J. F. Brady, "Swim Pressure: Stress Generation in Active Matter", en, Physical Review Letters **113**, 028103 (2014).

[28] S. C. Takatori and J. F. Brady, "Swim stress, motion, and deformation of active matter: effect of an external field", en, Soft Matter **10**, 9433–9445 (2014).

[29] W. Yan and J. F. Brady, "The force on a boundary in active matter", en, Journal of Fluid Mechanics **785**, R1 (2015).

[30] S. C. Takatori and J. F. Brady, “Towards a thermodynamics of active matter”, en, Physical Review E **91**, 032117 (2015).

[31] J. Dhont, *An Introduction to Dynamics of Colloids*, en (Elsevier, May 1996), p. 661.

[32] J. F. Brady, “Particle motion driven by solute gradients with application to autonomous motion: Continuum and colloidal perspectives”, Journal of Fluid Mechanics **667**, 216–259 (2011).

[33] D. Saintillan and M. J. Shelley, “Active suspensions and their nonlinear models”, Comptes Rendus Physique **14**, 497–517 (2013).

[34] W. Yan and J. F. Brady, “The swim force as a body force”, Soft Matter **11**, 6235–6244 (2015).

[35] A. R. Dulaney and J. F. Brady, “Waves in active matter: The transition from ballistic to diffusive behavior”, Phys. Rev. E **101**,
A.R.D. participated in the conception of the project, performed the calculations, analyzed the data, performed the simulations, and participated in the writing of the manuscript., 052609 (2020),

[36] S. C. Takatori and J. F. Brady, “Forces, stresses and the (thermo?) dynamics of active matter”, Current Opinion in Colloid & Interface Science **21**, 24–33 (2016).

[37] A. Wysocki, R. G. Winkler, and G. Gompper, “Cooperative motion of active Brownian spheres in three-dimensional dense suspensions”, EPL **105** (2014).

[38] J. Stenhammar, D. Marenduzzo, R. J. Allen, and M. E. Cates, “Phase behaviour of active Brownian particles: The role of dimensionality”, Soft Matter **10**, 1489–1499 (2014).

[39] V. Prymidis, S. Paliwal, M. Dijkstra, and L. Filion, “Vapour-liquid coexistence of an active Lennard-Jones fluid”, The Journal of Chemical Physics **145**, 124904 (2016).

[40] D. Levis, J. Codina, and I. Pagonabarraga, “Active Brownian equation of state: metastability and phase coexistence”, Soft Matter **13**, 8113–8119 (2017).

[41] B. van der Meer, V. Prymidis, M. Dijkstra, and L. Filion, “Predicting the phase behavior of mixtures of active spherical particles”, (2016).

[42] J. U. Klamser, S. C. Kapfer, and W. Krauth, “Thermodynamic phases in two-dimensional active matter”, Nature Communications **9** (2018).

[43] S. Chakraborti, S. Mishra, and P. Pradhan, “Additivity, density fluctuations, and nonequilibrium thermodynamics for active Brownian particles”, Physical Review E **93**, 052606 (2016).

[44] T. Speck, “Stochastic thermodynamics for active matter”, Epl **114** (2016).

[45] S. Paliwal, J. Rodenburg, R. Van Roij, and M. Dijkstra, "Chemical potential in active systems: Predicting phase equilibrium from bulk equations of state?", New Journal of Physics **20**, 015003 (2018).

[46] A. P. Solon, J. Stenhammar, M. E. Cates, Y. Kafri, and J. Tailleur, "Generalized thermodynamics of motility-induced phase separation: phase equilibria, Laplace pressure, and change of ensembles", New Journal of Physics **20**, 075001 (2018).

[47] C. Nardini, É. Fodor, E. Tjhung, F. van Wijland, J. Tailleur, and M. E. Cates, "Entropy Production in Field Theories without Time-Reversal Symmetry: Quantifying the Non-Equilibrium Character of Active Matter", Physical Review X **7**, 021007 (2017).

[48] D. Mandal, K. Klymko, and M. R. DeWeese, "Entropy Production and Fluctuation Theorems for Active Matter", Physical Review Letters **119**, 1–6 (2017).

[49] S. A. Mallory, A. K. Omar, and J. F. Brady, "Dynamic Overlap Concentration Scale of Active Colloids", (2020).

[50] J. T. Siebert, F. Dittrich, F. Schmid, K. Binder, T. Speck, and P. Virnau, "Critical behavior of active Brownian particles", Physical Review E **98** (2018).

[51] B. Partridge and C. F. Lee, "Critical Motility-Induced Phase Separation Belongs to the Ising Universality Class", (2019).

[52] A. R. Dulaney, S. A. Mallory, and J. F. Brady, "The "isothermal" compressibility of active matter",
A.R.D. participated in the conception of the project, performed the calculations, analyzed the data, and participated in the writing of the manuscript. (2020),

[53] A. Voulodimos, N. Doulamis, A. Doulamis, and E. Protopapadakis, "Deep Learning for Computer Vision: A Brief Review", (2018).

[54] A. Singhal, P. Sinha, and R. Pant, *Use of Deep Learning in Modern Recommendation System: A Summary of Recent Works*, tech. rep. 7 (2017), pp. 975–8887.

[55] A. Da'u and N. Salim, "Recommendation system based on deep learning methods: a systematic review and new directions", Artificial Intelligence Review **53**, 2709–2748 (2020).

[56] D. Nakhaeinia, S. H. Tang, S. B. Mohd Noor, and O. Motlagh, "A review of control architectures for autonomous navigation of mobile robots", International Journal of the Physical Sciences **6**, 169–174 (2011).

[57] J. Rosenzweig and M. Bartl, *THE MAKING-OF INNOVATION, E-JOURNAL makingofinnovation A Review and Analysis of Literature on Autonomous Driving*, tech. rep. ().

[58] J. Carrasquilla and R. G. Melko, "Machine learning phases of matter", Nature Physics **13**, 431–434 (2017).

[59] M. P. Brenner, J. D. Eldredge, and J. B. Freund, "Perspective on machine learning for advancing fluid mechanics", Physical Review Fluids **4**, 100501 (2019).

[60] H. Jeckel, E. Jelli, R. Hartmann, P. K. Singh, R. Mok, J. F. Totz, L. Vidakovic, B. Eckhardt, J. Dunkel, and K. Drescher, "Learning the space-time phase diagram of bacterial swarm expansion", Proceedings of the National Academy of Sciences **116**, 1489–1494 (2019).

[61] Q. Ni, M. Tang, Y. Liu, and Y.-C. Lai, "Machine learning dynamical phase transitions in complex networks", Physical Review E **100** (2019).

[62] L. Cheng, N. B. Kovachki, M. Welborn, and T. F. Miller, *Regression-clustering for Improved Accuracy and Training Cost with Molecular-Orbital-Based Machine Learning*, tech. rep. (2019).

[63] K. Swanson, S. Trivedi, J. Lequieu, K. Swanson, and R. Kondor, "Deep learning for automated classification and characterization of amorphous materials", Soft Matter **16**, 435–446 (2020).

[64] Z. Qiao, M. Welborn, A. Anandkumar, F. R. Manby, and T. F. Miller Iii, *OrbNet: Deep Learning for Quantum Chemistry Using Symmetry-Adapted Atomic-Orbital Features*, tech. rep. ().

[65] Z. Qiao, F. Ding, M. Welborn, P. J. Bygrave, D. G. A. Smith, A. Anandkumar, F. R. Manby, and T. F. Miller, "Multi-task learning for electronic structure to predict and explore molecular potential energy surfaces", (2020).

[66] A. L. Ferguson, J. Hachmann, T. F. Miller, and J. Pfaendtner, "The Journal of Physical Chemistry A/B/C Virtual Special Issue on Machine Learning in Physical Chemistry", The journal of physical chemistry. B **124**, 9767–9772 (2020).

[67] E. P. L. van Nieuwenburg, Y.-H. Liu, and S. D. Huber, "Learning phase transitions by confusion", Nature Physics **13**, 435–439 (2017).

[68] A. R. Dulaney and J. F. Brady, "Machine Learning for Phase Behavior in Active Matter Systems",
A.R.D. participated in the conception of the project, developed the models, analyzed the data, and participated in the writing of the manuscript. (2020),

Chapter 2

WAVES IN ACTIVE MATTER: THE TRANSITION FROM BALLISTIC TO DIFFUSIVE BEHAVIOR

We highlight the unique wavelike character observed in the relaxation dynamics of active systems via a Smoluchowski based theoretical framework and Brownian dynamic simulations. Persistent swimming motion results in wavelike dynamics until the advective swim displacements become sufficiently uncorrelated, at which point the motion becomes a random walk process characterized by a swim diffusivity, $D^{swim} = U_0^2\tau_R/(d(d-1))$, dependent on the speed of swimming U_0, reorientation time τ_R, and reorientation dimension d. This change in behavior is described by a telegraph equation, which governs the transition from ballistic wave-like motion to long-time diffusive motion. We study the relaxation of active Brownian particles (ABPs) from an instantaneous source, and provide an explanation for the nonmonotonicity observed in the intermediate scattering function (ISF). Using our simple kinetic model we provide the density distribution for the diffusion of active particles released from a line source as a function of time, position, and the ratio of the activity to thermal energy. We extend our analysis to include the effects of an external field on particle spreading to further understand how reorientation events in the active force vector affect relaxation. The strength of the applied external field is shown to be inversely proportional to the decay of the wavelike structure. Our theoretical description for the evolution of the number density agrees with BD simulation data.

This chapter includes content from our previously published article:

[1] A. R. Dulaney and J. F. Brady, "Waves in active matter: The transition from ballistic to diffusive behavior", Phys. Rev. E **101**,
A.R.D. participated in the conception of the project, performed the calculations, analyzed the data, performed the simulations, and participated in the writing of the manuscript., 052609 (2020),

2.1 Introduction

Active systems have garnered significant attention for their interesting phenomena such as motility induced phase separation and spontaneous self-assembly [1, 2]. While much work has been done to study the steady-state behavior of active systems, the time dependent nature of these systems and the interplay between their modes of relaxation have not been studied in as much detail. Foundational work related to this topic has been established [3–5], but with a focus on the intermediate scattering function (ISF) [6–9]. Here, we focus on the fundamental difference in the relaxation of active systems compared to their passive counterparts and how activity alters the characteristics of their short time dynamics. The persistent swimming motion of active particles results in fundamentally different modes of relaxation, which leads to interesting phenomena not present in either purely advective or diffusive systems.

The initial relaxation response of a confined active system results in a ballistic explosion, as observed by Takatori *et al.* [5]. When active Janus particles are released from a trap they initially explode outward and eventually become diffusive after several reorientation times. The initial directed motion results in a shock wave in density that radiates outward from the trap until the persistent swimming motion becomes uncorrelated. This wave motion is a direct result of the swimming and is present in all active systems.

In simple passive colloidal systems, thermal diffusion is the only relaxation mode. However, for active colloidal particles there is an additional mechanism that originates from the activity. When probing times less than the timescale for reorientation of an active particle there is a directed and nonzero average for the active propulsive force. Since the reorientation process is stochastic, at times long compared to the reorientation timescale the active force has zero mean and the ballistic motion becomes diffusive and scales with the thermal energy plus the activity [10].

In this chapter we bring to light the inherent wavelike behavior exhibited by active systems relaxing from perturbed states and provide a fundamental explanation for this phenomena, as well as its mathematical origins. In Sec. 2.2 we provide a general theoretical framework for describing active relaxation. In Sec. 2.3 & 2.4 we apply the theory for the release of active Brownian particles (ABPs) from an instantaneous source in the limit of strong activity and when the thermal energy scale becomes comparable to the activity, respectively. Then in Sec. 2.5 we characterize the observed active waves in the presence of an external orienting field, and predict further instances of wavelike behavior in active systems. Finally, in Sec. 2.6 we

discuss the criterion necessary to observe wavelike behavior and provide concluding remarks. Our analysis and characterization focuses on dilute colloidal suspensions of ABPs that self-propel with an inherent swim speed U_0 with orientation $\mathbf{q}$ and reorient on a characteristic timescale τ_R. Interparticle and hydrodynamic interactions in the suspension are neglected in this work.

2.2 Theoretical Framework

We define a simple model for ABPs using the Smoluchowski equation for the probability distribution of particle positions and orientations. Unlike with passive, isotropic particles, the probability must be considered in positional ($\mathbf{x}$) and orientational ($\mathbf{q}$) space at each instant in time:

$$\frac{\partial P(\mathbf{x},\mathbf{q},t)}{\partial t} + \nabla\cdot\mathbf{j}^T + \nabla_R\cdot\mathbf{j}^R = 0. \tag{2.1}$$

Here, the translational and rotational fluxes are given by $\mathbf{j}^T = U_0\mathbf{q}P - D_T\nabla P$ and $\mathbf{j}^R = -D_R\nabla_R P$, respectively, where $\nabla_R = \mathbf{q}\times\nabla_q$ is the rotational gradient operator. The contributions to the translational flux are from the advective swimming motion $U_0\mathbf{q}P$ and from thermal diffusion, where the translational diffusivity is defined using the Stokes-Einstein-Sutherland relationship $D_T = k_BT/\zeta$. The rotational flux is only comprised of a diffusive piece with rotational diffusivity $D_R = 1/\tau_R$.

Analytic solutions to Eq. (2.1) are elusive, but insight into the governing phenomena and wavelike structure can be obtained by expanding the Smoluchowski equation in orientational moments [11, 12]. The first two orientational moments of Eq. (2.1) are governed by the conservation equations [13, 14]:

$$\begin{aligned}\frac{\partial n}{\partial t} + \nabla\cdot\mathbf{j}_n &= 0,\\ \mathbf{j}_n &= U_0\mathbf{m} - D_T\nabla n,\end{aligned} \tag{2.2}$$

$$\begin{aligned}\frac{\partial \mathbf{m}}{\partial t} + \nabla\cdot\mathbf{j}_m + (d-1)D_R\mathbf{m} &= 0,\\ \mathbf{j}_m &= U_0\mathbf{Q} + \frac{1}{d}U_0 n\mathbf{I} - D_T\nabla\mathbf{m},\end{aligned} \tag{2.3}$$

where $n(\mathbf{x},t) \equiv \int P(\mathbf{x},\mathbf{q},t)\,d\mathbf{q}$ is the number density, $\mathbf{m}(\mathbf{x},t) \equiv \int \mathbf{q}P(\mathbf{x},\mathbf{q},t)\,d\mathbf{q}$ is the polar-order field, $\mathbf{Q}(\mathbf{x},t) \equiv \int(\mathbf{qq} - \mathbf{I}/d)P(\mathbf{x},\mathbf{q},t)\,d\mathbf{q}$ is the nematic order field, and d is the orientational dimensionality (i.e. 2 for planar reorientations). Eqs. 2.2

and 2.3 are left as an open set of coupled equations which depend on subsequent orientational moments of $P(\mathbf{x}, \mathbf{q}, t)$. A derivation of Eqs. 2.2 and 2.3 can be found in appendix 2.7 for completeness.

Intuitively we understand that translational Brownian motion only gives rise to diffusion, which implies that the wavelike character must result from activity. Therefore to isolate this facet of particle motion we first focus on the limit of high activity relative to thermal energy, or when $D_T \to 0$. As a first order approximation we truncate the moment expansion by assuming the nematic order is isotropic, i.e. $\mathbf{Q}(\mathbf{x}, t) = 0$, thus closing the above equations. Combining Eqs. 2.2 and 2.3 gives rise to a telegraph equation

$$\frac{\partial^2 n}{\partial t^2} + \frac{(d-1)}{\tau_R}\frac{\partial n}{\partial t} = \frac{1}{d}U_0^2 \nabla^2 n. \tag{2.4}$$

For times short compared to the reorientation time τ_R, Eq. (2.4) has a wave-like character with wave speed $c = U_0/\sqrt{d}$ (similar to that obtained by Sevilla and Villarreal [9]), but for times long compared to τ_R the behavior is diffusive with the swim diffusivity $D^{swim} = U_0^2 \tau_R / d$. Eq. (2.4) in this form is similar to the model created by Alharbi and Petrovskii for population dynamics [15]. Fundamentally, ABP dynamics exhibit both wavelike behavior at short times and diffusive behavior at long times; this behavior is general for all active systems.

2.3 Waves From An Instantaneous Source

We consider the unsteady behavior of active systems from an instantaneous source. That is, we focus on observing how the density of an active system in an open domain relaxes from a localized point source disturbance back to a uniform distribution. The point source can be thought of as an instantaneous, local addition of particles to an empty domain or as a local addition of particles overtop a homogeneous background concentration of particles. This problem's historical relevance in the field of diffusion and its potential to further the understanding of bacterial film propagation on surfaces [16] make it a prime initial example for comparing relaxation in active and passive systems. For brevity we will only consider sources in two spatial dimensions as these are most experimentally relevant, but the following analyses are readily extensible to three spatial dimensions.

The Green's function for Eq. (2.4) in two dimensions with radial symmetry is

$$n(r,t) = \frac{2\theta((t-r)/\sqrt{2})}{\sqrt{t^2-r^2}} e^{-\frac{1}{2}t} \cosh\left(\frac{\sqrt{t^2-r^2}}{2}\right), \tag{2.5}$$

where $\theta(x)$ is the Heaviside function, r is the radial displacement from the source normalized by run length, $l = U_0\tau_R$, and t is time normalized by τ_R. The Green's function corresponds to the release of active particles from an instantaneous source with randomly distributed initial orientations. Number density as a function of radial displacement is shown in Fig. 2.1 at multiple time points. At short times, $t < \tau_R$, particles swim outward from the origin, which leads to a sharp peak in the density. When $t \sim \tau_R$, particles have reoriented, reducing the maximum in the density. A small fraction of particles have retained a purely outward pointing trajectory which pushes the leading edge of the density profile slightly in front of the peak. The long wake is a result of the wavelike character dominating in the short-time regime and is characteristic of symmetric wave propagation in two spatial dimensions [17]. As $t > \tau_R$ the wavefront diminishes further and the density profile more closely resembles that of a diffusive system at all points away from the leading edge. When $t \gg \tau_R$ the density profile looks diffusive (not shown) for all positions with a diffusion coefficient given by the swim diffusivity.

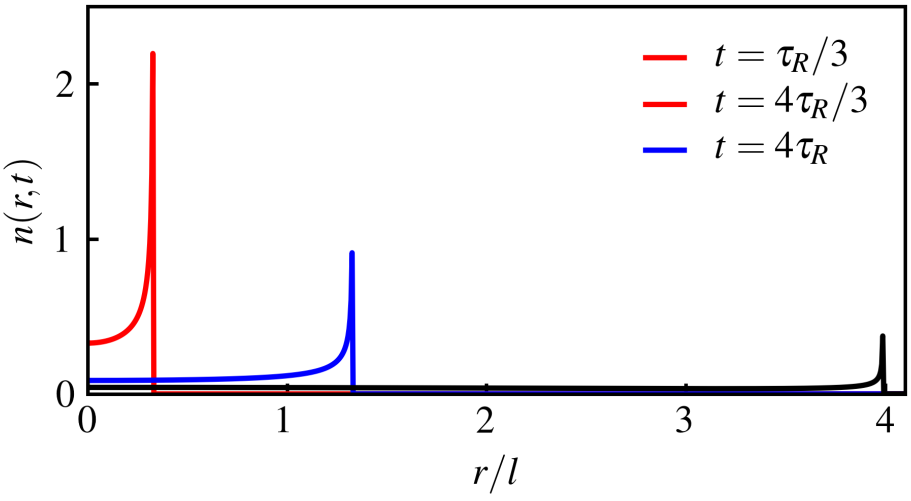

Figure 2.1: Density as a function of radial position normalized by the run length, $l = U_0\tau_R$, in the limit of $D_T \to 0$ for the telegraph equation at times $t/\tau_R = 1/3, 4/3, 4$.

Evidence of wavelike motion has been experimentally observed in systems of active Janus particles released from a two-dimensional, circular confining trap [5], but the

the experimental data implies a faster transition to diffusive dynamics. We believe the discrepancy between our simple model and these experimental data arises from the closure approximation that we have chosen, as evidenced by Fig. 2.3 in the following section. By neglecting the flux of polar order generated through nematic alignment, we have limited the diffusive character of the activity on longer timescales and thus prolonged the transition of the dynamics. This effect is exacerbated by the lack of thermal diffusion, which provides an additional mechanism through which the wavefront can relax, as will be seen in the following section. The telegraph equation shows the essential features of the ballistic to diffusive behavior [15], but it is not sufficient to quantitatively capture the transitional dynamics and is only strictly valid in the limit of high activity.

2.4 The Effects of Diffusion

In this section, we revisit the relaxation of ABPs from an instantaneous source in the limit of finite activity to examine the interplay between thermal and active energy in the short-time dynamics. We again start with Eqs. 2.2 and 2.3, but keep the translational diffusion terms. Scaling position and time by the particle run length and reorientation time respectively, gives rise to a dimensionless parameter defined by the ratio of thermal energy, k_BT to activity, $k_sT_s \equiv \zeta U_0^2\tau_R/(d(d-1))$ for $d \geq 2$ [18]. As in Section 2.2 we formulate the set of scaled conservation equations as a single expression for the number density. The telegraph structure is still readily seen by Fourier transforming in position space, but now the first order time derivative and Laplacian terms have k-dependent coefficients:

$$\frac{\partial^2\hat{n}}{\partial t^2} + f\Big(\frac{k_BT}{k_sT_s}, k\Big)\frac{\partial\hat{n}}{\partial t} = g\Big(\frac{k_BT}{k_sT_s}, k\Big)k^2\hat{n}, \tag{2.6}$$

where $\hat{n}(\mathbf{k}, t)$ is the transformed density and $\mathbf{k}$ is the dimensionless wavenumber. The spatially-dependent coefficients are

$$\begin{aligned} f &= (d-1) + \frac{2k^2}{d(d-1)}\Big(\frac{k_BT}{k_sT_s}\Big), \\ g &= \Big[1 + \frac{k_BT}{k_sT_s} + \frac{k^2}{d(d-1)^2}\Big(\frac{k_BT}{k_sT_s}\Big)^2\Big]\frac{k^2}{d}. \end{aligned} \tag{2.7}$$

The transformed number density follows as

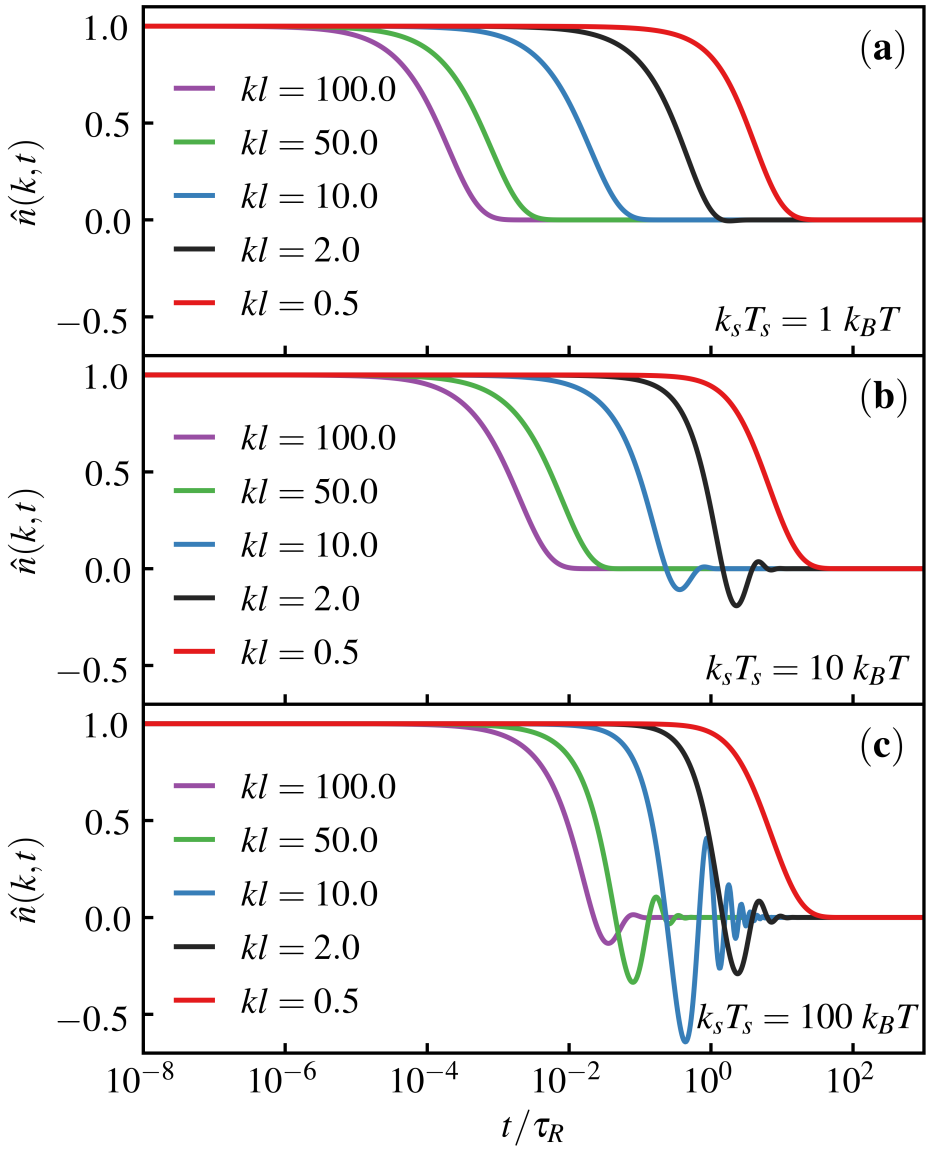

Figure 2.2: Intermediate scattering function $\hat{n}(k,t)$ of ABPs for different values of dimensionless wavenumber, kl, as a function of dimensionless time, t/τ_R for different levels of activity: **(a)** $k_sT_s = 1\ k_BT$, **(b)** $k_sT_s = 10\ k_BT$, and **(c)** $k_sT_s = 100\ k_BT$ in two orientational dimensions.

$$\hat{n} = e^{-\left(\frac{(d-1)}{2} + \frac{k^2}{d(d-1)}\frac{k_BT}{k_sT_s}\right)t}\left\{\cosh\left(\frac{(d-1)}{2}\Gamma t\right) + \frac{1}{\Gamma}\sinh\left(\frac{(d-1)}{2}\Gamma t\right)\right\}, \tag{2.8}$$

where $\Gamma = \sqrt{1 - 4k^2/(d(d-1)^2)}$. The spatially transformed density is equivalently the intermediate scattering function (ISF) as given by the Van Hove correlation [19]. Our analytic form of the ISF is similar to that obtained by Sevilla and Villarreal [9],

though we do not utilize a memory function for the active motion. There has been broad interest in obtaining the ISF for active particles both experimentally [20–22] through differential dynamic microscopy and analytically [6, 7, 23]. Kurzthaler *et al.* numerically computed the ISF for anisotropic ABPs and anisotropic Brownian circle swimmers from an infinite expansion of the Smoluchowski equation in spherical harmonic functions [6–8], and Schwarz-Linek *et al.* solved the Smoluchowski equation using a series of Mathieu functions to compute the ISF of *E. coli* [22]. Our results show good agreement with the aforementioned methods while offering a more readily interpretable form. Figure 2.2 presents the ISF as a function of time for various wavelengths at three different levels of activity. When activity is comparable to thermal energy the ISF decays monotonically for all wavenumbers, just as in a purely diffusive process (Fig. 2.2a). As activity increases the decay of the ISF becomes nonmonotonic and has dampened oscillations at sufficiently large wavenumbers (Fig. 2.2b, c). For large k the ISF decays monotonically and the onset of the decay begins sooner. When k is large, diffusion dominates over the ballistic behavior of the active motion. As activity increases, the active contribution begins to dominate over thermal diffusion at shorter times and larger wavenumbers, which extends the range of oscillations. These features agree with the results obtained by Kurzthaler *et al.* for anisotropic and circle swimmers.

The oscillations in the structure factor correspond to time-dependent density fluctuations, and are equivalent to those observed for the *sinc* function, which yields a dampened wave. As time increases towards the steady-state uniform distribution—approximately an order of magnitude beyond the reorientation timescale—the swimming motion becomes uncorrelated and each run length is a step in a random walk process, with a diffusivity governed by activity [24]. This transition corresponds to dampening of the oscillations observed in the decay of the ISF at small wavenumbers. Mathematically, this transition is the point where the arguments of the hyperbolic functions in Eq. (2.8) become imaginary. That is, Γ becomes imaginary when $k > (d-1)\sqrt{d}/2$ and results in a critical dimensionless wavenumber $k^{crit} \simeq 0.71$ for our two dimensional system. This transition from monotonic to oscillatory behavior as a function of wavenumber can be observed in Fig. 2.2b-c by the change in character from $kl = 0.5$(red) to $kl = 2.0$ (black). We additionally computed the transition point from correlated wavelike to diffusive motion as a function of moment closure, the details of which are given in Appendix 2.8.

A key benefit of the moment expansion method over a full numerical solution is the

availability of an analytic form for the ISF. Asymptotic analyses of this analytic form provide insight into the physical nature of the observed phenomena beyond locating the wave transition. For large displacements ($kl \to 0$) the density fluctuations decay as $\hat{n} \sim e^{-k^2 D^{eff} t}$ with an effective diffusivity, $D^{eff} = D_T + 2D^{swim}$, where D^{swim} is the diffusivity—as presented in Sec. 2.2—that results when the swimming motion becomes uncorrelated. For small displacements ($kl \to \infty$) the fluctuations are governed by dampened oscillations:

$$\hat{n} = e^{-\left(\frac{(d-1)}{2} + \frac{k^2}{d(d-1)} \frac{k_B T}{k_s T_s}\right) t} \left\{ \cos\left(\frac{kt}{\sqrt{d}}\right) + \frac{\sqrt{d}(d-1)}{2k} \sin\left(\frac{kt}{\sqrt{d}}\right) \right\}. \tag{2.9}$$

These oscillations in density capture the nondiffusive behavior witnessed by Takatori *et al.* [5].

In the short time limit $t \to 0$, the mean-squared displacement (MSD) is $\langle x^2 \rangle \sim 2dD_T t + U_0^2 t^2$, where the first term is the expected contribution from thermal motion and the second term arises from the ballistic swimming motion. This form of the MSD matches the results obtained by Ebbens *et al.* for their experimental catalytic swimmers [25]. The temporal scaling of each term explains the initial monotonicity in the decay of the ISF for times $t < \tau_R$ as $t > t^2$ and how this effect is reduced when activity is large. The ballistic scaling from activity is responsible for the "explosion" observed by Takatori *et al.* [5]. A full expression for the MSD is presented in Appendix 2.10.

The realspace density profile for active particles diffusing from an instantaneous source can also be calculated. For the following analysis we consider the case of diffusion from an infinite line source for mathematical simplicity. Since this is effectively a one-dimensional problem, the long wakes present in Fig. 2.1 are no longer observed. The number density as a function of distance from the line source is shown in Fig. 2.3 at several instances in time for different closures to the moment hierarchy with an activity of $k_s T_s = 100 k_B T$. While the first order closure to the moment hierarchy works very well for the ISF calculation, the large gradients in the initial density require a more sophisticated closure to obtain the realspace solution.

The transition from wavelike character is too slow with the simple $\mathbf{Q} = 0$ closure, and requires an additional mode of relaxation. We do this by adding the effects of nematic order, which have thus far been neglected. In the presence of large spatial gradients $\mathbf{Q}$ is nonzero and therefore contributes to the speed of the relaxation of

the wave. We rely on two different closures: assuming $\mathbf{Q}$ is slaved to the gradient of the polar order (solid lines) and assuming the third orientational moment $\mathbf{B} = \int(\mathbf{qqq} - \alpha \cdot \mathbf{q}/(d+2))P\, d\mathbf{q}$ is zero (dashed lines), where α is the appropriate fourth order isotropic tensor. The first alternative closure, $\mathbf{Q} \sim \mathbf{A} : \nabla\mathbf{m} \sim \nabla\mathbf{m}$, neglects $\mathbf{B}$ and higher order gradients of $\mathbf{Q}$, with constant tensor $\mathbf{A} = \boldsymbol{\alpha} - ((d+2)/d)\mathbf{II}$ (see Appendix 2.9 for the exact closure) whereas the second closure only neglects $\mathbf{B}$ while retaining the effects of thermal diffusion on the nematic order.

For each closure, the density was calculated using a finite element method (FEM) performed in FreeFem++ [26], and full Brownian dynamic (BD) simulations of ideal particles were performed to corroborate our results. The details of our simulations are outlined in Appendix 2.11. Slaving $\mathbf{Q}$ to $\nabla\mathbf{m}$ (solid lines) correctly captures the short time behavior of the system, but still fails to relax the wavefront quickly enough. Closing the expansion with $\mathbf{B} = 0$ (dashed lines) matches the BD simulations well for $t \geq \tau_R$, but fails to capture the strong wavelike character at short times. Correctly capturing the behavior of the density for all times requires a more sophisticated closure for the expansion.

Snapshots of a characteristic simulation of ABPs released from a point source with $k_s T_s = 100 k_B T$ are shown in Fig. 2.4. The dense wave (yellow) at short times expands outward and spreads until the system reaches a uniform denisty (purple) after several τ_R. This representation is evidence for the production of a relaxing wave that becomes diffusive, regardless of the dimensionality of the initial source.

Sokolov *et al.* observed similar wavelike behavior after cessation of rotation of a particle in a suspension of bacteria [27]. The rotating particle creates a stagnation zone wherein bacteria collect, which causes a large gradient in the radial density. After cessation of the particle, the bacteria explode outward in a wave, as indicated by Fig. $2f$ in [27] by the shifting peak in the density with time. We see in this instance, similar to the example of diffusion from an instantaneous source, that the wavelike behavior appears to result from large spatial disturbances in the density.

Thus far we have focused on suspensions of active Brownian particles released from instantaneous sources and have shown that the initial relaxation is ballistic and gets dampened out as the active motion becomes uncorrelated. As the motion decorrelates the relaxation resembles that of a diffusive process. In the following section we study the effects induced by the presence of an external orienting field and how this alters the relaxation behavior.

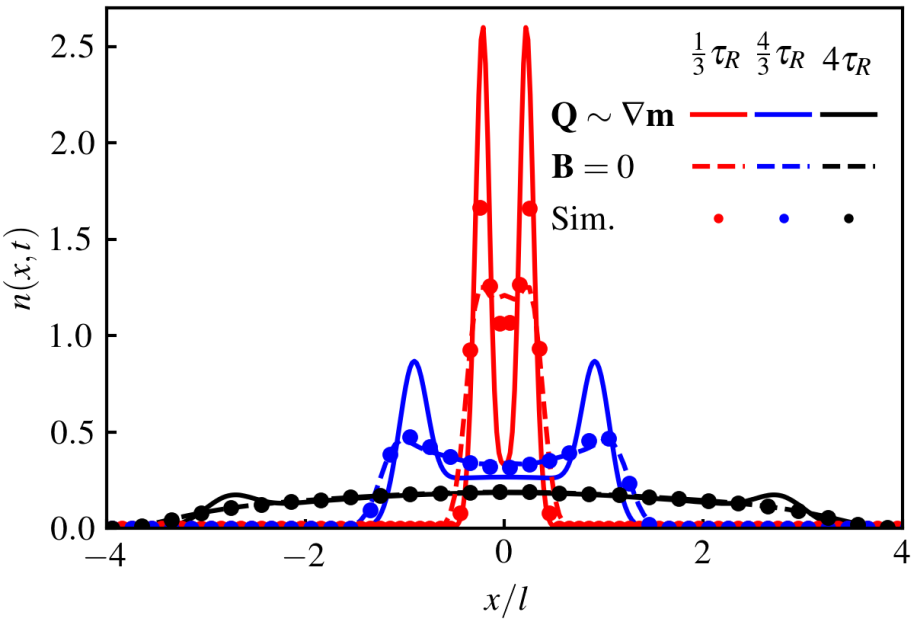

Figure 2.3: Number density of particles as a function of position from an infinite line source with $k_s T_s = 100 k_B T$. The solid lines, dashed lines, and symbols represent closures $\mathbf{Q} = \mathbf{A} : \nabla\mathbf{m}$, $\mathbf{B} = 0$, and BD simulations, respectively. The red, blue, and black colors correspond to $t = \tau_R/3$, $t = 4\tau_R/3$, and $t = 4\tau_R$, respectively.

2.5 Effects of an External Field

Consider the relaxation of active particles in the presence of an external orienting field. It is known that certain synthetic and living swimmers can be controlled through the application of external fields [28, 29], but these works have focused on the steady-state regime [28], the strength of long-time response based on reorientation statistics [30], or how a strong perturbation to the field direction affects a single swimmer [29]. To study the relaxation we modify the rotational flux of Eq. (2.1) to include the effects of an external orienting field. The rotational flux expression becomes

$$\mathbf{j}_R = D_R(\chi_R \mathbf{q} \times \hat{\mathbf{H}} P - \nabla_R P), \tag{2.10}$$

where $\hat{\mathbf{H}}$ is the unit vector in the field direction and $\chi_R \equiv \Omega_c \tau_R$ is the Langevin parameter with Ω_c being the magnitude of the angular velocity imposed by the field. Taking orientational moments results in the same expression for density conservation as before, but the expression for polar order becomes

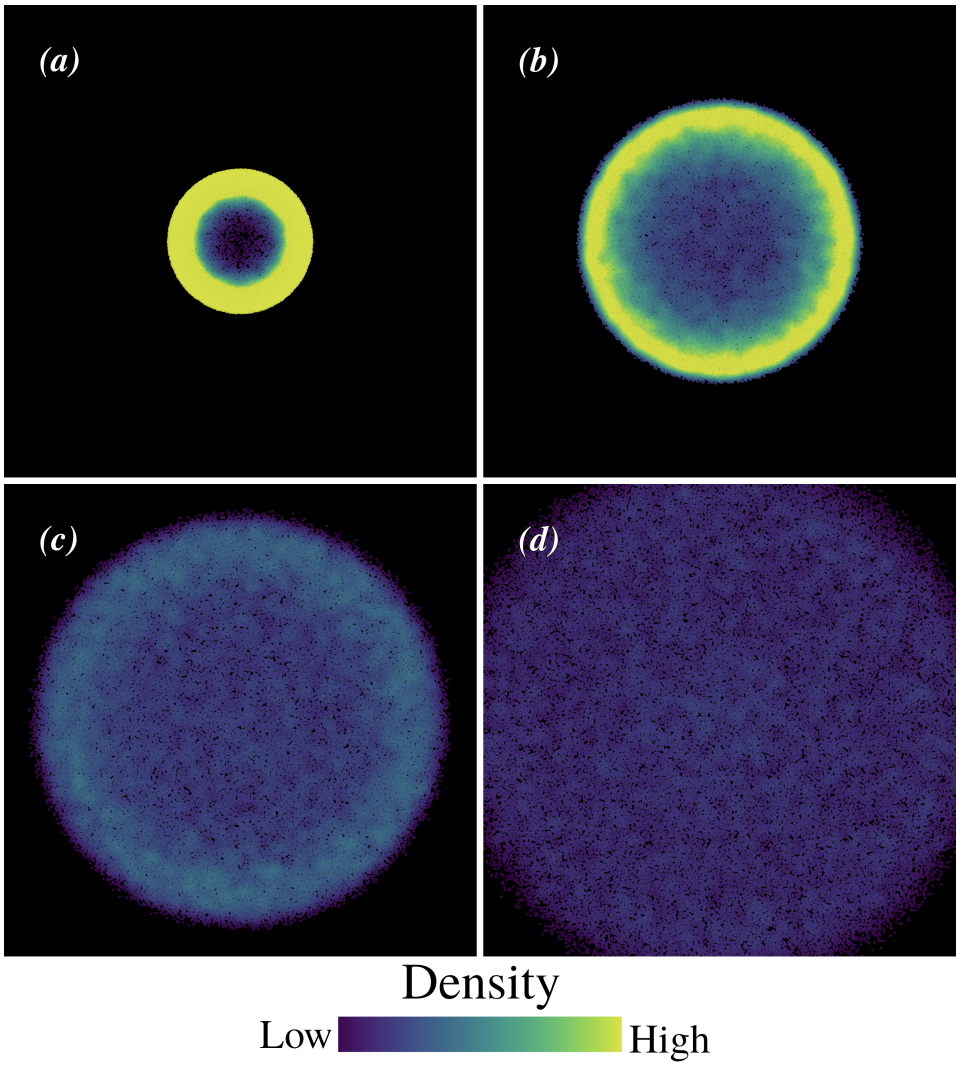

Figure 2.4: BD simulation snapshots for a system of ideal ABPs released from a two-dimensional point source with $k_s T_s = 100\ k_B T$ at (**a**) $t = \tau_R$, (**b**) $t = 2\tau_R$, (**c**) $t = 3\tau_R$, and (**d**) $t = 4\tau_R$. A dense wave of particles (yellow) can be seen spreading outward and diffusing until the system reaches a uniform density (purple).

$$\frac{\partial \mathbf{m}}{\partial t} + \nabla \cdot \mathbf{j}_m + \frac{(d-1)}{\tau_R}\mathbf{m} + \frac{\chi_R}{\tau_R}\mathbf{Q}\cdot\hat{\mathbf{H}} - \frac{(d-1)\chi_R}{d\tau_R} n\hat{\mathbf{H}} = 0,$$
$$\mathbf{j}_m = U_0\mathbf{Q} + \frac{1}{d}U_0 n\mathbf{I} - D_T\nabla\mathbf{m}. \tag{2.11}$$

We once again consider particles released from an infinite line source, with no initial polar order, but at time $t = 0$ we apply an external field in the positive x direction. The density of particles as a function of position at times less than, comparable to, and greater than τ_R are presented in Fig. 2.5 for various values of the Langevin parameter for a highly active system, $k_s T_s = 100 k_B T$. When χ_R is small (Fig. 2.5a) the density distribution looks similar to that presented in Fig. 2.3 when $t < \tau_R$, but with some asymmetry in the field direction. As time increases the peak moving opposite to the field relaxes faster while the peak moving in the field direction persists longer than it would in the absence of the field. As we increase the field strength to $\chi_R = 10$ (Fig. 2.5b) the particles initially moving opposite to the field direction are quickly reoriented resulting in a slight tailing of the density distribution, and when $t > \tau_R$ the particles have reoriented thus reducing the tailing. Importantly, the spread in the density peak then is primarily from translational diffusion. When $\chi_R = 100$ (Fig. 2.5c) the alignment effect is further enhanced and all particles are aligned in the field direction almost immediately after the field is turned on. This strong alignment prevents fluctuations in orientation from activity resulting in a more persistent wavefront. The spread of the distribution is almost exclusively from thermal noise as evidenced by the mean and peak density speeds being equal to the swim speed. A strong orienting field reduces the swim diffusivity in the field direction as $\langle D_{\parallel}^{swim}\rangle \sim O(\chi_R^{-3})$ and as $\langle D_{\perp}^{swim}\rangle \sim O(\chi_R^{-2})$ in the transverse direction, as shown by Takatori and Brady [28].

The persistence of the wave in the field direction and the dissipation of the wave in the opposite direction are better understood by calculating the mean-squared orientational displacement. The evolution for the average orientation is

$$\frac{\partial}{\partial t}\langle \mathbf{q}\rangle = -\frac{(d-1)}{\tau_R}\langle \mathbf{q}\rangle - \frac{\chi_R}{\tau_R}\langle(\mathbf{q}\mathbf{q}\cdot\hat{\mathbf{H}} - \hat{\mathbf{H}})\rangle, \tag{2.12}$$

where angled brackets represent an ensemble average. In the linear response regime (where χ_R is small) the rightmost term can be represented by $\langle(\mathbf{q}\mathbf{q}\cdot\hat{\mathbf{H}} - \hat{\mathbf{H}})\rangle_0 = \int[(\mathbf{q}\mathbf{q}\cdot\hat{\mathbf{H}} - \hat{\mathbf{H}})]\, d\mathbf{q} = -(d-1)\hat{\mathbf{H}}/d$. From this,

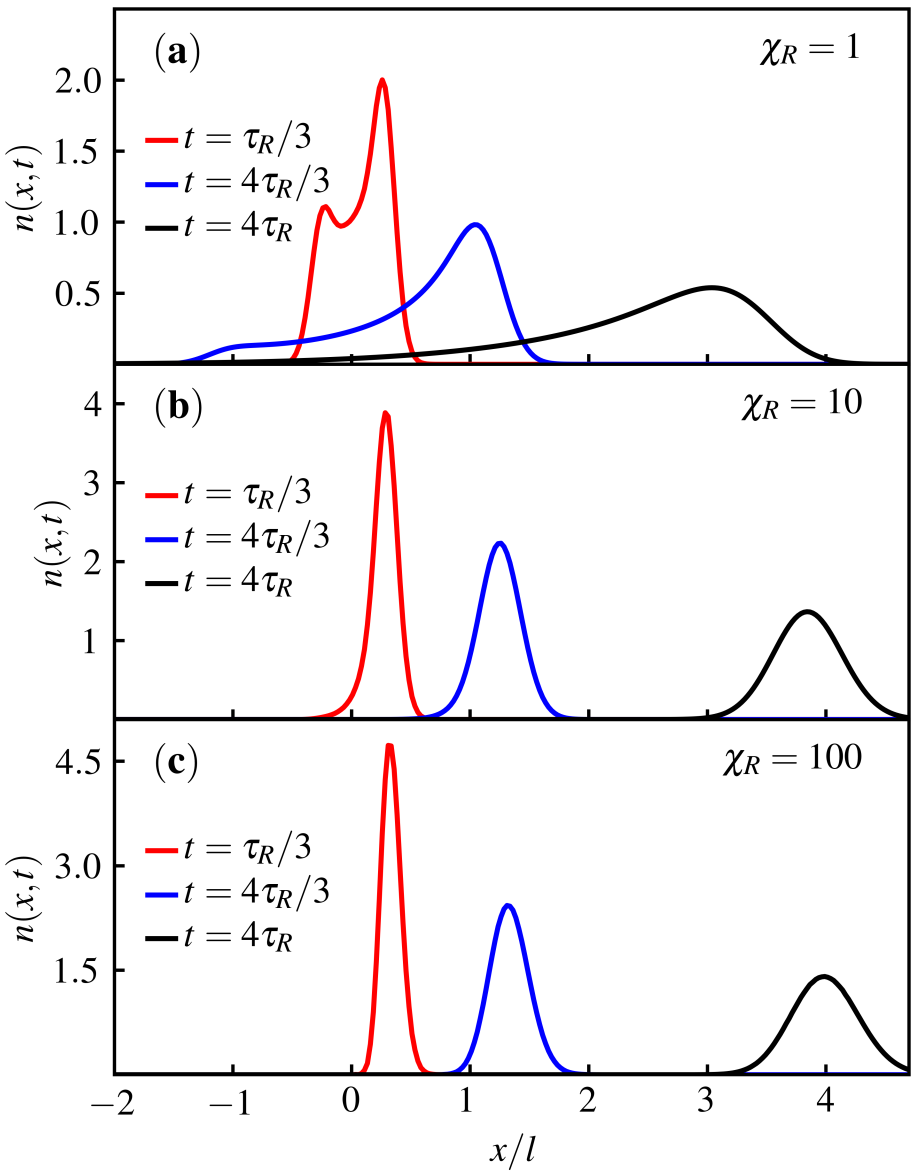

Figure 2.5: The mean squared displacement as a function of time normalized by the reorientation time at **(a)** $\chi_R = 1$, **(b)** $\chi_R = 10$, and **(c)** $\chi_R = 100$.

$$\langle \mathbf{q}(t) \rangle = \frac{\chi_R}{d} \hat{\mathbf{H}} [1 - e^{-(d-1)t/\tau_R}] + \mathbf{q_0} e^{-(d-1)t/\tau_R}, \tag{2.13}$$

where $\mathbf{q_0} = \langle \mathbf{q}(0) \rangle$. Multiplying Eq. (2.13) by $\mathbf{q_0}$ and using $\langle (\mathbf{q}(t) - \mathbf{q}(0))^2 \rangle = \langle \mathbf{q}^2(t) + \mathbf{q}^2(0) - 2\mathbf{q}(t) \cdot \mathbf{q}(0) \rangle$ in the limit of $t/\tau_R << 1$ gives a mean squared orientational displacement of

$$\langle(\mathbf{q}(t)-\mathbf{q}(0))^2\rangle \simeq 2(d-1)\left[1-\frac{\chi_R}{d}\langle\hat{\mathbf{H}}\cdot\mathbf{q}(0)\rangle\right]\frac{t}{\tau_R}. \tag{2.14}$$

From Eqs. 2.13 and 2.14 we see mean squared orientational displacement is greatly reduced in the field direction and enhanced in the opposite direction, resulting in the persistence and expedited dissipation of the two wavefronts, respectively. We can validate this result by computing the change to the average swim diffusivity $\langle D^{swim}\rangle \sim L_{eff}^2/\tau_R$, where $L_{eff} \sim (U_0 - \langle u\rangle)\tau_R$ is the effective step size of a particle. The average velocity is given by $\langle\mathbf{u}\rangle = U_0\langle\mathbf{q}\rangle$, which is 0 in the absence of an external field and is $\chi_R\hat{\mathbf{H}}/d$ with an external field in the linear response regime, as shown by taking the long-time limit of Eq. (2.13). This gives the change in effective step size as $\Delta L_{eff} \sim \chi_R U_0\tau_R$ and a scaling for the change in swim diffusivity as $\langle\Delta\mathbf{D}^{swim}\rangle \sim (U_0^2\tau_R)\chi_R^2$, which is in agreement with the predictions by Takatori and Brady [28]. Note that in the presence of an external orienting field the swim diffusivity is $\langle\mathbf{D}^{swim}\rangle \sim U_0^2\tau_R(1+O(\chi_R^2))$ and is anisotropic.

2.6 Conclusions

We have provided a model for active dynamics that provides insight into the wavelike behavior observed in active systems and have provided an explanation for how these dynamics relax. This motion and its transition to the steady-state diffusive behavior was shown through the relaxation of a dilute active system from an instantaneous source. The results were corroborated through BD simulations and comparison of the ISF with existing works [6, 7, 9, 23]. At short times a strong wavelike character is present, and as the swimming motion becomes uncorrelated the overall motion becomes diffusive with an effective diffusivity given by the sum of the translational, D_T, and swim, D^{swim} diffusivities and is described via the telegraph equation. The wavelike behavior observed for small displacements is supported by oscillations in density fluctuations in the system as predicted by the intermediate scattering function. We have calculated and correctly captured this behavior using a simple expansion of orientational moments with different closures: $\mathbf{Q} = 0$, $\mathbf{Q} \sim \nabla\mathbf{m}$, and $\mathbf{B} = 0$. While the majority of the relaxation results focus on diffusion from a line source, the methods shown readily extend to higher spatial dimensions.

The strength of an active wave can be maintained as shown by extension of the instantaneous source diffusion problem through the addition of an external orienting field. As the field strength increases, active constituents become unable to reorient, which is the primary mode of wave relaxation, thus increasing the life of the wave and

allowing for greater displacements through more directed motion. The mean squared orientational displacement of active particles in the presence of an orientating field compared to the unbiased case of free swimmers supports the claim in Takatori and Brady [28] that the persistence of the ballistic motion is primarily dependent on how correlated particle orientations are in time.

Given the observations presented we propose that the only criterion necessary for wavelike behavior is the existence of a mechanism through which the particle orientations can be recorrelated. This allows us to predict further instances wherein waves could be observed in active systems. For example, active suspensions near criticality should exhibit wavelike behavior as noncritical nuclei form and melt. The formation of noncritical nuclei results in large fluctuations in the density and their melting is analogous to the explosion of a 'swimmer-crystal' observed by Takatori *et al.* [5] which, as previously discussed, clearly showcases a wave after release of the trap. Through our work we believe that waves are an inherent part of many active systems as they transition from a ballistic to diffusive motion.

Appendix

2.7 Orientational Moments

Starting with Eq. (2.1) from section 2.2 and integrating over orientation gives

$$\frac{\partial n}{\partial t} + \nabla \cdot \mathbf{j}_n - D_R \int (\mathbf{q} \times \nabla_q) \cdot (\mathbf{q} \times \nabla_q) P \, d\mathbf{q}, \tag{2.15}$$

where $(\mathbf{q} \times \nabla_q) \cdot (\mathbf{q} \times \nabla_q) = \nabla_q \cdot \nabla_q$ [31] and $\mathbf{j}_n = U_0 \int \mathbf{q} P \, d\mathbf{q} - D_T \nabla \int P \, d\mathbf{q}$. From periodicity we have $\int \nabla_q^2 P \, d\mathbf{q} = 0$, which yields the resulting conservation equation for the number density (Eq. (2.2)).

When computing the first moment, we need to first multiply the Smoluchowski equation by $\mathbf{q}$ then integrate as was done for the zeroth moment. Doing so and using our definitions for the polar and nematic orders gives

$$\begin{aligned} &\frac{\partial \mathbf{m}}{\partial t} + \nabla \cdot \mathbf{j}_m - D_R \int \mathbf{q} \nabla_q^2 P \, d\mathbf{q} = 0, \\ &\mathbf{j}_m = U_0 \int \mathbf{q}\mathbf{q} P \, d\mathbf{q} - D_T \nabla \mathbf{m}, \end{aligned} \tag{2.16}$$

where the third term has been simplified using equation A.44 from reference [31]—as was done for the zeroth moment derivation. From here, it is helpful to write the

integrand in Einstein notation as

$$\int q_i \frac{\partial}{\partial q_j} \frac{\partial}{\partial q_j} [P] \, d\mathbf{q}. \tag{2.17}$$

Making use of the product rule and Eqs. A.25 and A.41 from reference [31], we can simplify the expression as follows:

$$\begin{aligned}
\int q_j \frac{\partial}{\partial q_i} [f_i] \, d\mathbf{q} =& \int \frac{\partial}{\partial q_i} [q_j f_i] \, d\mathbf{q} - \int (\delta_{ij} - q_i q_j) f_i \, d\mathbf{q} \\
=&(d-1) \int q_j f_i q_i \, d\mathbf{q} - \delta_{ij} \int f_i \, d\mathbf{q} + \int q_j f_i q_i \, d\mathbf{q} \\
=&d \int q_j f_i q_i \, d\mathbf{q} - \int f_j \, d\mathbf{q} \\
=&d \int q_i q_j \frac{\partial P}{\partial q_i} \, d\mathbf{q} - \int \frac{\partial P}{\partial q_j} \, d\mathbf{q} \\
=&d \Bigg[\int \frac{\partial}{\partial q_i} (q_i q_j P) \, d\mathbf{q} - \int ((\delta_{ij} - q_i q_j) q_i P \, d\mathbf{q} \\
&- \int (\delta_{ii} - q_i q_i) q_j P \, d\mathbf{q} \Bigg] - \int \frac{\partial P}{\partial q_j} \, d\mathbf{q} \\
=&d \Bigg[(d-1) \int q_i q_i q_j P \, d\mathbf{q} - \int q_j P \, d\mathbf{q} + \int q_j P \, d\mathbf{q} \\
&- (d-1) \int q_j P \, d\mathbf{q} \Bigg] - (d-1) \int q_j P \, d\mathbf{q} \\
=& -(d-1) \int q_j P \, d\mathbf{q} \\
=& -(d-1)\mathbf{m},
\end{aligned} \tag{2.18}$$

where $f_i = \partial P / \partial q_i$ and d is the number of rotational dimensions. Substituting this back into Eq. (2.16) and adding and subtracting $\mathbf{I}n/d$ to the flux results in the polar order conservation equation from Eq. (2.3).

This process can be repeated for subsequent moments. For reference, the conservation equations for the second and third moments are given below:

$$\begin{aligned}
&\frac{\partial \mathbf{Q}}{\partial t} + \nabla \cdot \mathbf{j}_Q + (2d) D_R \mathbf{Q} = 0, \\
&\mathbf{j}_Q = U_0 \mathbf{B} + \frac{U_0}{(d+2)} \left(\boldsymbol{\alpha} - \frac{d+2}{d} \mathbf{II} \right) \cdot \mathbf{m} - D \nabla \mathbf{Q},
\end{aligned} \tag{2.19}$$

$$\begin{aligned}
&\frac{\partial \mathbf{B}}{\partial t} + \nabla \cdot \mathbf{j}_B + 3(d+1) D_R \mathbf{B} = 0, \\
&\mathbf{j}_B = U_0 \mathbf{C} + U_0 \left(\frac{1}{2(d+4)} \boldsymbol{\beta} : \mathbf{Q} - \frac{1}{(d+2)} \boldsymbol{\alpha} \cdot \mathbf{Q} \right) - D_T \nabla \mathbf{B},
\end{aligned} \tag{2.20}$$

where $\mathbf{C} = \int \left(\mathbf{qqqq} - \frac{1}{d(d+2)} \boldsymbol{\alpha} - \frac{1}{2(d+4)} \boldsymbol{\beta} : \left[\mathbf{qq} - \frac{1}{d} \mathbf{I} \right] \right) P \, d\mathbf{q}$ is the fourth orientational moment and β is the appropriate sixth-order isotropic tensor given by

$$\begin{aligned}
\beta_{ijklmn} = {} & \delta_{ij}\delta_{kl}\delta_{mn} + \delta_{ij}\delta_{km}\delta_{ln} + \delta_{ij}\delta_{kn}\delta_{lm} + \delta_{ik}\delta_{jl}\delta_{mn} + \delta_{ik}\delta_{jm}\delta_{ln} \\
& + \delta_{ik}\delta_{jn}\delta_{lm} + \delta_{il}\delta_{jk}\delta_{mn} + \delta_{il}\delta_{jm}\delta_{kn} + \delta_{il}\delta_{jn}\delta_{km} + \delta_{im}\delta_{jk}\delta_{ln} \\
& + \delta_{im}\delta_{jl}\delta_{kn} + \delta_{im}\delta_{jn}\delta_{kl} + \delta_{in}\delta_{jk}\delta_{lm} + \delta_{in}\delta_{jl}\delta_{km} + \delta_{in}\delta_{jm}\delta_{kl}.
\end{aligned} \tag{2.21}$$

2.8 Wave Transition

Fourier transforming the conservation equations for the orientational moments of the probability distribution function $P(\mathbf{x}, \mathbf{q}, t)$ in space and subsequently Laplace transforming in time generates a system of algebraic equations. The system of equations can be rewritten as an explicit expression for $\hat{n}(\mathbf{k}, s)$ with the following structure:

$$\hat{n}(\mathbf{k}, s) = \cfrac{1}{b_0 + \cfrac{a_1}{b_1 + \cfrac{a_2}{b_2 + \cdots}}}, \tag{2.22}$$

which can be represented in continued fraction form as

$$\hat{n}(\mathbf{k}, s) = \left[b_0 + \mathrm{K}_{j=1}^{\infty} \frac{a_j}{b_j} \right]^{-1}, \tag{2.23}$$

where s is the frequency. The terms a_j and b_j are given by the series:

$$
\begin{aligned}
a_j &= \frac{(-1)^{j+1} j(d-3+j) U_0^2 k^2}{(d-4+2j)(d-2+2j)}, \\
b_j &= \left(s + k^2 D_T + j(d-2+j) D_R\right),
\end{aligned}
\tag{2.24}
$$

where a_j comes from the isotropic definition of the $(j+1)$ moment in the j^{th} moment equation and b_j comes from the sink term on the j^{th} moment equation.

This expression for $\hat{n}(\mathbf{k}, s)$ is used to calculate the transition from wavelike to diffusive behavior. We demonstrate this by calculating the transition obtained from choosing the simplest moment closure of $\mathbf{Q} = 0$. From the first two moments we obtain

$$
\hat{n}(\mathbf{k}, s) = \frac{1}{s + D_T k^2 + \dfrac{\frac{1}{d} U_0^2 k^2}{s + D_T k^2 + (d-1) D_R}}
\tag{2.25}
$$

for the transformed density. We then take the non-diffusive limit ($\lim D_T \to 0$), and nondimensionalize the wavenumber and frequency by $\bar{\mathbf{k}} = \mathbf{k} l$ and $\bar{s} = s\tau_R$, respectively. The number density expression then becomes

$$
\hat{n} = \frac{\tau_R(\bar{s} + (d-1))}{\bar{s}^2 + (d-1)\bar{s} + \frac{1}{d}\bar{k}^2},
\tag{2.26}
$$

with poles given by

$$
\bar{s}^2 + (d-1)\bar{s} + \frac{1}{d}\bar{k}^2 = 0.
\tag{2.27}
$$

The transition from wavelike to diffusive behavior occurs when the poles become imaginary, whence,

$$
\bar{s} = -\frac{(d-1)}{2} \pm \frac{1}{2}\sqrt{(d-1)^2 - \frac{4}{d}\bar{k}^2},
\tag{2.28}
$$

and become imaginary when $\bar{k}^2 > d(d-1)^2/4$, which matches the result we get from our analytic expression for the Fourier transformed number density.

2.9 Alternative Closure for Q

The conservation equation for the nematic order with a closure of $\mathbf{B} = 0$ and neglecting high order spatial derivatives of $\mathbf{Q}$ gives

$$\begin{aligned}\frac{\partial \mathbf{Q}}{\partial t} + \nabla \cdot \left(\frac{U_0}{(d+2)} \left(\boldsymbol{\alpha} - \frac{(d+2)}{d}\mathbf{II}\right) \cdot \mathbf{m} \right) \\ + \frac{2d}{\tau_R}\mathbf{Q} = 0,\end{aligned} \tag{2.29}$$

which can be rewritten as

$$\mathbf{Q} = -\frac{U_0}{2d(d+2)D_R}\left(1 - e^{-2dD_R t}\right)\nabla\Big(\mathbf{A} : \mathbf{m}\Big), \tag{2.30}$$

where $\mathbf{A} = \boldsymbol{\alpha} - ((d+2)/d)\mathbf{II}$ and α is the appropriate isotropic fourth order tensor, as defined in the main text.

2.10 Mean-Squared Displacement

The mean-squared displacement (MSD) is given by

$$\langle x^2 \rangle = -\nabla_k \nabla_k \hat{n}(\mathbf{k}, t)|_{k=0}, \tag{2.31}$$

for any instant in time. The full MSD expression with $\mathbf{Q} = 0$ closure is

$$\begin{aligned}\langle x^2 \rangle = \frac{4\alpha}{d(d-1)^2} e^{-\alpha} \Big[\left(1 + \frac{k_B T}{k_s T_s}\right) \cosh \alpha \\ + \left(1 - \frac{1}{\alpha} + \frac{k_B T}{k_s T_s}\right) \sinh \alpha \Big],\end{aligned} \tag{2.32}$$

where $\alpha = \frac{(d-1)}{2} t$ and t is normalized by the reorientation time τ_R. A plot of the MSD is presented in Fig. 2.6 for various levels of activity. For $t << \tau_R$ the MSD scales linearly with time because thermal diffusion wins out over active motion. As time increases the MSD goes quadratically with time due to the persistent and directed active swimming. For $t > \tau_R$ the swimming motion becomes uncorrelated and the active particles become diffusive with an effective diffusivity which is a combination of the thermal diffusivity and swim diffusivity D^{swim}.

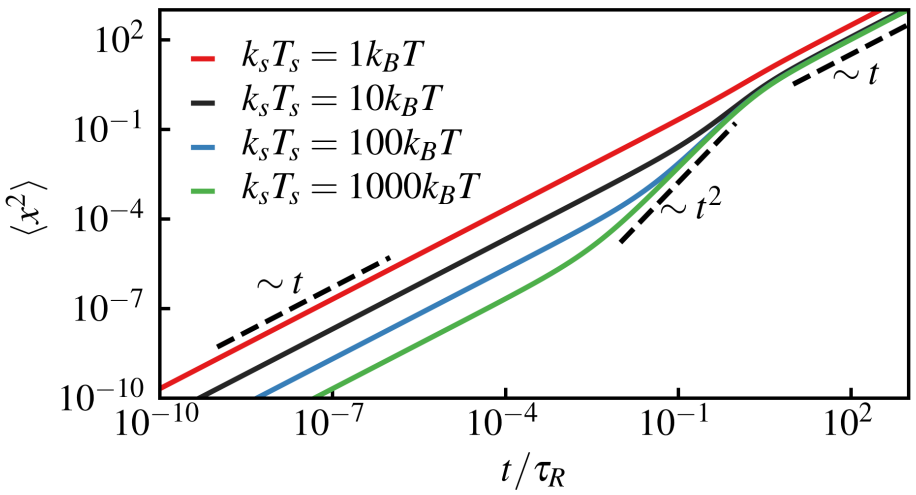

Figure 2.6: The mean squared displacement as a function of time normalized by the reorientation time at different levels of activity.

2.11 Brownian Dynamic Simulations

We simulate suspensions of ideal ABPs using the overdamped Langevin equations for translation and orientation:

$$0 = -\zeta \mathbf{U} + \zeta \mathbf{U}_0 + \mathbf{F}^B, \tag{2.33}$$

$$0 = -\zeta_R \mathbf{\Omega} + \mathbf{L}^R. \tag{2.34}$$

Here ζ is the hydrodynamic resistance coupling translational velocity to force, $\mathbf{U}$ is the translational velocity, $\zeta \mathbf{U}_0$ is the active—or swim—force [24], $\mathbf{F}^B$ is the random Brownian force, ζ_R is the hydrodynamic resistance coupling angular velocity to torque, $\mathbf{\Omega}$ is the angular velocity, and $\mathbf{L}^R$ is the reorientation torque. The Brownian force is modeled using the usual white-noise statistics with $\overline{\mathbf{F}^B} = 0$ and $\overline{\mathbf{F}^B(0)\mathbf{F}}^B(t) = 2k_B T \zeta \delta(t)\mathbf{I}$. The reorientation torque is modeled in similar fashion with $\overline{\mathbf{L}^R} = 0$ and $\overline{\mathbf{L}^R(0)\mathbf{L}}^R(t) = 2\zeta_R^2 \delta(t)\mathbf{I}/\tau_R$.

References

[1] C. Bechinger, R. Di Leonardo, H. Löwen, C. Reichhardt, G. Volpe, and G. Volpe, "Active Particles in Complex and Crowded Environments", Reviews of Modern Physics **88**, 045006 (2016).

[2] S. A. Mallory, C. Valeriani, and A. Cacciuto, "An Active Approach to Colloidal Self-Assembly", Annual Review of Physical Chemistry **69**, 59–79 (2018).

[3] F. J. Sevilla and L. A. Gómez Nava, "Theory of diffusion of active particles that move at constant speed in two dimensions", Physical Review E **90**, 022130 (2014).

[4] F. J. Sevilla and M. Sandoval, "Smoluchowski diffusion equation for active Brownian swimmers", en, Physical Review E **91**, 052150 (2015).

[5] S. C. Takatori, R. De Dier, J. Vermant, and J. F. Brady, "Acoustic trapping of active matter", en, Nature Communications **7**, 10694 (2016).

[6] C. Kurzthaler, S. Leitmann, and T. Franosch, "Intermediate scattering function of an anisotropic active Brownian particle", en, Scientific Reports **6**, 36702 (2016).

[7] C. Kurzthaler and T. Franosch, "Intermediate scattering function of an anisotropic Brownian circle swimmer", en, Soft Matter **13**, 6396–6406 (2017).

[8] C. Kurzthaler, C. Devailly, J. Arlt, T. Franosch, W. C. K. Poon, V. A. Martinez, and A. T. Brown, "Probing the Spatiotemporal Dynamics of Catalytic Janus Particles with Single-Particle Tracking and Differential Dynamic Microscopy", en, Physical Review Letters **121**, 078001 (2018).

[9] F. J. Sevilla and P. Castro-Villarreal, "Generalized persistence dynamics for active motion", arXiv (2019).

[10] S. C. Takatori and J. F. Brady, "Forces, stresses and the (thermo?) dynamics of active matter", Current Opinion in Colloid & Interface Science **21**, 24–33 (2016).

[11] M. E. Cates and J. Tailleur, "When are active Brownian particles and run-and-tumble particles equivalent? Consequences for motility-induced phase separation", EPL (Europhysics Letters) **101**, 20010 (2013).

[12] F. J. Sevilla, "Two-dimensional active motion", Physical Review E **101**, 022608 (2020).

[13] D. Saintillan and M. J. Shelley, *Complex Fluids in Biological Systems*, edited by S. E. Spagnolie, Biological and Medical Physics, Biomedical Engineering (Springer New York, New York, NY, Nov. 2015) Chap. 9, p. 449.

[14] W. Yan and J. F. Brady, "The force on a boundary in active matter", en, Journal of Fluid Mechanics **785**, R1 (2015).

[15] W. Alharbi and S. Petrovskii, "Critical Domain Problem for the Reaction–Telegraph Equation Model of Population Dynamics", Mathematics **6**, 59 (2018).

[16] H. Du, Z. Xu, M. Anyan, O. Kim, W. M. Leevy, J. D. Shrout, and M. Alber, "High Density Waves of the Bacterium Pseudomonas aeruginosa in Propagating Swarms Result in Efficient Colonization of Surfaces", Biophysical Journal **103**, 601–609 (2012).

[17] P. M. Morse and H. Feshbach, *Methods of theoretical physics* (McGraw-Hill, 1953).

[18] S. C. Takatori and J. F. Brady, "Towards a thermodynamics of active matter", en, Physical Review E **91**, 032117 (2015).

[19] L. Van Hove, "Correlations in Space and Time and Born Approximation Scattering in Systems of Interacting Particles", en, Physical Review **95**, 249–262 (1954).

[20] L. G. Wilson, V. A. Martinez, J. Schwarz-Linek, J. Tailleur, G. Bryant, P. N. Pusey, and W. C. K. Poon, "Differential Dynamic Microscopy of Bacterial Motility", en, Physical Review Letters **106**, 018101 (2011).

[21] V. A. Martinez, R. Besseling, O. A. Croze, J. Tailleur, M. Reufer, J. Schwarz-Linek, L. G. Wilson, M. A. Bees, and W. C. Poon, "Differential Dynamic Microscopy: A High-Throughput Method for Characterizing the Motility of Microorganisms", en, Biophysical Journal **103**, 1637–1647 (2012).

[22] J. Schwarz-Linek, J. Arlt, A. Jepson, A. Dawson, T. Vissers, D. Miroli, T. Pilizota, V. A. Martinez, and W. C. Poon, "Escherichia coli as a model active colloid: A practical introduction", en, Colloids and Surfaces B: Biointerfaces **137**, 2–16 (2016).

[23] C. Kurzthaler, C. Devailly, J. Arlt, T. Franosch, W. C. K. Poon, V. A. Martinez, and A. T. Brown, "Probing the Spatiotemporal Dynamics of Catalytic Janus Particles with Single-Particle Tracking and Differential Dynamic Microscopy", en, Physical Review Letters **121**, 078001 (2018).

[24] S. C. Takatori, W. Yan, and J. F. Brady, "Swim Pressure: Stress Generation in Active Matter", en, Physical Review Letters **113**, 028103 (2014).

[25] S. Ebbens, R. A. L. Jones, A. J. Ryan, R. Golestanian, and J. R. Howse, "Self-assembled autonomous runners and tumblers", en, Physical Review E **82**, 015304 (2010).

[26] F. Hecht, "New development in FreeFem++", J. Numer. Math. **20**, 251–265 (2012).

[27] A. Sokolov, L. D. Rubio, J. F. Brady, and I. S. Aranson, "Instability of expanding bacterial droplets", en, Nature Communications **9**, 1322 (2018).

[28] S. C. Takatori and J. F. Brady, "Swim stress, motion, and deformation of active matter: effect of an external field", en, Soft Matter **10**, 9433–9445 (2014).

[29] W. Gao, X. Feng, A. Pei, Y. Gu, J. Li, and J. Wang, "Seawater-driven magnesium based Janus micromotors for environmental remediation", Nanoscale **5**, 4696 (2013).

[30] B. Hancock and A. Baskaran, "Effect of reorientation statistics on torque response of self-propelled particles", Physical Review E **92**, 052143 (2015).

[31] D. W. Condiff and H. Brenner, "Transport Mechanics in Systems of Orientable Particles", Physics of Fluids **12**, 539 (1969).

Chapter 3

ACTIVE COMPRESSIBILITY

We demonstrate that the mechanically-defined "isothermal" compressibility behaves as a thermodynamic-like response function for suspensions of purely-repulsive active Brownian particles. The compressibility computed from the active pressure—a combination of the collision and unique swim pressures—is capable of predicting the critical point for motility induced phase separation, as expected from the mechanical stability criterion. We relate this mechanical definition to the static structure factor via an active form of the thermodynamic compressibility equation, and find the two to be equivalent, as would be the case for equilibrium systems. This equivalence indicates that compressibility behaves like a thermodynamic response function, even when activity is large. Finally, we discuss the importance of the phase interface when defining an active chemical potential. Previous definitions of the active chemical potential are shown to be accurate above the critical point but breakdown in the coexistence region. Inclusion of the swim pressure in the mechanical compressibility definition suggests that the interface is essential for determining phase behavior.

This chapter includes content from our previously published article:

[1] A. R. Dulaney, S. A. Mallory, and J. F. Brady, "The "isothermal" compressibility of active matter",
A.R.D. participated in the conception of the project, performed the calculations, analyzed the data, and participated in the writing of the manuscript. (2020),

3.1 Introduction

Response functions are central to thermodynamics and the study of critical phenomena. These quantities, which are those most frequently probed in experiment (or simulation), include various heat capacities, compressibilities, and magnetic susceptibilities. Each response function serves as a metric on how a specific state variable changes as other independent state variables are varied under controlled conditions. For example, isothermal compressibility, one of the more prominent response functions and the focus of this study, is a measure of the relative volume change of a system in response to a change in pressure at constant temperature. Isothermal compressibility has played a central role in unraveling the confounding properties of water and more generally served as a means for identifying novel phase transitions in complex fluids [1–3]. For an isotropic, homogeneous fluid at equilibrium the isothermal compressibility takes a simple form

$$\chi_T = -\frac{1}{V}\left(\frac{\partial V}{\partial \Pi}\right)_{N,T} = \frac{1}{n}\left(\frac{\partial n}{\partial \Pi}\right)_{N,T}, \tag{3.1}$$

where V is the volume of the system, Π is pressure, and n is the number density defined by $n = N/V$ with N being the number of particles in the system.

From a statistical mechanical perspective, response functions offer a systematic way of characterizing the magnitude of fluctuations and correlation lengths in a system. In this context, the isothermal compressibility is a measure of local density fluctuations. It is straight-forward to show for an isotropic, homogeneous, thermodynamic system that the isothermal compressibility is given by

$$n k_B T \chi_T = \frac{\langle (\Delta N)^2 \rangle}{\langle N \rangle} = \frac{(\langle N^2 \rangle - \langle N \rangle^2)}{\langle N \rangle}, \tag{3.2}$$

where $k_B T$ is the thermal energy scale and $\langle (\Delta N)^2 \rangle$ is the variance in number density [4]. As this result can only be derived in the grand canonical ensemble, N here is interpreted as the number of particles in a subsystem of macroscopic dimension V, which is in equilibrium with a much larger thermodynamic system.

Equivalently, one can compute isothermal compressibility directly from the system microstructure—as is often done in the study of liquids—via the compressibility equation

$$n k_B T \chi_T = \lim_{\boldsymbol{k} \to 0} S(\boldsymbol{k}) = \left(1 + n \int [g(r) - 1] d\boldsymbol{r}\right), \tag{3.3}$$

where $g(r)$ is the radial-distribution function and S($\mathbf{k}$) is the static structure factor. Finally, one can also compute the compressibility by means of the free energy, or more precisely, from the chemical potential μ:

$$\chi_T = \frac{1}{n^2}\left(\frac{\partial n}{\partial \mu}\right)_{V,T}, \tag{3.4}$$

where the partial derivative is taken at constant volume and temperature. For thermodynamic consistency to hold in equilibrium systems, we have equivalency of these three methods: mechanical, thermodynamic, and structural (see Fig. 3.1).

In this study, we explore whether the same equivalence and consistency exist for an important class of nonequilibrium systems—active Brownian particles (ABPs). The motivation for carrying out this work is multifold. ABPs have become a popular minimal model for understanding the behavior of active or self-propelled colloids, bacteria, and other living systems. The defining characteristic of an active colloid, which makes it unique relative to its purely passive Brownian counterpart, is the driven and persistent nature of its motion. This difference in dynamics is responsible for a wealth of interesting and novel behaviors including spontaneous clustering [5], swarming, and motility-induced phase separation [6–10]. For this reason, suspensions of active colloids have garnered interest from the material science and engineering community as they represent a potentially innovative approach to directed transport, self-assembly, and material design at the microscale [9, 11].

The collective behavior of these active matter systems is incredibly rich and has aided the development of new nonequilibrium theories [12–15]. Motility-induced phase separation (MIPS) has been a particular focal point for many in the active matter community. Surprisingly, a suspension of active colloids interacting solely through their excluded volume undergoes a nonequilibrium phase transition into a dilute and dense phase–akin to liquid-vapor coexistence in a typical equilibrium liquid [7, 8, 16]. A great deal of effort has gone towards developing theories capable of deducing the coexistence criterion for MIPS. Significantly less attention has been paid to the behavior of active colloids above the critical point, where there remain a number of open and important questions about this supercritical region [17–19].

Due to advances in experimental methods, there has been a resurgence of interest in properties of equilibrium systems in the supercritical phase. The highly tunable behavior of molecular supercritical fluids has lead to a number of industrial applications and the introduction of new theoretical concepts in liquid state theory such

as the Fisher–Widom line, the Widom line, and the Frenkel line [2, 20, 21]. These lines, which are identified using various thermodynamic response function (for instance, the Widom line is often identified by a peak in the isobaric heat capacity), delineate characteristic regions within the supercritical region of the phase diagram. It remains to be seen whether these ideas can be extended to suspensions of active colloids. Given the similarity of the MIPS transition with liquid-gas condensation, there is some optimism that supercritical active fluids can play as versatile a role as their molecular counterparts.

A first step toward this aim is to consolidate the notion of isothermal compressibility for active suspensions. Like many other microscopic systems, the structure factor has become an important diagnostic for active systems. In one of the earliest papers regarding MIPS, Fily et al. made use of the static structure factor to characterize the phase behavior of ABPs about the MIPS critical point [8]. A recent study by Chakraborti et al. introduced a notion of compressibility for active systems [22]. By making use of a large deviation framework and assuming the property of additivity, they define a nonequilibrium chemical potential μ as the change in a nonequilibrium free energy required to insert a particle into the system—as is done in equilibrium thermodynamics. Using this chemical potential and the partition function for a given subvolume of the system, they derived the following expression for the compressibility:

$$\frac{\partial n}{\partial \mu} = \lim_{V\to\infty} \frac{1}{V}(\langle \Delta N\rangle^2) = \lim_{V\to\infty} \frac{1}{V}(\langle N^2\rangle - \langle N\rangle^2), \tag{3.5}$$

where n is the system density and N is the number of particles within a subsystem of volume V. This formulation is similar to the one used in the grand canonical ensemble (see Eq. (3.2)). Through careful consideration of the number fluctuations $\langle \Delta N\rangle^2$ within a given subvolume, the authors were able to predict the onset of MIPS by looking at the fluctuations as a function of system density for increasing levels of activity [22]. This study raises the natural question as to whether the compressibility can be computed through the other aforementioned methods for thermodynamic systems and whether the connections between these definitions—as depicted in Fig. 3.1—exist for active systems.

Using a combination of large-scale simulation and analytical theory, we focus on characterizing the compressibility of a suspension of active Brownian disks. The manuscript is organized as follows. In section 3.2, we define our implementation

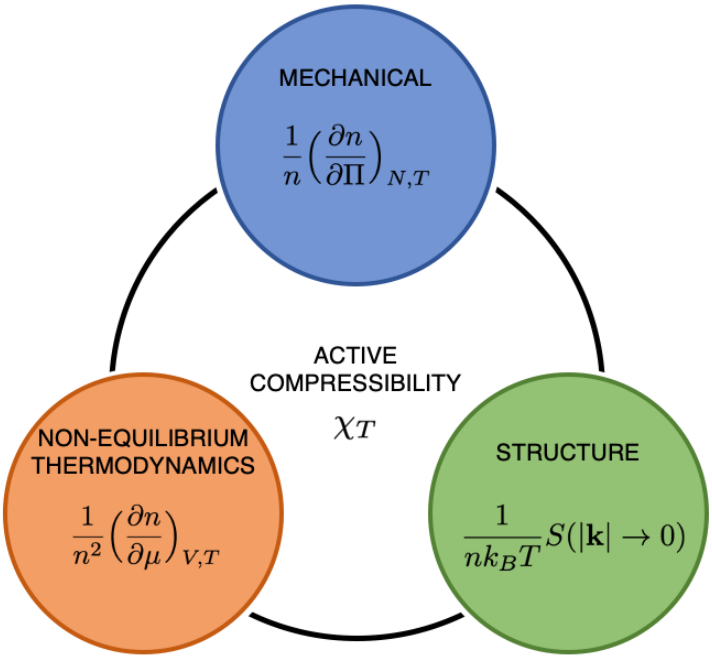

Figure 3.1: A postulated diagram of the compressibility in purely active systems with each method of calculation defined in the traditional thermodynamic sense.

of the active Brownian particle model and discuss all relevant details to performing large-scale simulation. In section 3.3, we introduce the notion of pressure and "isothermal" compressibility in active systems and directly compute these quantities from large scale simulation data for a wide range of volume fractions and activities. We explicitly demonstrate the divergence of the isothermal compressibility as the MIPS critical point is approached. In section 3.4, we motivate the validity of calculating isothermal compressibility from the definition of the structure factor for active Brownian particles, which provides an independent approach to computing compressibility directly from the fluid structure. In section 3.5, we present a comparison between the structural and mechanical definitions for compressibility and address the relation to an active chemical potential. Lastly, we summarize our work and discuss future directions in section 3.6.

3.2 Simulation Methods

We consider a suspension of monodisperse, athermal active particles of radii a. The active motion is characterized by an intrinsic swim velocity $U_0\mathbf{q}$—where $\mathbf{q}$ is the particle orientation—and a timescale for reorientation τ_R. We evolve the system forward in time using overdamped Langevin dynamics

$$0 = -\zeta \mathbf{U}_i + \mathbf{F}_i^{swim} + \sum_{i \neq j} \mathbf{F}_{ij}^{wca}, \tag{3.6}$$

$$0 = -\zeta_R \mathbf{\Omega}_i + \mathbf{L}_i^R, \tag{3.7}$$

where $\mathbf{U}_i$ is the velocity of particle i, $\mathbf{F}_{ij}^{wca}$ is the interparticle force for pair ij, $\mathbf{F}_i^{swim} = \zeta U_0 \mathbf{q}_i$ is the swim force, $\mathbf{\Omega}_i$ is the angular velocity of particle i, and ζ and ζ_R are the translational and rotational drag coefficients, respectively. The angular velocity relates to the evolution of particle orientations via $\partial \mathbf{q}_i / \partial t = \mathbf{\Omega}_i \times \mathbf{q}_i$. Normalizing position and time in Eqs. (3.6) and (3.7) by a and τ_R, respectively, gives rise to the nondimensional reorientation Péclet number $Pe_R \equiv a/(U_0 \tau_R)$, which measures the ratio of a particle's size to its run length $l = U_0 \tau_R$, the distance traveled between reorientation events [7]. Here we assume reorientations occur through a stochastic torque $\mathbf{L}^R$ governed by white noise statistics with zero mean and variance $2\zeta_R^2 \delta(t)/\tau_R$ and our particles interact via a Weeks-Chandler-Anderson (WCA) potential with cutoff radius $r_{cut} = (2a)2^{1/6}$. The depth of the potential is set such that $\epsilon = 200 F^{swim} a$.

The primary aim in this work is to understand the behavior of active systems in the supercritical region—above the critical point—and as such we explore phase space by varying Pe_R. To avoid introducing an additional force scale, we hold U_0 fixed and tune the persistence by varying τ_R. Importantly, as our active force is of finite amplitude, a sufficiently strong choice for the repulsive force $\mathbf{F}^{wca}$ will mimic a true hard-particle potential. A choice of $\epsilon/(F^{swim} a) = 200$ is found to result in hard-disk statistics with an effective average particle diameter of $2^{1/6}(2a)$. In this hard-disk limit, the state of our system is independent of the amplitude of the active force and is fully described by two geometric parameters: the area fraction $\phi = n\pi(2^{1/6}a)^2$ and the Péclet number Pe_R. Using τ_R to vary Pe_R ensure a well-defined area fraction for all activities, whereas variations in U_0 does not. Each simulation, unless otherwise specified, is run for $10{,}000\tau_R$ with a total number of 40,000 particles. All simulations were conducted using the HOOMD-Blue software package [23, 24].

3.3 Mechanical Compressibility

The mechanical pressure exerted by a suspension of active particles on its surroundings Π^{act} can be easily computed directly from the virial as

$$\Pi^{act} = \frac{1}{V}\sum_{i}^{N}\langle \mathbf{x}_i \cdot \mathbf{F}_i^{tot}\rangle, \tag{3.8}$$

where $\mathbf{F}_i^{tot}$ is the total force acting on particle i, $\mathbf{x}_i$ is the position of particle i, and $\langle ...\rangle$ denotes a time average. The total force acting on a given particle $\mathbf{F}_i^{tot} = \mathbf{F}_i^{swim} + \mathbf{F}_i^{col}$ arises from the particle's swimming motion and interparticle collisions ($\mathbf{F}_i^{col} = \sum_j \mathbf{F}_{ij}^{wca}$), respectively. It follows naturally that the virial can be decomposed into the individual pressure contributions:

$$\begin{aligned}\Pi^{act} &= \frac{1}{V}\sum_{i}^{N}\left[\langle \mathbf{x}_i \cdot \mathbf{F}_i^{swim}\rangle + \langle \mathbf{x}_i \cdot \mathbf{F}_i^{col}\rangle\right] \\ &= \frac{\tau_R}{2A}\sum_{i}^{N}(\mathbf{U}_i \cdot \mathbf{F}_i^{swim}) + \frac{1}{V}\sum_{i}^{N}\left[\langle \mathbf{x}_i \cdot \mathbf{F}_i^{col}\rangle\right] \\ &= \Pi^{swim} + \Pi^{coll}.\end{aligned} \tag{3.9}$$

The first term is the so-called swim pressure [25] (defined via the impulse formula [26, 27] in the second line) and the second is the typical collisional pressure as computed from the microscopic virial. The total pressure Π^{act} defined this way is a state function for spherical ABPs and its definition can be extended to unconfined systems where Π^{act} is equal to the internal bulk pressure. From this we are able to use this pressure from simulation at different points on the $Pe_R - \phi$ phase diagram to calculate the mechanical compressibility.

Figure 3.2 illustrates the behavior of χ_τ (Eq. (3.1)) as a function of ϕ for different Pe_R values. The compressibility is nondimensionalized by the ideal swim pressure written in terms of the activity $k_s T_s \equiv \zeta U_0^2 \tau_R/2$ [25]. The hard-disk compressibility (dashed line) as calculated by the first 10-terms of the virial expansion is shown for comparison. When $Pe_R > 1$, the compressibility is similar to that of passive hard-isk systems, even though no thermal translational motion is present. When $Pe_R < 1$ the compressibility becomes nonmonotonic and eventually diverges. The Pe_R value that is close to divergence is shown in the inset of Fig. 3.2. Here we note that the maximum compressibility changes by several orders of magnitude for a fractional change in Pe_R and thus we take this value to be the point of divergence. The divergence of χ_τ corresponds with the critical point, as supported by inspection of our simulations and the critical point presented by Takatori and Brady [7], with a critical Péclet number $Pe_R^{crit} \sim 0.04$ and volume fraction $\phi^{crit} \sim 0.58$.

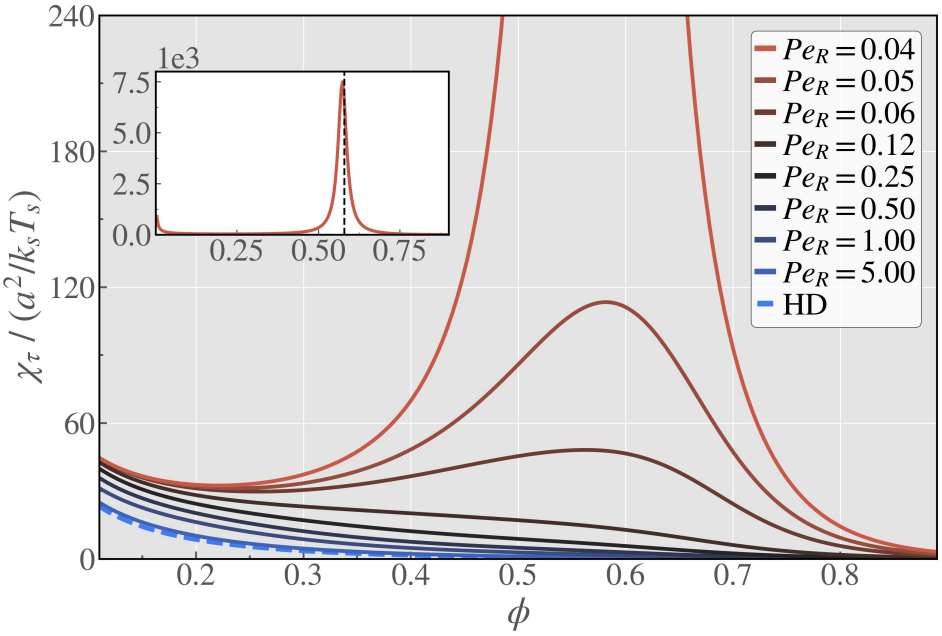

Figure 3.2: Mechanical compressibility χ_τ of 2D ABPs for various Pe_R as a function of volume fraction ϕ. The compressiblity for hard disks (dashed line)—as calculated by the 10-term virial expansion [28]—is shown for comparison. The inset shows χ_τ for $Pe_R = 0.04 \sim Pe_R^{crit}$.

3.4 Structure Factor

For equilibrium systems, the low wavenumber limit of the structure factor is related to isothermal compressibility via the compressibility equation (Eq. (3.3)). But this form of the compressibility equation is ill-defined in a purely active system as there is no notion of thermal energy. However, we can define the active compressibility via

$$S(|\mathbf{k}| \to 0) = nk_sT_s\chi_\tau, \tag{3.10}$$

where the thermal energy k_BT has been replaced with the activity k_sT_s as this is the relevant energy scale in the system. The form of Eq. (3.10) comes from a mechanical argument relating the static structure factor to the particle flux, following a similar framework outlined in [29]. (The full derivation can be found in Appendix 3.7.) Equation (3.10) can equivalently be written in terms of the radial distribution function $g(r)$

$$nk_sT_s\chi_\tau = 1 + n\int_V [g(r) - 1]d\mathbf{r}, \tag{3.11}$$

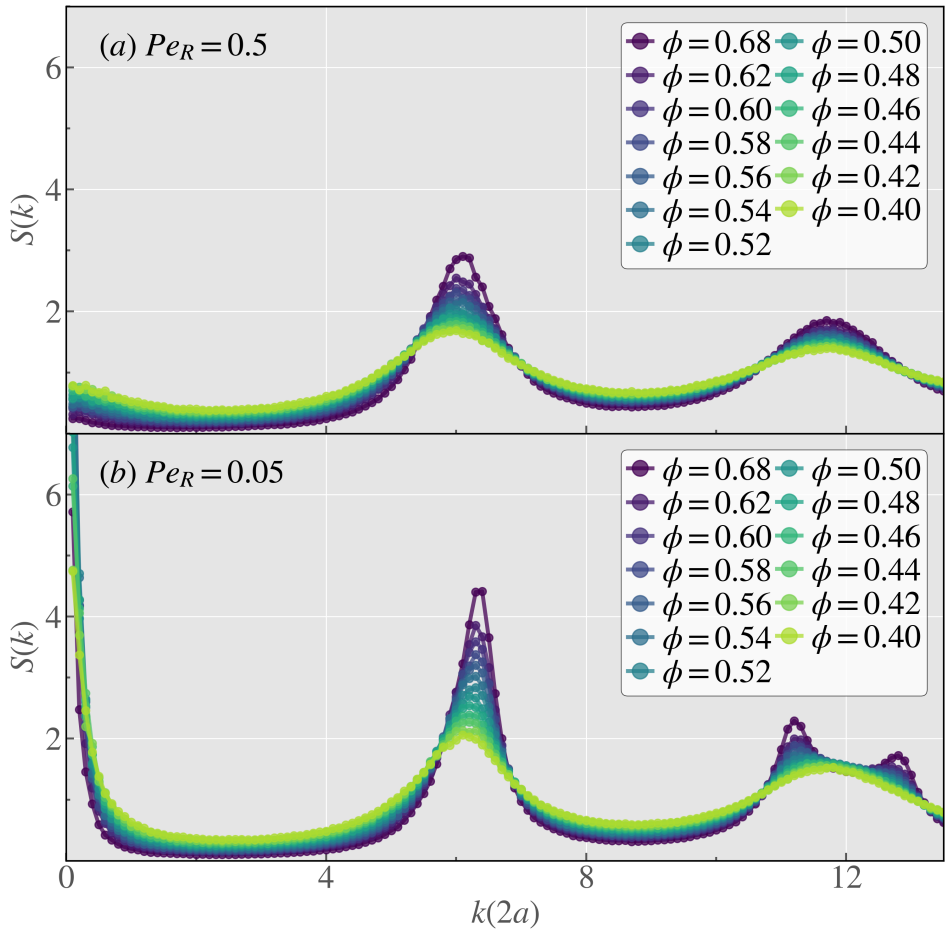

Figure 3.3: The static structure factor for a suspension of active Brownian particles over a range of volume fractions at (a) $Pe_R = 0.5$ and (b) $Pe_R = 0.05$.

where the integral is over the volume of the system. The definition of static structure factor does not rely on the detailed microscopic dynamics.

The static structure factor for two different values of Pe_R over a range of volume fractions is presented in Fig. 3.3. In weakly active systems, $Pe_R \sim 1$, the structure factor behaves similarly to that of a passive system and matches well with the results presented by De Macedo Biniossek et al. [30] (see Fig. 3.3(a)). At this level of activity $S(|\mathbf{k}| \to 0)$ never diverges. However, as the activity increases towards the critical activity level (Fig. 3.3b) $S(\mathbf{k})$ begins to diverge as $|\mathbf{k}| \to 0$ at the same critical density that was predicted in Fig. 3.2, indicating a phase transition. This result is not surprising as the structure factor in this limit is a measure of the long-range density fluctuations and should coincide with the mechanical compressibility (Eq. (3.1)) as we approach the critical point.

3.5 Compressibility Comparison

Thus far we have shown that compressibility computed from the fluid structure matches the mechanical definition near the critical point, but we would like to know how the two compare throughout the homogeneous supercritical regime for active fluids. Figure 3.4 presents the compressibility computed via gradients in the active pressure (solid lines; Eq. (3.1)) and from the static structure factor through the use of Eq. (3.10) (symbols). Due to the finite size of our simulations, the Nyquist sampling frequency dictates the minimum wavenumber value that can be probed $k_{min} = 2\pi/L$, where L is the size of the system. Therefore, the structure factor in the small wavenumber limit $\mathbf{k} \to 0$ was fit using the expansion $S(\mathbf{k}) = S(0)/(1+\xi_{OZ}^2 k^2)$, where $S(0)$ and ξ_{OZ} were used as fitting parameters, with ξ_{OZ} being the Ornstein-Zernike correlation length [8, 31]. The error bars represent the 95% confidence interval for the fitting parameter. The error increases as activity increases due to larger long-range density fluctuations as the critical point is approached. The uncertainty resulting from these fluctuations can be reduced with larger system size as this lowers the minimum possible sampling frequency.

The strong agreement between the different definitions of compressibility shows that there is meaning in the thermodynamic relations—even though the system is far from equilibrium—when using the appropriate energy scale. This is also evidence that compressibility behaves as a traditional thermodynamic response function even for an active system. The notion that compressibility gives relevant information for the phase behavior of the system also implies that the active pressure is the relevant quantity necessary to construct an equation of state for active disks.

Until now we have not considered the proposed non-equilibrium definition via the chemical potential for compressibility. Chakraborti *et al.* have shown—through the property of additivity—the existence of a general scalar $\mu^{act}(n)$ which is tied to density fluctuations in the system [22]. As such, this scalar can be related to the compressibility via the structure factor and, from the equivalence shown here, to the pressure, giving rise to a “thermodynamics" of active matter (outlined in orange in Fig. 3.1). From Eqs. (3.1), (3.2), (3.4), and (3.5) it follows that

$$n\frac{\partial \mu^{act}}{\partial n} = \frac{\partial \Pi^{act}}{\partial n}, \tag{3.12}$$

an equation first proposed by Takatori and Brady [7] based on arguments of particle

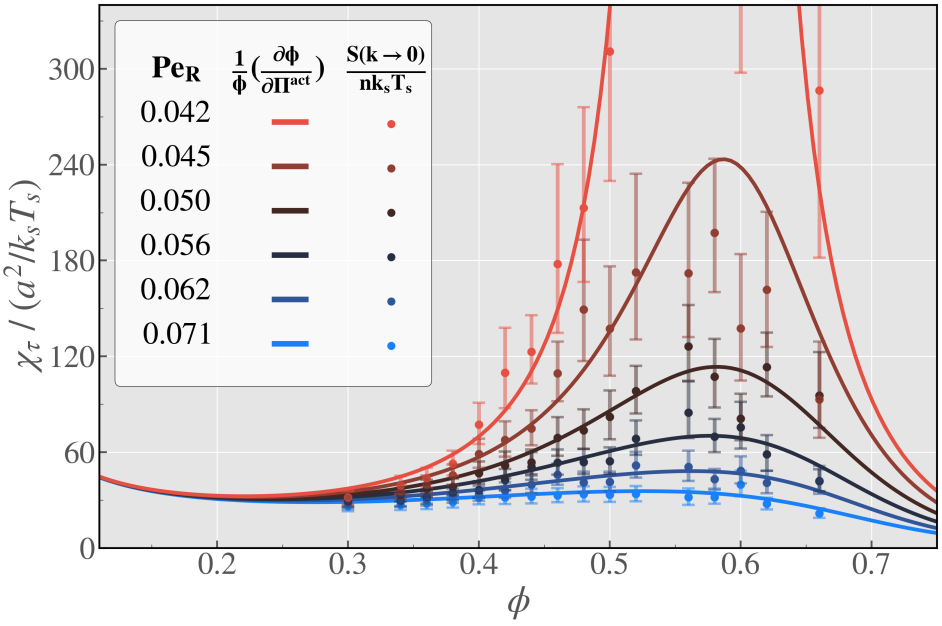

Figure 3.4: Compressibility of active systems at varying levels of activity Pe_R = 0.071, ..., 0.042 computed mechanically from derivatives of the pressure (solid lines) and structurally using the compressibility equation (symbols).

flux driven by stress gradients (see Appendix 3.7). [1]

This active chemical potential μ^{act} predicts the critical point [7] and the existence of a binodal. Since the chemical potential agrees with the mechanical compressibility above the critical point [7, 22], it implies that a thermodynamic relation can be defined and used. However, the same relation does not hold below the critical point. Equation (3.12) implies a Maxwell construction which overestimates the coexistence pressure in the two-phase region [32]. The inaccuracy of the binodal prediction indicates that the standard Gibbs-Duhem relation (Eq. (3.12)) is inadequate for phase coexistence and that an additional contribution is needed.

From our comparison between the active compressibility computed via the structure factor and the active pressure, we know that they are only equivalent if the swim pressure is included in the equation of state. It is known that swim pressure jumps at interfaces—like those present at phase boundaries. This suggests that the non-negligible jump in swim pressure at the phase interface must be accounted for to accurately determine the phase behavior below the critical point, implying that the interface acts as an extensive property for active Brownian particles, while it does

[1] Takatori and Brady considered ABPs in an incompressible fluid and therefore had a factor of $(1 - \phi)$ accounting for the flux of fluid in response to a flux of particles.

not for passive particles. Including contributions from the phase interface when constructing an active chemical potential should be required to arrive at the correct coexistence pressure in the two-phase region, while simultaneously not altering predictions above the critical point.

3.6 Conclusions and Future Work

We have computed the compressibility for an athermal, active suspension mechanically—using pressure—and structurally from the static structure factor. In order to compute compressibility for active systems from structure we have utilized a mechanical argument to motivate an active form of the compressibility equation. From this we have shown that compressibility behaves like a thermodynamic response function, as it does in equilibrium systems, so long as the swim pressure is accounted for in the total system pressure. As activity varies, the compressibility continuously deviates from the 2D hard-disk behavior and diverges at the onset of MIPS, thus reinforcing the idea that the compressibility behaves like a response function and can be used to determine phase behavior.

We have also discussed the existence of an active chemical potential which is linked to number fluctuations in the system as shown in Chakraborti *et al*. [22]. This active chemical potential, while useful in the region before the onset of phase separation, does not accurately capture the location of the binodal. This result hints at the importance of the phase interface to determine behavior in active systems, as speculated by Solon et al. [33], a surprising requirement not observed in passive systems.

While our focus has been on compressibility, its behavior as a thermodynamic response function suggests that other response functions are worth exploring in active systems. Compressibility serves as a natural starting point as it can be mechanically defined, but perhaps there are active analogues to other familiar thermodynamic response functions, especially considering the evidence for a non-equilibrium chemical potential and thus a non-equilibrium free energy. There have been predictions to the form of an active heat capacity [7], but to our knowledge there have been no further explorations into active analogues to thermodynamic response functions.

Appendix

3.7 Active Compressibility Equation

Here we present the motivation for Eq. (3.10), the active compressibility equation. Following the derivation outlined by Leshansky and Brady [29], we begin with

the dynamic structure factor (DSF) $F(\mathbf{k},t) = \langle \sum_{\alpha,\beta} \exp[i\mathbf{k}\cdot(\mathbf{x}_\alpha(t) - \mathbf{x}_\beta(0))]\rangle/N$, where $\mathbf{k}$ is the wavenumber, the sum is over particle pairs (α,β), and the angular brackets denote an ensemble average. It has been shown that the collective diffusivity of a suspension can be obtained by computing the time derivative of the DSF via $\dot{F} - i\mathbf{k}\cdot\tilde{\mathbf{U}}^* F = -\mathbf{k}\cdot\hat{\mathbf{D}}^{coll}(\mathbf{k})F$, where $\tilde{\mathbf{U}}^*$ is the bulk average velocity at an arbitrary point in the suspension and $\hat{\mathbf{D}}^{coll}(\mathbf{k})$ is the Fourier transform of the collective diffusivity [29]. In the long wavelength limit (when density fluctuations persist for longer than the size of a particle), as $\mathbf{k} \to 0$, $F(\mathbf{k},t) \sim S(\mathbf{k})$ and $\hat{\mathbf{D}}^{coll}$ is given by

$$\hat{\mathbf{D}}^{coll} = \lim_{\mathbf{k}\to 0} \frac{1}{NS(\mathbf{k})} \Big\langle \sum_{\alpha,\beta} \mathbf{M}_{\alpha\beta} e^{i\mathbf{k}\cdot(\mathbf{x}_\alpha(t) - \mathbf{x}_\beta(t))} \Big\rangle, \tag{3.13}$$

where $\mathbf{M}_{\alpha\beta} = \int_{t'=0}^{t} \mathbf{U}'_\alpha(t)\mathbf{U}_\beta(t')dt'$ is the mobility and $\mathbf{U}'_\alpha = \mathbf{U}_\alpha - \langle\mathbf{U}\rangle$ is the configuration dependent velocity fluctuation of particle α, as presented by Leshansky and Brady [29]. The velocities can be decomposed into contributions from interparticle interactions and swimming $\mathbf{U}_\alpha = \mathbf{U}^P_\alpha + \mathbf{U}^{swim}_\alpha$, which allows the velocity correlation function to be decomposed into interparticle-interparticle, swim-swim, and swim-interparticle components. The swim-swim correlation function results in the swim diffusivity $\mathbf{D}^{swim} = (U_0^2\tau_R/2)\mathbf{I}$ [25] because only self-terms are correlated, and the interparticle-interparticle correlation goes to 0 for pairwise interactions. This gives

$$\begin{aligned} \hat{\mathbf{D}}^{coll} = \frac{1}{S(\mathbf{k}\to 0)} \Big(& D^{swim}\mathbf{I} \\ & + \frac{1}{N} \Big\langle \sum_{\alpha,\beta} \int \mathbf{U}^P_\alpha(t)\mathbf{U}^{swim}_\beta(t')dt' \Big\rangle \Big). \end{aligned} \tag{3.14}$$

It is important to note that were this a system of passive Brownian particles, then D^{swim} would be replaced by D_T and Brownian contributions would replace those from swimming in the above correlation functions, with the interparticle-Brownian velocity correlation function being 0. For simplicity we will assume the second term on the right hand side of Eq. (3.14) is 0 as it would be for Brownian motion. Now we can relate $\mathbf{D}^{coll}$ to the pressure through a suspension momentum balance

$$0 = -\zeta n(\mathbf{u}_p - \langle\mathbf{u}\rangle) + \nabla\cdot\sigma^p, \tag{3.15}$$

where $n(\mathbf{u}_p - \langle\mathbf{u}\rangle) = \mathbf{j}^{rel}$ is the relative flux, $\mathbf{u}_p$ is the particle velocity, $\langle\mathbf{u}\rangle = \phi\mathbf{u}_p + (1-\phi)\mathbf{u}_f$ is the suspension averaged velocity, $\mathbf{u_f}$ is the fluid velocity, and $\sigma^p = -\Pi\mathbf{I}$ is the particle stress written in terms of pressure. The relative flux is

representable as a generalized Fick's law $\mathbf{j}^{\mathbf{rel}} = -\int \mathbf{D}^{coll}(\mathbf{x}-\mathbf{x}') \cdot \nabla n(\mathbf{x}', t) d\mathbf{x}'$ with a nonlocal diffusivity given by the collective diffusivity. Substituting this definition into Eq. (3.15) gives

$$\begin{aligned} -\int \mathbf{D}^{coll}(\mathbf{x}-\mathbf{x}') \cdot \nabla n(\mathbf{x}', t) d\mathbf{x}' &= \frac{1}{\zeta} \nabla \cdot \sigma^p \\ &= \frac{1}{\zeta} \frac{\partial \sigma^p}{\partial n} \cdot \nabla n. \end{aligned} \tag{3.16}$$

Combining Eq. (3.14) and (3.16) in the limit $\mathbf{k} \to 0$ gives

$$\hat{\mathbf{D}}^{coll}(\mathbf{k} \to 0) = \frac{1}{\zeta} \Big(\frac{\partial \Pi}{\partial n} \Big) \mathbf{I} = \frac{D^{swim} \mathbf{I}}{S(\mathbf{k} \to 0)}. \tag{3.17}$$

Using the definition for mechanical compressibility results in the well known compressibility equation [3, 29, 34]

$$S(\mathbf{k} \to 0) = n\zeta D^{swim} \chi_\tau = n k_s T_s \chi_\tau, \tag{3.18}$$

expressed in terms of the activity $k_s T_s$ instead of the thermal energy $k_B T$, as presented in Section 3.4. A more detailed discussion regarding this derivation and its origins can be found in Leshansky and Brady [29].

References

[1] P. G. Debenedetti, F. Sciortino, and G. H. Zerze, "Second critical point in two realistic models of water", Science (New York, N.Y.) **369**, 289–292 (2020).

[2] D. Bolmatov, V. V. Brazhkin, and K. Trachenko, "Thermodynamic behaviour of supercritical matter", Nature Communications **4**, 1–7 (2013).

[3] H. E. Stanley, *Introduction to Phase Transitions and Critical Phenomena* (Oxford University Press, 1971).

[4] L. E. Reichl, *A Modern Course in Statistical Physics* (Wiley-VCH Verlag GmbH & Co. KGaA, Weinheim, Germany, Apr. 2016).

[5] J. Palacci, S. Sacanna, A. P. Steinberg, D. J. Pine, and P. M. Chaikin, "Living Crystals of Light-Activated Colloidal Surfers", en, Science **339**, 936–940 (2013).

[6] A. Zöttl and H. Stark, "Emergent behavior in active colloids", Journal of Physics: Condensed Matter **28**, 253001 (2016).

[7] S. C. Takatori and J. F. Brady, "Towards a thermodynamics of active matter", en, Physical Review E **91**, 032117 (2015).

[8] Y. Fily and M. C. Marchetti, "Athermal Phase Separation of Self-Propelled Particles with No Alignment", Physical Review Letters **108**, 235702 (2012).

[9] C. Bechinger, R. Di Leonardo, H. Löwen, C. Reichhardt, G. Volpe, and G. Volpe, "Active Particles in Complex and Crowded Environments", Reviews of Modern Physics **88**, 045006 (2016).

[10] J. U. Klamser, S. C. Kapfer, and W. Krauth, "Thermodynamic phases in two-dimensional active matter", Nature Communications **9** (2018).

[11] S. A. Mallory, C. Valeriani, and A. Cacciuto, "An Active Approach to Colloidal Self-Assembly", Annual Review of Physical Chemistry **69**, 59–79 (2018).

[12] L. Berthier, E. Flenner, and G. Szamel, "How active forces influence nonequilibrium glass transitions", New Journal of Physics **19** (2017).

[13] S. Paliwal, V. Prymidis, L. Filion, and M. Dijkstra, "Non-equilibrium surface tension of the vapour-liquid interface of active Lennard-Jones particles", The Journal of Chemical Physics **147**, 084902 (2017).

[14] S. K. Nandi and N. S. Gov, "Nonequilibrium mode-coupling theory for dense active systems of self-propelled particles", Soft Matter **13**, 7609–7616 (2017).

[15] M. Feng and Z. Hou, "Mode coupling theory for nonequilibrium glassy dynamics of thermal self-propelled particles", Soft Matter **13**, 4464–4481 (2017).

[16] V. Prymidis, S. Paliwal, M. Dijkstra, and L. Filion, "Vapour-liquid coexistence of an active Lennard-Jones fluid", The Journal of Chemical Physics **145**, 124904 (2016).

[17] M. Paoluzzi, C. Maggi, U. Marini Bettolo Marconi, and N. Gnan, "Critical phenomena in active matter", Physical Review E **94**, 052602 (2016).

[18] B. Partridge and C. F. Lee, "Critical motility-induced phase separation belongs to the Ising universality class", Physical Review Letters **123**, 068002 (2018).

[19] J. T. Siebert, F. Dittrich, F. Schmid, K. Binder, T. Speck, and P. Virnau, "Critical behavior of active Brownian particles", Physical Review E **98** (2018).

[20] P. F. McMillan and H. E. Stanley, "Going supercritical", Nature Physics **6**, 479–480 (2010).

[21] M. Herrero, J. A. Mendiola, A. Cifuentes, and E. Ibáñez, *Supercritical fluid extraction: Recent advances and applications*, Apr. 2010.

[22] S. Chakraborti, S. Mishra, and P. Pradhan, "Additivity, density fluctuations, and nonequilibrium thermodynamics for active Brownian particles", Physical Review E **93**, 052606 (2016).

[23] J. A. Anderson, C. D. Lorenz, and A. Travesset, "General purpose molecular dynamics simulations fully implemented on graphics processing units", Journal of Computational Physics **227**, 5342–5359 (2008).

[24] J. Glaser, T. D. Nguyen, J. A. Anderson, P. Lui, F. Spiga, J. A. Millan, D. C. Morse, and S. C. Glotzer, "Strong scaling of general-purpose molecular dynamics simulations on GPUs", Computer Physics Communications **192**, 97–107 (2015).

[25] S. C. Takatori, W. Yan, and J. F. Brady, "Swim Pressure: Stress Generation in Active Matter", en, Physical Review Letters **113**, 028103 (2014).

[26] Y. Fily, Y. Kafri, A. P. Solon, J. Tailleur, and A. Turner, "Mechanical pressure and momentum conservation in dry active matter", Journal of Physics A: Mathematical and Theoretical **51** (2018).

[27] A. Patch, D. M. Sussman, D. Yllanes, and M. C. Marchetti, "Curvature-dependent tension and tangential flows at the interface of motility-induced phases", Soft Matter **14**, 7435–7445 (2018).

[28] N. Clisby and B. M. McCoy, "Ninth and tenth order virial coefficients for hard spheres in D dimensions", Journal of Statistical Physics **122**, 15–57 (2006).

[29] A. M. Leshansky and J. F. Brady, "Dynamic structure factor study of diffusion in strongly sheared suspensions", Journal of Fluid Mechanics **527**, 141–169 (2005).

[30] N. De Macedo Biniossek, H. Löwen, T. Voigtmann, and F. Smallenburg, "Static structure of active Brownian hard disks", Journal of Physics Condensed Matter **30** (2018).

[31] D. Stopper, H. Hansen-Goos, R. Roth, and R. Evans, "On the decay of the pair correlation function and the line of vanishing excess isothermal compressibility in simple fluids", Journal of Chemical Physics **151** (2019).

[32] S. Paliwal, J. Rodenburg, R. Van Roij, and M. Dijkstra, "Chemical potential in active systems: Predicting phase equilibrium from bulk equations of state?", New Journal of Physics **20**, 015003 (2018).

[33] A. P. Solon, J. Stenhammar, M. E. Cates, Y. Kafri, and J. Tailleur, "Generalized thermodynamics of phase equilibria in scalar active matter", Physical Review E **97**, 020602 (2018).

[34] J. P. Hansen and I. R. McDonald, *Theory of Simple Liquids: With Applications to Soft Matter: Fourth Edition* (Elsevier Ltd, 2013).

Chapter 4

MACHINE LEARNING FOR PHASE BEHAVIOR IN ACTIVE MATTER SYSTEMS

We demonstrate that deep learning techniques can be used to predict motility induced phase separation (MIPS) in suspensions of active Brownian particles (ABPs) by creating a notion of phase at the particle level. Using a fully connected network in conjunction with a graph neural network we use individual particle features to predict to which phase a particle belongs. From this, we are able to compute the fraction of dilute particles to determine if the system is in the homogeneous dilute, dense, or coexistence region. Our predictions are compared against the MIPS binodal computed from simulation. The strong agreement between the two suggests that machine learning provides an effective way to determine the phase behavior of ABPs and could prove useful for determining more complex phase diagrams.

This chapter includes content from our previously published article:

[1] A. R. Dulaney and J. F. Brady, "Machine Learning for Phase Behavior in Active Matter Systems",
A.R.D. participated in the conception of the project, developed the models, analyzed the data, and participated in the writing of the manuscript. (2020),

4.1 Introduction

Since its inception, the field of active matter has been dominated by studies of motility-induced phase separation (MIPS). The majority of these studies focus on developing a theoretical framework to describe clustering behavior and the accumulation of active particles at boundaries. Due to the striking similarities between classical and active phase behavior, the creation of thermodynamic-like frameworks has been of particular interest but continues to be a source of debate [1–5]. A key difficulty surrounding this approach is the lack of a well-defined notion of temperature and free energy—as these systems are far from equilibrium—which results from the intrinsic swimming motion of active particles.

Adhering to the structure of traditional thermodynamic frameworks has resulted in several definitions of a non-equilibrium chemical potential [6–8], each of which predicts an active binodal but fails to predict the correct coexistence pressure measured inside the phase envelope from simulation. The shortcomings with the current chemical potential definitions do not preclude its existence but necessitate alternative measures for determining the phase boundaries. Large scale computer simulations provide a means to computing system pressure, which can provide insights into the phase behavior through the mechanical instability criterion. While this method is robust and has shown great success [2, 9, 10], it inherently has a steep trade-off between accuracy and computational cost. Determination of the phase boundary requires the change in system pressure with volume fraction to be zero. To make such a judgment one either needs to finely sweep volume fraction space or rely on fitting functions to smoothly fit the pressure data. Both methods are highly dependent on the quality of the pressure data obtained at each point in phase space, and large fluctuations in active pressure make this a difficult task, especially deep in the coexistence region [2, 9].

To overcome these limitations we turn towards methods used to characterize other inherently complex materials. Recently, there has been a surge of interest in using machine learning algorithms to aid in material characterization [11–14]. While early studies were predominantly interested in materials containing explicit symmetries or those confined to two-dimensional lattices [11, 12], there has been some development in classifying amorphous materials [14].

In this study, we leverage the developments in machine learning to aid in characterizing the observed phase behavior in suspensions of active Brownian particles (ABPs). ABPs are an important minimal model system for determining the behavior

of self-propelled colloids, bacteria, and other living organisms. The key feature that distinguishes an active colloid from a passive one is the driven and persistent nature of its motion. This distinct characteristic of its dynamics gives rise to a wealth of interesting behaviors including self-assembly [15], clustering [16, 17], and motility-induced phase separation [1–5]. As such, active materials have garnered interest from the chemical and material science communities for novel drug delivery methods, remediation strategies, and material design methods at the microscale [15, 18, 19].

Due to the nonequilibrium nature of these systems, it is difficult to develop analytic theories that can accurately predict the more complex collective behaviors. Thus, we look towards machine learning to aid in this endeavor. Machine learning algorithms are capable of discerning difficult—and potentially nonintuitive—nonlinear relationships among system variables, which would otherwise go unnoticed. These algorithms also have the benefit of readily handling multi-body correlations, which are exceptionally taxing or intractable through traditional analytic means.

Using a combination of deep learning and large-scale simulation, we focus on characterizing the phase behavior of particles in a suspension of active Brownian disks. We use machine learning to predict particle phase at a per particle level for simulations conducted at different regions in phase space. We then use these phase labels to get an estimate for the fraction of particles in each phase present at a given point in phase space. This fraction is then used to determine the system phase behavior. The chapter is outlined as follows. In section 4.2 we define the implementation of the active Brownian particle model used in our simulations. We then outline the datasets generated for use in our machine learning model in section 4.2. Here we also discuss the feature selection used for our machine learning model. In section 4.2, we describe the machine learning model architecture used in this work and provide details on the training procedures. In section 4.2, we discuss the input features used for our model. In section 4.3, we discuss the representation of our simulation snapshots as graphs. In section 4.4, we present our results in the form of predictions of the phase behavior for suspensions of ABPs at different regions in the phase diagram. Finally, in section 4.5 we discuss the implications of this work and future directions.

4.2 Methods

Simulation Details

Suspensions of monodispersed, purely active particles are modeled using the active Brownian particle (ABP) model. The active motion is characterized by an intrinsic swim velocity $\mathbf{U_0} = U_0\mathbf{q}$—where $\mathbf{q}$ is the particle orientation—which reorients on a timescale τ_R. Particles of radius a interact through a Weeks-Chandler-Anderson (WCA) potential with cutoff radius $r_{cut} = (2a)2^{1/6}$ and depth $\epsilon = 200F^{swim}a$, where $F^{swim} = \zeta U_0$ is the magnitude of the force resulting from the product of the translational drag ζ and swim velocity. Here we assume particles reorient via a stochastic torque $\mathbf{L}^R$ governed by zero-mean white noise statistics with variance $2\zeta_R^2\delta(t)/\tau_R$, where ζ_R is the rotational drag coefficient. Particle positions and orientations can be evolved in time using overdamped Langevin dynamics

$$0 = -\zeta\mathbf{U}_i + \mathbf{F}_i^{swim} + \sum_{i\neq j}\mathbf{F}_{ij}^P, \tag{4.1}$$

$$0 = -\zeta_R\mathbf{\Omega}_i + \mathbf{L}_i^R, \tag{4.2}$$

where $\mathbf{F}_i^{swim} = \zeta U_0\mathbf{q}_i$ is the swim force of particle i, $\mathbf{F}_{ij}^P$ is the interparticle force between pair i, j, $\mathbf{U}_i$ is the velocity, $\mathbf{\Omega}_i$ is the angular velocity, and ζ and ζ_R are the translational and rotational drags, respectively. The angular velocity is related to the particle orientation by $\partial\mathbf{q}_i/\partial t = \mathbf{\Omega}_i\times\mathbf{q}_i$. Normalizing position and time by a and τ_R, respectively, results in the dimensionless reorientation Péclet number $Pe_R \equiv a/l$, which is the ratio of a particle's size to its persistence length $l = U_0\tau_R$—the distance traveled between reorientation events [2].

We performed independent simulations of 40,000 particles for $10{,}000\tau_R$ for various combinations of the two governing nondimensional parameters: the packing fraction ϕ and Pe_R. To avoid introducing an additional force scale Pe_R was varied by changing τ_R at a fixed value of U_0. All simulations were conducted using the HOOMD-Blue software package [20, 21]. Hydrodynamic interactions have been neglected.

Datasets

Our machine learning model is structured to predict phase identity at a per particle level, similar to what was done by Ha *et al.* [22]. This results in a binary classification task in which particles can be members of the gas phase or the dense phase. For

simplicity, we ignore the second-order hexatic transition present in two-dimensional hard disk systems and treat the hexatic phase as part of the dense phase.

We use the simulations outlined in section 4.2 to produce datasets for each point in phase space represented by a (ϕ, Pe_R) pair. For each of these phase points, we look at 6 snapshots spaced roughly $1{,}000\tau_R$ apart. From these snapshots, we construct a feature set for each phase point which consists of 240,000 entries. Predictions of the phase behavior at each phase point are averaged across each of the 6 time points to reduce bias from a single configuration.

Learning Framework

Here we give a brief overview of neural networks and describe the architecture and training routine used in this work.

Neural networks have shown great potential for predicting particle phase for both two-state and amorphous phase-separated systems [13, 14]. The most common neural network employed is the fully connected feedforward network. Feedforward networks are composed of layers of transformations modified by nonlinear functions. These layers can be stacked resulting in the output of one layer acting as the input of the following layer. The basic form for a layer f is $f(x) = g(Wx+b)$, where g is the nonlinear activation function, x is the vector input data, W is the weight matrix, and b is a vector of biases. When constructing a fully connected network the activation functions g for each layer need not be the same, and additional regularization terms can be added to prevent overfitting to training data. Some common activation functions are the sigmoid, hyperbolic tangent, and rectified linear unit (ReLU), defined as $g(x) = max(0, x)$. Once constructed, a network is given an objective, or loss, function to minimize and updates the weight and bias terms through either gradient descent [1] or a more sophisticated algorithm like Adam [23]. Here we are interested in a binary classification and thus use binary cross entropy to compute loss

$$L = -(y \log(p) + (1 - y) \log(1 - p), \tag{4.3}$$

where L is the loss, y is the binary indicator of whether the positive class is the

[1] Gradient descent is an iterative method for locating the local minimum of a function by determining the steepest gradient of the function with respect to its independent variables. In this context gradient descent is used with backpropagation, which relates the weights of each layer in the neural network back to the loss function so the entire network can be updated during each iteration.

correct label for a given observation, and p is the probability that an observation is of the positive class.

Recent advances in machine learning have resulted in the adoption of graph convolutional neural networks (GNNs), which utilize graph theory to add information on the spatial proximity of training data [24–26]. These are similar to traditional convolutional neural networks (CNNs), which rely on convolution and connected layers to make predictions. The primary uses for CNNs have been been in the areas of computer vision and natural language processing, due to the inherent structure of image and text data. Similarly, GNNs use convolutions and the inherent structure of the data, but adjacent training points need not be distributed on a rectilinear grid like an image or sequentially like in text [26]. In both architectures, the input matrix is convolved with a set of matrices—the convolution layer—to produce output matrices. These convolution layers are equivariant under translation and rotation, making them highly effective at learning abstract features of an image or graph while simultaneously reducing the number of parameters.

The amorphous configurations found in particle-based phase-separated systems can benefit from traditional CNNs [14], but this requires spatial discretization of the system which may vary with particles of different sizes. We avoid this when looking at MIPS in active disks by using a GNN to provide information on the local structure to the network.

Our training and model architecture is as follows. We first train a supervised deep neural network (DNN) on data in the single-phase region above the critical point. After the supervised network is trained, we predict particle labels for a simulation of interest. These predictions are then taken and those that predict the phase with a >90% confidence are used as seed labels in a semi-supervised GNN. We then take the simulation snapshot and represent it as a graph, which we will discuss in more detail in section 4.3. We then train a GNN for each graph. The training in this step is structured as a transductive, or semi-supervised, learning problem. For each graph we use the seeded particle (node) labels to propagate labels to the remainder of the graph. We use the same features from the DNN, but instead of learning a very general problem, we are using confidently labeled particles to influence the labels given to their neighbors. In this work, we use the graph attention network (GAT) architecture [25] for our GNNs implemented using the DGL software package [27]. The resulting prediction from the GNN is then weighted against the prediction provided by the DNN in the first step.

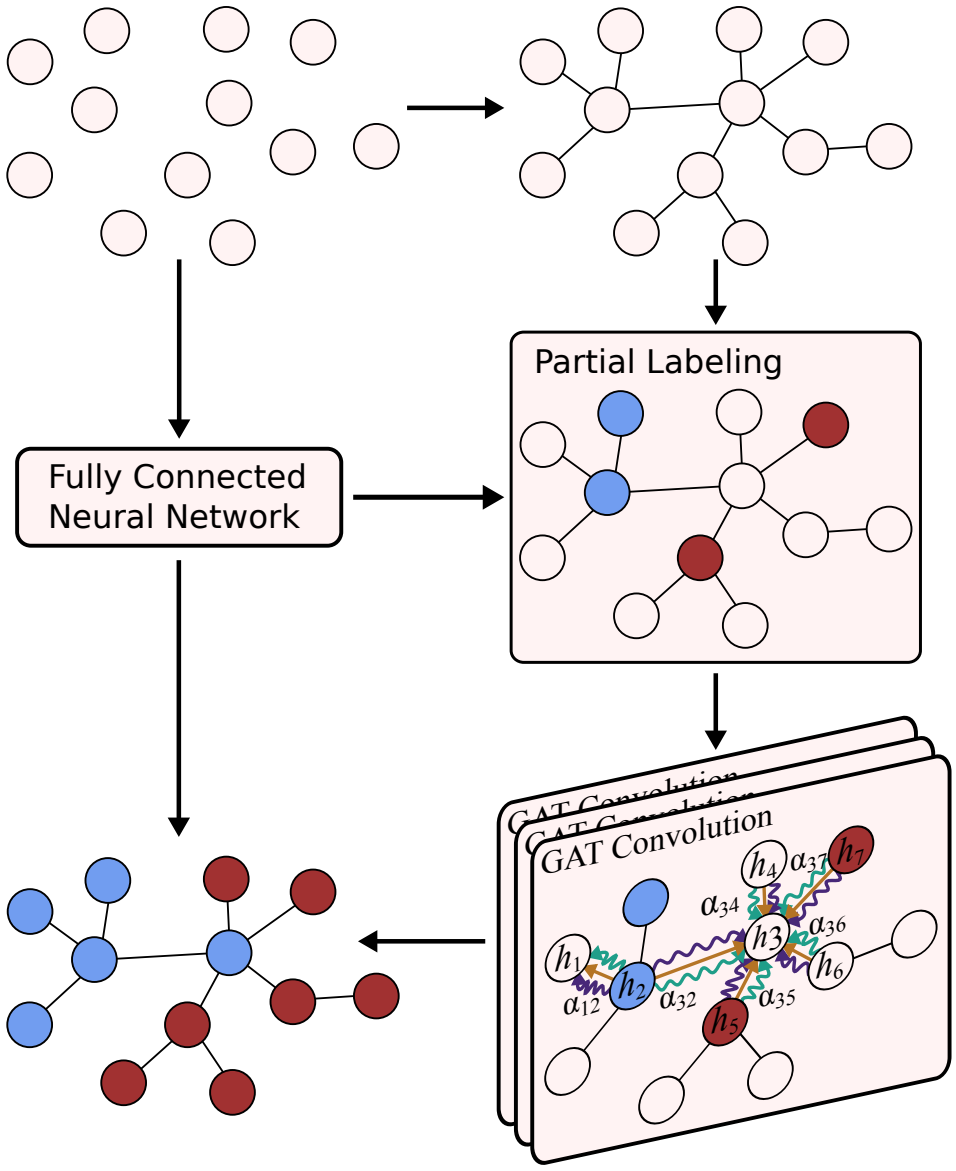

Figure 4.1: The learning architecture used in this work to predict particle phase labels. First, a particle feature matrix is fed into a fully connected DNN. Simultaneously particles are connected to form a graph structure. The graph is partially labeled using the most confident (>90%) labels from the DNN and is then used with the feature matrix as inputs into a GNN consisting of three GAT convolution layers with a final softmax activation function. The resulting label probabilities from the GNN are then averaged with the label probabilities output from the DNN to achieve the final label probabilities. Each particle is then given the most probable label.

A flowchart of our learning process is outlined in Fig. 4.1. The purple, orange, and teal lines of the GAT convolution represent the different attention heads for the layer. Each attention head serves as a means to create feature abstractions [25]. The coefficients $\alpha_{i,j}$ are learned weight parameters which determine the weighted importance of neighbor j on particle i. The attention heads from each node are then concatenated or averaged to produce the layer output, which may be a label probability or feature abstraction. Details of the GAT implementation can be found in reference [25]. Further details of the model architecture used in this work are presented in appendix 4.7.

Feature Selection

In order to label individual particles, our feature space is limited to quantities that can be computed on a per-particle basis. This includes Voronoi volume, the number of first shell Voronoi neighbors, and the average of first shell Voronoi volumes. We repeat this averaging process for the second and third shell neighbors as well to incorporate information about the local environment. We also include the hexatic and translational order parameters defined as $\psi_6(i) = 1/n \sum_j^n e^{\mathrm{i}6\theta_{ij}}$ and $G_6(\mathbf{r}_{ij}) = \sum_j^n \psi_6(i) \cdot \psi_6^*(j)$, respectively, where n is the number of Voronoi neighbors, $\mathbf{r}_{ij}$ is the vector connecting pair ij, θ_{ij} is the angle between $\mathbf{r}_{ij}$ and the reference vector $(0, 1)$, and $\psi_6^*(i)$ is the complex conjugate of the hexatic order parameter. The Voronoi volumes and the hexatic and translational order parameters were computed using the Freud analysis software [28]. In order to account for some of the dynamics we include the force-orientation autocorrelation $\mathbf{F}_i \cdot \mathbf{q}_i$ and the particle speed $\mathbf{U}_i = \mathbf{F}/\zeta$.

Our initial set of features is paired down using a boosted random forest to remove highly collinear features in order of importance. The final feature set is comprised of the Voronoi volume, number of third shell neighbors, hexatic order parameter, translational order parameter, and the force-orientation autocorrelation in order of importance. The process of removing collinear features is discussed further in appendix 4.6 and the correlation matrices for the full and final feature sets are shown in Fig. 4.5. It is interesting to note that the number of third shell neighbors is ranked highly in importance because the model might be learning the order-disorder hexatic transition. Lastly, we take each of our features and average them across all first shell neighbors to create an additional set of aggregate features. This aggregation step improved the performance and training stability of our DNN in the first step of our model.

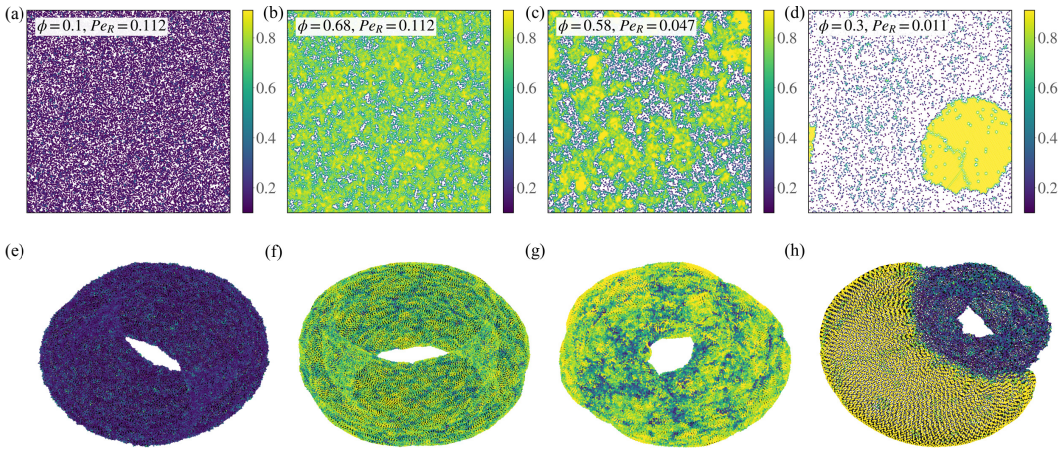

Figure 4.2: Simulation snapshots and respective graph structures for different regions of phase space colored by particle Voronoi volume. We look at the weakly active ($Pe_R \sim 0.11$) (a),(e) dilute and (b),(f) dense regions, (c),(g) the region near the critical point ($P_R \sim 0.047$), and (d),(h) deep within the coexistence region ($Pe_R \sim 0.011$).

4.3 Graph Representation

The MIPS transition is markedly similar to the liquid-vapor transition seen in traditional thermodynamic fluids with the two coexisting phases both being disordered. In thermodynamic fluids one could measure local density and use spatial density discontinuities to distinguish between the coexisting phases. However, this is difficult to do in practice as we are constrained to finite systems in simulations. Regions close to the critical point are subject to large density fluctuations which make it difficult to observe persistent macroscopic phase domains. Therefore, we need an alternative way to gather this similar type of local structure in the system. We do this by representing the system as a graph.

For each simulation snapshot, we represent the system as a graph where each particle is a node in the graph and connections are made between first shell Voronoi neighbors. With periodic boundaries, this results in a fully-connected graph. If the edges are then constrained to be the distances between particles we obtain a three-dimensional, toroidal shape as depicted in Fig. 4.2(e)–(h).

In Fig. 4.2, we present simulation snapshots at different points of the phase diagram with their corresponding graph representations. Each particle and corresponding graph node are colored based on the Voronoi volume fraction of that particle. The graphs in each region of the phase diagram possess unique morphologies and characteristics. The gas phase [see Fig. 4.2(a),(e)] is marked by a uniform graph

with a rough surface. The disorder in the phase prevents a smooth surface from forming and any structure present is short-range. If we next look at a primarily dense system [Fig. 4.2(b),(f)], we see that the graph representation still has bumps on the surface, but they are not as sharp. The increased system density causes jamming and reduces the magnitude of fluctuations, which results in longer-range morphological features. When we approach the critical point [see Fig. 4.2(c),(g)], the graph starts to form "lumps" which are connected by coarse sections of the surface. This results from mixing regions with dense and dilute phase features. We can think of the connecting coarse regions as articulation points in the graph surface, which become less pronounced with lower activity. As we go deep into the coexistence region, the dense region is made up of a single large crystal providing clear spatial domains for the two phases, as shown in Fig. 4.2(d). The distinctive regions manifest as a coarse mesh for the dilute phase—similar to Fig. 4.2(e)—and a smooth surface for the dense phase with perturbations resulting from crystalline defects [see Fig. 4.2(h)].

The clear distinction in graph structure in the different phase regions lends support for the use of graph neural networks to aid in predicting particle phase. The use of local structure also serves to help make decisions for particles near phase interfaces and regions which may be marked by large density fluctuations.

4.4 Results

Here we present the results from our machine learning model. Our model was trained on very dilute ($\phi < 0.2$) or very dense ($\phi > 0.7$) phase points above the critical point and deep within the coexistence region. Training points from deep within the coexistence region were labeled by inspection and particles near phase interfaces were not used for training. The model was then used to predict particle phase below the critical point ($Pe_R^{crit} \sim 0.047$). Figure 4.3 presents the snapshots of particles shown in Fig. 4.2(a)–(d) colored by their predicted phase labels. It can be seen that our model is highly capable of distinguishing particle phase in the homogeneous phase and deep within the coexistence region. The most challenging region is near the critical point as these particles are more difficult to readily distinguish from inspection.

Therefore, to evaluate performance in this region we take the predicted particle labels for each phase point and compute the fraction of dilute particles F_g present and average this across all $T = 6$ time points for a given (Pe_R,ϕ) pair. This is represented by

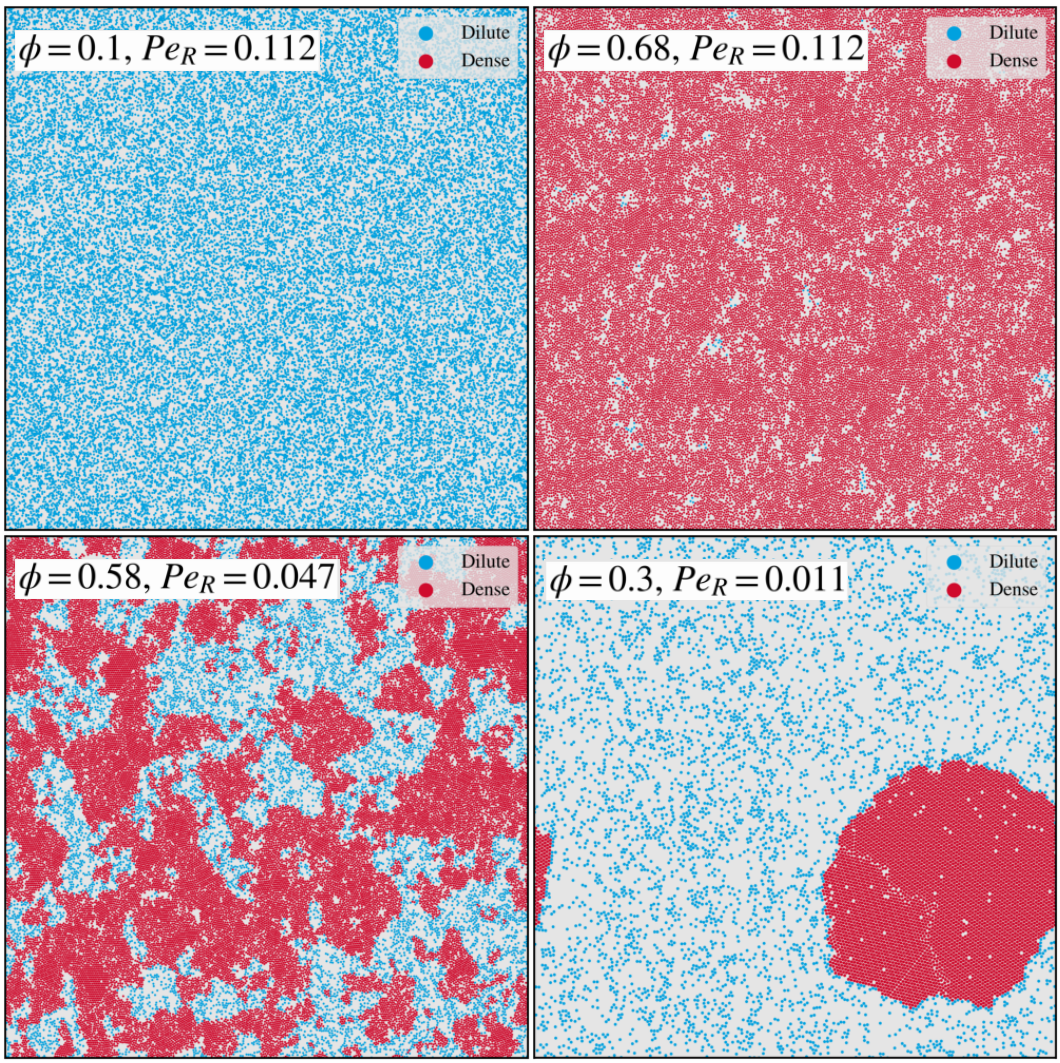

Figure 4.3: Simulation snapshots for different regions of the phase diagram with particles colored based on their predicted phase.

$$F_g = \frac{1}{T}\sum_{t=0}^{T}\left(1 - \frac{1}{N}\sum_{j}^{N} y_j(t)\right), \tag{4.4}$$

where y_j is the predicted label of particle j and N is the total number of particles. In our model the positive case is the dense phase ($y_j = 1$) and the null case is the dilute phase ($y_j = 0$). To account for small fluctuations in prediction we consider a point to be in the dilute region if F_g >95% and to be in the dense region if F_g <5%. Any other value of F_g is labeled as coexisting as we are only considering points below the critical point ($Pe_R^{crit} \sim 0.0468$).

Figure 4.4 presents the MIPS phase diagram with points colored based on which

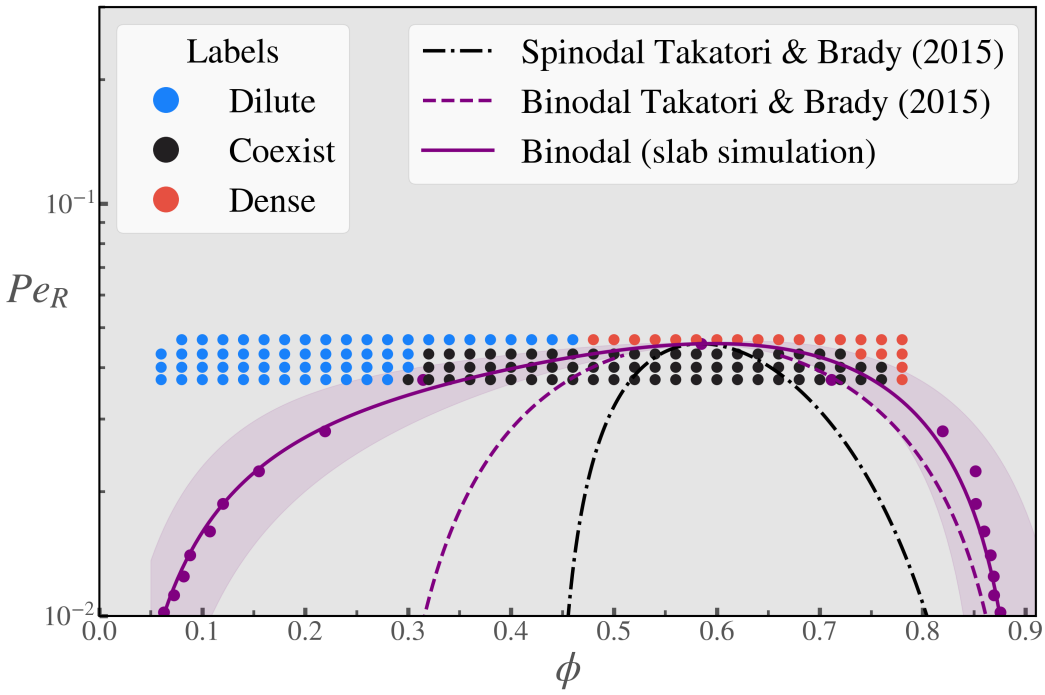

Figure 4.4: The Pe_R–ϕ phase diagram for purely active Brownian particles. We show the spinodal (black dash-dotted line) and binodal (purple dashed line) predicted by Takatori and Brady [2] along with the binodal computed from slab simulations (purple points). A fourth-order polynomial fit (solid purple line) is used to give a more complete picture of the computed binodal. The shaded region represents one standard deviation above and below the predicted fitting parameters. The remaining points on the graph are colored based on their predicted region of phase space from our machine learning model. We use a cutoff of >95% gas fraction to be considered gas (purple) and <1% gas fraction to be considered in the dense phase (blue). Every value for gas fraction between those values is considered within the coexistence envelope. Here we show Pe_R values in the range 0.0468–0.0374.

phase the system is predicted to be in using our machine learning model. We compare the predicted phase against the binodal predicted by Takatori and Brady [2] (purple dashed line) and the binodal computed from slab simulations (purple points). The solid purple line is a fourth-order polynomial fit of the computed binodal. The shaded region represents the range of this fit ±1 standard deviation for each fitting parameter. The spinodal predicted by Takatori and Brady (black dash-dotted line) is shown for completeness. We find remarkable agreement between the binodal obtained from simulations and our machine learning predictions.

From Fig. 4.4 it is clear that predicting dilute particles is more challenging than predicting dense particles. We suspect this difficulty arises from the large tail in the

distribution of Voronoi densities for particles in the dilute phase. Ha *et al.* observed this type of large overlap for particle density distributions when studying the phase behavior of a Lennard-Jones fluid [22].

4.5 Conclusions

We have created a machine learning model to predict the phase identity of individual active Brownian particles. Our results indicate that single-particle parameters are sufficient for learning particle phase when some amount of structure is included in the system. We have also shown that the MIPS phase transition can be predicted using this machine learning model. From our model optimization and feature analysis, we conclude that kinematic features—such as particle speed or the force-orientation correlation—are important for distinguishing the phases present in the MIPS transition (see appendix 4.6 and Fig. 4.6), unlike the traditional liquid-vapor transition present in thermodynamic fluids. The directed motion present in active systems results in a stronger separation for particle speeds and longer correlation lengths than would be seen in traditional systems when considering phase identity near the critical point. Ha *et al.* were able to successfully characterize particle phase of a Lennard-Jones fluid with high accuracy using a convolutional neural network and only three structural features [22], but we find that our model performance steeply drops off near the critical point if we do not include at least one of the kinematic features mentioned above.

We have demonstrated that the local structure plays an important role in determining the phase behavior of active systems. Our graph representations of the system possess unique characteristics specific to their region of the phase diagram—which can be learned using a general graph neural network framework with attention. This matches the results from Swanson *et al.* and Ha *et al.* who included structure via a message-passing network and convolutional neural network, respectively, to characterize amorphous materials [14, 22].

We believe machine learning can be used for more challenging classification problems. It would be straightforward to extend our framework to also distinguish between the hexatic crystalline phase and the disordered dense phase to produce a more complete phase diagram. Our model is already capable of learning the importance of the third shell average Voronoi volumes, which act as a surrogate for the third peak in the radial distribution function. This peak provides a way to distinguish between liquid and solid phases. We also feel a more specific model

could be created to directly predict which region of the phase diagram the system is in by performing classification at the graph-level instead of the node-level (as was done in this work). A graph-level classifier can then be readily generalized using an unsupervised learning scheme, where the model is learning distinctions between the present phases.

The learning architecture used here should also readily generalize to active systems with thermal noise, polydispersity, or higher dimensionality. These deviations from the problem focused on in this work would result in different distributions for feature values, but should still maintain similar relationships between features. The graph network can be further extended to include edge features, which would allow for more complicated or varied interparticle interactions and should prove to be a useful tool in the characterization of other amorphous systems.

Appendix

4.6 Feature Correlation and Importance

The correlation matrix for our full initial feature set is presented at the top of Fig. 4.5. In the figure we have used a shorthand notation where ϕ is the Voronoi volume fraction, ϕ_i is the Voronoi volume fraction averaged over the i^{th} shell neighbors, N_i is the number of neighbors in shell i, U is the particle speed, $\mathbf{F} \cdot \mathbf{q}$ is the force-orientation correlation, ψ_6 is the hexatic order parameter, and G_6 is the translational order parameter. The hexatic and translational order parameters are broken into their real part, imaginary part, magnitude, and angular components represented by $\mathfrak{R}(\cdot)$, $\mathfrak{I}(\cdot)$, $|\cdot|$, and $(\cdot)_{6,\theta}$, respectively. Features were dropped in order of the strength of the measured collinearity with other features. When considering a pair of collinear features, the feature that contributes the least to the total importance is removed.

We use a simple boosted random forest to compute feature importance. Our random forest classifier is made up of 1000 estimators, with a max decision tree depth of 8, and trained for 30 epochs with early stopping. Our boosted random forest is implemented in XGBoost. This classifier is then used to compute the SHAP feature importance (see Fig. 4.6) [29]. The color in Fig. 4.6 indicates the value of the feature in the line, and the actual SHAP value indicates how important a feature value was for predicting the positive (dense) case. As an example, from Fig. 4.6(top) we see that ϕ_3 is the most indicative feature, and large values of this feature strongly indicate that the particle is dense, whereas very low values indicate that the particle in question is likely dilute. The SHAP analysis for the full feature

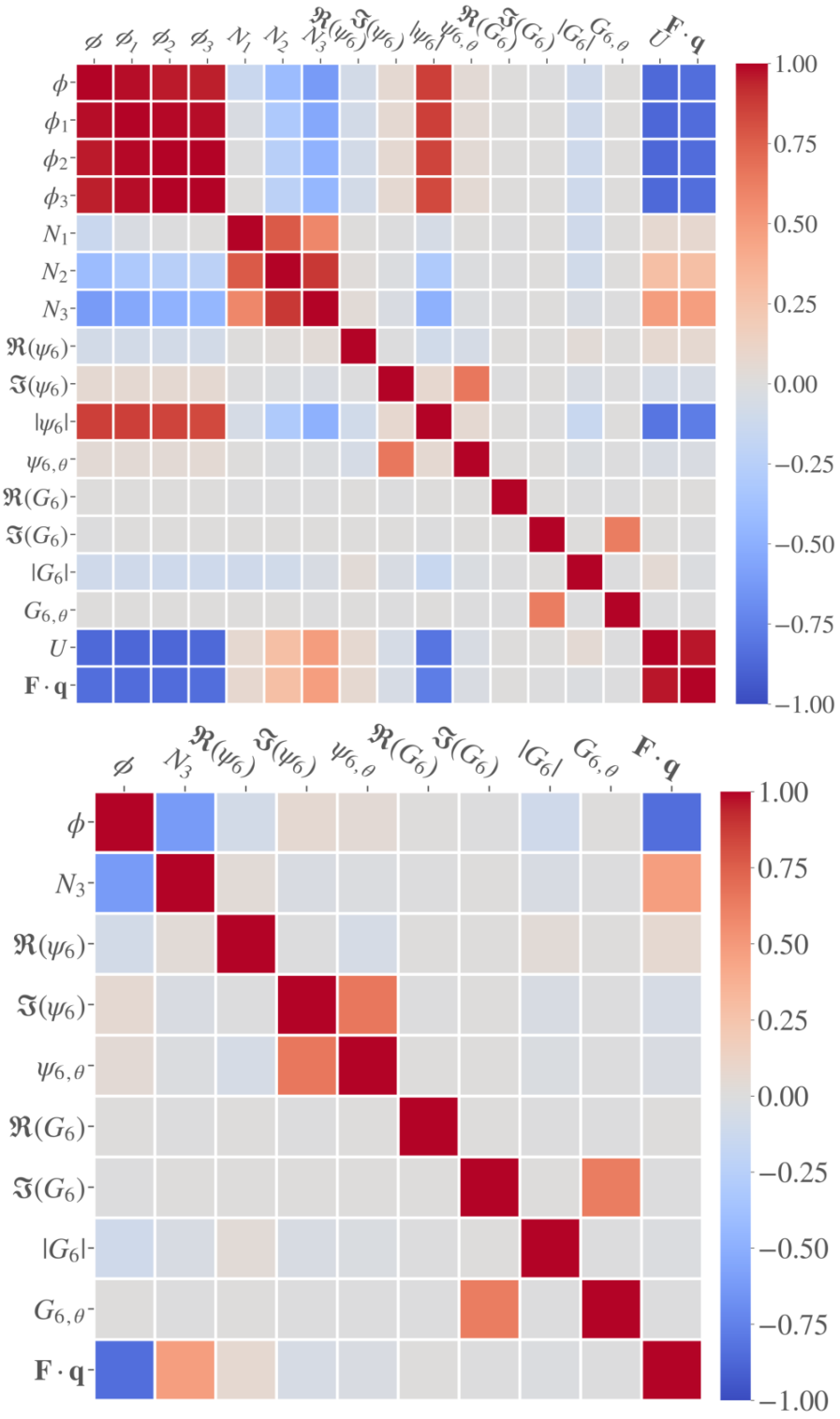

Figure 4.5: The correlation matrix for the (**top**) full and (**bottom**) reduced feature sets. Strong positively (red) and negatively (blue) correlated features are removed in the reduced feature set.

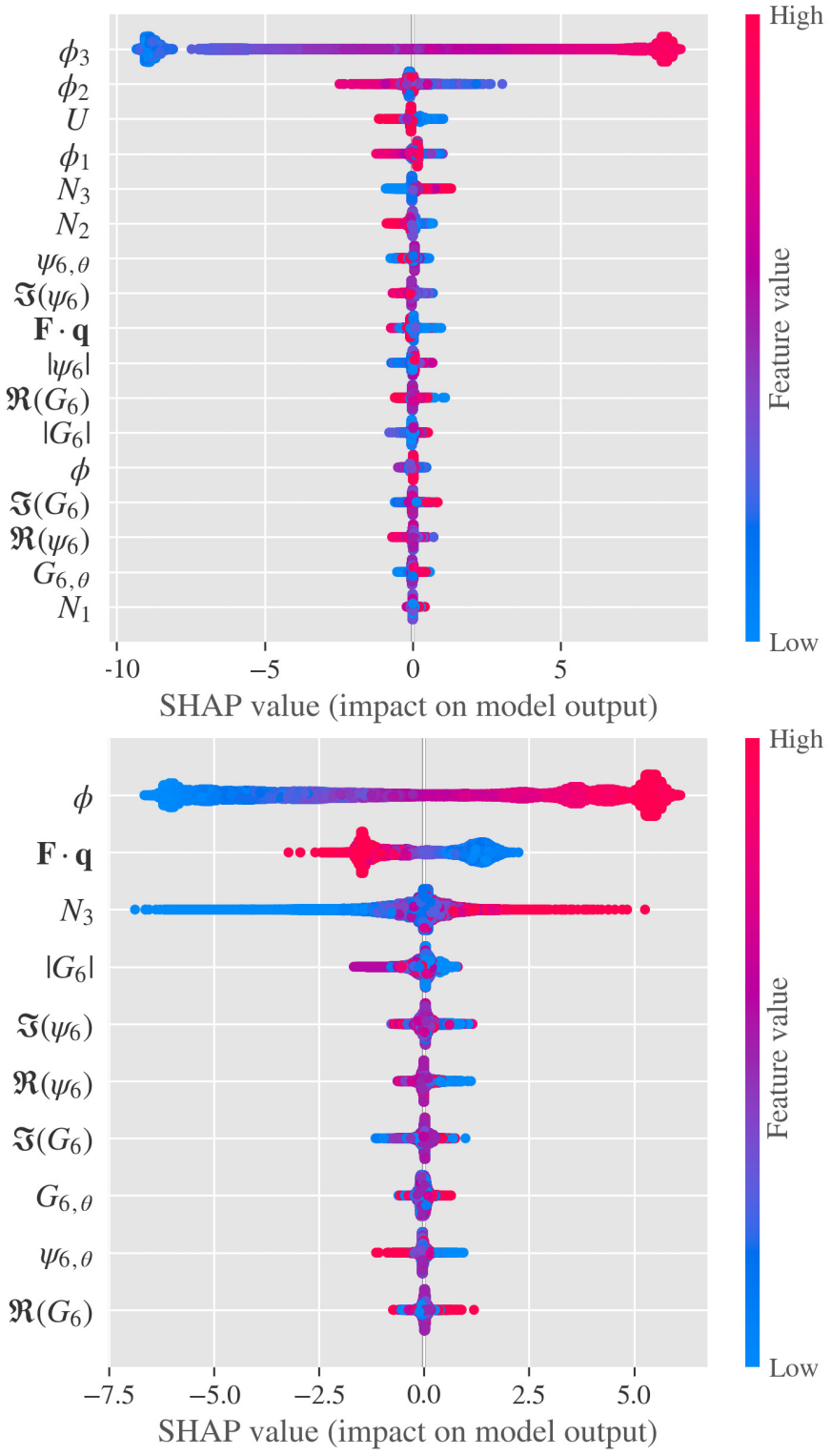

Figure 4.6: Feature importance for the (**top**) full and (**bottom**) reduced feature sets computed using SHAP. The color corresponds to the magnitude of a given feature. The SHAP value presents how important a feature is at predicting the positive class.

Table 4.1: The specific model architecture of the trained deep neural network used for the results presented in this work.

Layer	Size	Activation	Batch Norm	Dropout
1	128	ReLU	–	–
2	128	LeakyReLU[a]	True	0.69
3	128	LeakyReLU[a]	True	0.35
4	64	LeakyReLU[a]	–	0.75
5	2	SoftMax	–	–

[a]LeakyReLU activation function with negative slope $\alpha = 0.1$.

Table 4.2: The architecture of the graph network portion of our model.

Layer	Size	Activation	Attention Heads
1	8	LeakyReLU[a]	2
2	8	LeakyReLU[a]	2
3	8	LeakyReLU[a]	2
4[b]	2	SoftMax	–

[a]LeakyReLU activation function with negative slope $\alpha = 0.2$.

[b]This is a fully-connected layer used to get the final prediction.

set is not very insightful due to the presence of strong collinearity, but it can still be used to determine which feature to drop from a pair of highly collinear features. After removing a feature the importance is recalculated as this can change as the feature set changes. The final correlation matrix for the features used in this work is shown at the bottom of Fig. 4.5, and the final feature SHAP values are shown in the bottom of Fig. 4.6. There is greater diversity in the SHAP values obtained, and now the volume fraction as the most important feature, which is in line with our physical intuition.

4.7 Model and Training Details

The trained DNN used in this work is 5 layers with batch normalization and dropout on some of the layers for regularization. The number of layers in the network, size of each layer, batch normalization, and dropout values were determined from 1,500 rounds of hyperparameter optimization with the Hyperopt package [30]. The hyperparameter optimization was performed in three stages, each of which was 500 rounds. We first optimize the learning rate to speed up future training as much as possible. The optimal learning rate $lr = 3 \times 10^{-3}$ was used for the remaining optimization rounds with a batch size of 32. The next round of optimization focuses on the number of neurons in the network, the number of layers, and the activation

function used for the layer (between ReLU and LeakyReLU). The final optimization round is focused on regularization and tunes the batch normalization and dropout for each layer in the network. Our final chosen parameters are presented in Table 4.1.

The GNN model architecture used in this work was explored manually. The graph network is intentionally kept small as this was shown by Veličković *et al.* to be effective at transductive learning [25]. The parameters of our GNN are shown in Table 4.2. Each layer in the network is a GAT convolution layer except for the last one, which is a fully-connected layer to give the outputs.

References

[1] Y. Fily and M. C. Marchetti, "Athermal Phase Separation of Self-Propelled Particles with No Alignment", Physical Review Letters **108**, 235702 (2012).

[2] S. C. Takatori and J. F. Brady, "Towards a thermodynamics of active matter", en, Physical Review E **91**, 032117 (2015).

[3] D. Levis, J. Codina, and I. Pagonabarraga, "Active Brownian equation of state: metastability and phase coexistence", Soft Matter **13**, 8113–8119 (2017).

[4] J. U. Klamser, S. C. Kapfer, and W. Krauth, "Thermodynamic phases in two-dimensional active matter", Nature Communications **9** (2018).

[5] A. P. Solon, J. Stenhammar, M. E. Cates, Y. Kafri, and J. Tailleur, "Generalized thermodynamics of motility-induced phase separation: phase equilibria, Laplace pressure, and change of ensembles", New Journal of Physics **20**, 075001 (2018).

[6] S. C. Takatori, W. Yan, and J. F. Brady, "Swim Pressure: Stress Generation in Active Matter", en, Physical Review Letters **113**, 028103 (2014).

[7] S. Chakraborti, S. Mishra, and P. Pradhan, "Additivity, density fluctuations, and nonequilibrium thermodynamics for active Brownian particles", Physical Review E **93**, 052606 (2016).

[8] S. Paliwal, J. Rodenburg, R. Van Roij, and M. Dijkstra, "Chemical potential in active systems: Predicting phase equilibrium from bulk equations of state?", New Journal of Physics **20**, 015003 (2018).

[9] Y. Fily, Y. Kafri, A. P. Solon, J. Tailleur, and A. Turner, "Mechanical pressure and momentum conservation in dry active matter", Journal of Physics A: Mathematical and Theoretical **51** (2018).

[10] A. Patch, D. M. Sussman, D. Yllanes, and M. C. Marchetti, "Curvature-dependent tension and tangential flows at the interface of motility-induced phases", Soft Matter **14**, 7435–7445 (2018).

[11] J. Carrasquilla and R. G. Melko, "Machine learning phases of matter", Nature Physics **13**, 431–434 (2017).

[12] E. P. L. van Nieuwenburg, Y.-H. Liu, and S. D. Huber, "Learning phase transitions by confusion", Nature Physics **13**, 435–439 (2017).

[13] P. Suchsland and S. Wessel, "Parameter diagnostics of phases and phase transition learning by neural networks", Physical Review B **97**, 174435 (2018).

[14] K. Swanson, S. Trivedi, J. Lequieu, K. Swanson, and R. Kondor, "Deep learning for automated classification and characterization of amorphous materials", Soft Matter **16**, 435–446 (2020).

[15] S. A. Mallory, C. Valeriani, and A. Cacciuto, "An Active Approach to Colloidal Self-Assembly", Annual Review of Physical Chemistry **69**, 59–79 (2018).

[16] J. Palacci, S. Sacanna, A. P. Steinberg, D. J. Pine, and P. M. Chaikin, "Living Crystals of Light-Activated Colloidal Surfers", en, Science **339**, 936–940 (2013).

[17] C. Bechinger, R. Di Leonardo, H. Löwen, C. Reichhardt, G. Volpe, and G. Volpe, "Active Particles in Complex and Crowded Environments", Reviews of Modern Physics **88**, 045006 (2016).

[18] W. Gao and J. Wang, "The Environmental Impact of Micro/Nanomachines: A Review", ACS Nano **8**, 3170–3180 (2014).

[19] S. Ebbens, "Active colloids: Progress and challenges towards realising autonomous applications", Current Opinion in Colloid & Interface Science **21**, 14–23 (2016).

[20] J. A. Anderson, C. D. Lorenz, and A. Travesset, "General purpose molecular dynamics simulations fully implemented on graphics processing units", Journal of Computational Physics **227**, 5342–5359 (2008).

[21] J. Glaser, T. D. Nguyen, J. A. Anderson, P. Lui, F. Spiga, J. A. Millan, D. C. Morse, and S. C. Glotzer, "Strong scaling of general-purpose molecular dynamics simulations on GPUs", Computer Physics Communications **192**, 97–107 (2015).

[22] M. Y. Ha, T. J. Yoon, T. Tlusty, Y. Jho, and W. B. Lee, "Widom Delta of Supercritical Gas-Liquid Coexistence", Journal of Physical Chemistry Letters **9**, 1734–1738 (2018).

[23] D. P. Kingma and J. L. Ba, "Adam: A method for stochastic optimization", in 3rd international conference on learning representations, iclr 2015 - conference track proceedings (Dec. 2015).

[24] T. N. Kipf and M. Welling, "Semi-Supervised Classification with Graph Convolutional Networks", (2016).

[25] P. Veličković, A. Casanova, P. Liò, G. Cucurull, A. Romero, and Y. Bengio, "Graph attention networks", in 6th international conference on learning representations, iclr 2018 - conference track proceedings (Oct. 2018).

[26] Z. Wu, S. Pan, F. Chen, G. Long, C. Zhang, and P. S. Yu, "A Comprehensive Survey on Graph Neural Networks", (2019).

[27] M. Wang, D. Zheng, Z. Ye, Q. Gan, M. Li, X. Song, J. Zhou, C. Ma, L. Yu, Y. Gai, T. Xiao, T. He, G. Karypis, J. Li, and Z. Zhang, "Deep Graph Library: A Graph-Centric, Highly-Performant Package for Graph Neural Networks", (2019).

[28] V. Ramasubramani, B. D. Dice, E. S. Harper, M. P. Spellings, J. A. Anderson, and S. C. Glotzer, "freud: A Software Suite for High Throughput Analysis of Particle Simulation Data", Computer Physics Communications **254** (2019).

[29] S. M. Lundberg, P. G. Allen, and S.-I. Lee, *A Unified Approach to Interpreting Model Predictions*, tech. rep. (2017), pp. 4765–4774.

[30] J. Bergstra, D. Yamins, and D. D. Cox, *Making a Science of Model Search: Hyperparameter Optimization in Hundreds of Dimensions for Vision Architectures*, tech. rep. (2013).

Chapter 5

CHARACTERIZING SUPERCRITICAL ACTIVE FLUIDS

Using a combination of large-scale simulation, analytic theory, and machine learning, we characterize the supercritical behavior of a suspension of repulsive active Brownian particles (ABPs). We use our previous work on the compressibility of active matter to compute the Widom line in the supercritical region of the active phase diagram. The identification of the Widom line provides insight into the relative character of each phase (liquid or gas) present at each point in the phase diagram in the supercritical regime. We use a machine learning classifier to identify gas-like and liquid-like coexisting particles in the supercritical region, and from this, we determine the location of the Widom line based on an equal fraction of each phase.

5.1 Introduction

Active matter systems truly challenge our theoretical understanding of nonequilibrium phenomena and simultaneously represent a potentially innovative approach to directed transport and material design at the microscale. In contrast to traditional nonequilibrium systems, where directional driving forces emerge as a result of global changes in thermodynamic variables or boundary conditions, active systems are intrinsically out of equilibrium at the single-particle level. The inherent nonequilibrium nature of these systems and their complex collective behavior have inspired a large body of work in the area of nonequilibrium statistical mechanics and soft condensed matter.

Particular focus has been placed on understanding the seemingly paradoxical phenomenon of motility induced phase separation (MIPS), where a suspension of purely-repulsive active particles exhibits behavior that is analogous in many ways to liquid-vapor phase coexistence in equilibrium systems [1–7]. While a balance between attractive and repulsive intermolecular forces is required to observe liquid-vapor coexistence in classical fluids at equilibrium, the same is not true for MIPS—which occurs with no attractive forces present. This startling discovery has resulted in a vast majority of research on the subject focusing on coexistence and the two-phase region (below the critical point), giving rise to multiple phase diagrams in both two and three dimensions.

There has been significantly less work on the behavior of ABPs in the supercritical region (i.e. above the critical point where there is no liquid-vapor phase separation) [8]. Most studies in this region have been centralized around the critical point to determine the universality class of ABPs [7, 8] or more recently, to study response functions in active suspensions [9]. There has yet to be substantial research into supercritical active fluids.

Traditional supercritical fluids (SCFs) have been used in a wide range of applications such as food extraction, pharmaceutical development, and environmental pollution measurements [10–12]. The key feature that has made SCFs such a useful tool for separation and extraction processes is the ability to continuously tune their properties while in a homogeneous state. Supercritical fluids have gas-like and liquid-like properties that dominate different parts of the SCF regime [10–13] and allow for selective and tunable separation processes based on the state of the fluid.

The variation in the parameters of a SCF can be viewed as the fluid becoming more gas-like or more liquid-like depending on the state variables. The desire to

distinguish between the regions of the supercritical phase led to the development of the Widom line [14]. The Widom line is denoted as the line of maximum correlation length or the local maxima of thermodynamic response functions [14]. These traits are reminiscent of the divergent behavior at the vapor-liquid coexistence line, which allows one to consider the Widom line as an extension of the coexistence line into the supercritical phase. It was shown by Ha et al. [15] that the Widom line can be described by the line of points where the phase fraction of liquid-like and gas-like particles are equivalent thanks to an argument minimizing the free energy of the system while maximizing the density fluctuations. This provides a method through which the supercritical phase can be divided to give yield predominantly gas-like or liquid-like behavior.

Our recent work showing that the "isothermal" compressibility behaves like a thermodynamic response function in suspensions of active Brownian disks creates an excellent starting point through which we can explore the Widom line in these systems [9]. Through a combination of large-scale simulation and our recent machine learning model [16], which classifies active particles based on the phase they belong to, we are also able to test whether the results obtained by Ha et al. [15] hold for active systems by extending our model to classify particles in the supercritical region.

This chapter is organized as follows. In section 5.2, we define our implementation of the active Brownian particle model and discuss all relevant details to performing large-scale simulations. In section 5.3, we discuss the phase phenomenology for active Brownian systems in the supercritical region. Additionally, we identify several active Widom line. In section 5.4, we introduce a machine learning model to predict particle phase behavior in the supercritical region. In section 5.5, we provide an argument for computing the Widom line from the equivalence of phase fraction in the supercritical region. We also compute the Widom line using phase fraction, predicted from our machine learning model. Lastly, we summarize our work and draw comparisons between active and passive systems in section 5.6.

5.2 Simulation Framework

We simulate a suspension of monodisperse, athermal active particles of radii a. The active motion is described by an intrinsic swim velocity $U_0\mathbf{q}$—where $\mathbf{q}$ is the particle orientation—and a reorientation timescale τ_R. The system is evolved forward in time using overdamped Langevin dynamics

$$0 = -\zeta \mathbf{U}_i + \mathbf{F}_i^{swim} + \sum_{i \neq j} \mathbf{F}_{ij}^P, \tag{5.1}$$

$$0 = \zeta_R \mathbf{\Omega}_i + \mathbf{L}_i^R, \tag{5.2}$$

where $\mathbf{U}_i$ is the translational velocity of particle i, $\mathbf{\Omega}_i$ is the angular velocity, $\mathbf{F}_i^{swim} = \zeta U_0 \mathbf{q}_i$ is the force from swimming, and ζ and ζ_R are the translational and rotational drags, respectively. The particle orientation evolves in time via $\partial \mathbf{q}_i / \partial t = \mathbf{\Omega}_i \times \mathbf{q}_i$. Reorientations occur through a stochastic torque $\mathbf{L}_i^R$ governed by white noise statistics with zero mean and variance $2\zeta_R^2 \delta(t)/\tau_R$. Normalizing the length and timescale by $\ell = U_0 \tau_R$—the distance travelled between reorientation events—and τ_R.

5.3 Active Widom Lines

Supercritical fluids can be thought of as heterogeneous mixtures of microphases, each of which is present in the nearby two-phase coexistence region [17]. The Widom line is defined as the maximum of a thermodynamic response function: isobaric heat capacity, isothermal compressibility, and thermal expansivity to name a few [17–21]. While there is a heat capacity prediction for active particles [22], we focus on and compute the Widom line via "isothermal" compressibility χ_τ [9]. The compressibility can be defined in terms of the active pressure $\Pi^{act} = \Pi^{coll} + \Pi^{swim}$ as

$$\chi_\tau = \frac{1}{n} \Big(\frac{\partial n}{\partial \Pi^{act}} \Big)_{N, Pe_R}, \tag{5.3}$$

where Π^{swim} is the pressure that results from the activity [23], Π^{coll} is the collisional pressure, n is the number density, and N is the total number of particles. The compressibility can also be defined from the static structure factor $S(\mathbf{k})$ via the active compressibility equation

$$\chi_\tau = \frac{1}{n k_s T_s} S(|\mathbf{k}| \to 0), \tag{5.4}$$

where $k_s T_s = \zeta U_0^2 \tau_R / 2$ is the activity [23] and $\mathbf{k}$ is the wavenumber. The Widom line can then be calculated by the maximum of χ_τ using either definition. Since the Widom line was originally defined as the maximum correlation length, we can

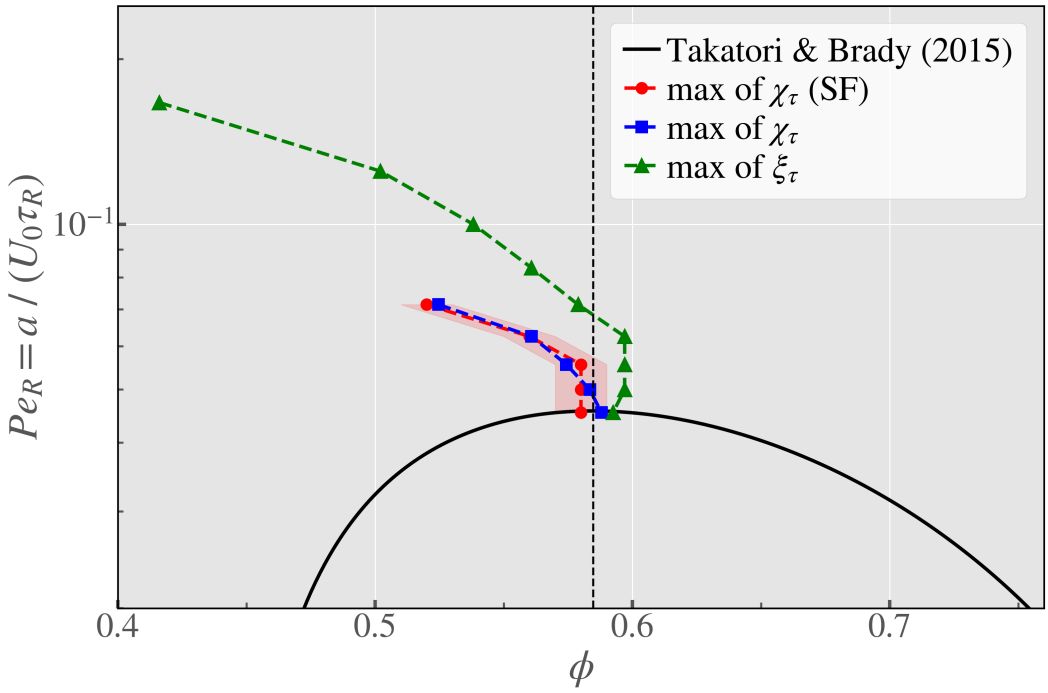

Figure 5.1: The maximum density fluctuation and compressibility Widom lines for ABPs on the $Pe_R - \phi$ plane. The beginning of each Widom line is close to the critical point predicted by Takatori and Brady [1].

compute it in this way by expanding the static structure factor in the limit of small wavenumber

$$S(|\mathbf{k}| \to 0) = \frac{S(0)}{1 + \xi_{OZ}^2 k^2}, \tag{5.5}$$

where ξ_{OZ} is the well-known Ornstein-Zernike correlation length [6, 24]. By computing the static structure factor at different points in the phase diagram, we can use the expansion in the low wavenumber limit to compute ξ_{OZ} from a regression, as was done in [9]. The Widom line, along with the spinodal predicted by Takatori and Brady [22], is presented in Fig. 5.1.

Figure 5.1 depicts the Widom line as computed from maximizing χ_τ (defined using Eqs. (5.3) and 5.4) and maximizing the density fluctuations $\xi_\tau = (\partial n/\partial \Pi^{act})_{N,Pe_R}$ along with the spinodal predicted by Takatori and Brady [1]. Each Widom line is computed for discrete (Pe_R, ϕ) pairs with dashed lines to draw the eye. There is excellent agreement in the Widom line computed mechanically (blue squares) and from the static structure factor (red circles), as expected from the equivalence of

the two definitions for compressibility. The error (red shaded region) on the data obtained using the active compressibility equation results from the discrete values used in our simulation data. The maximum density fluctuations (green triangles) deviate from the maximum compressibility due to the additional factor of n^{-1}. Here we see that each of the lines truncate at the critical packing fraction $\phi^{crit} \sim 0.58$ [1]), given by the black dashed line. Early truncation of the Widom lines resulting from compressibility is due to the divergence of χ_τ as $\phi \to 0$ from the leading factor of n^{-1}. As such, we have neglected to compute the Widom line for values of Pe_R which result in a maximum near $\phi = 0$, a practice which is not uncommon for certain definitions of the Widom line [18].

The Widom line may also be computed using the maximum correlation length. From Eq. (5.5), we obtain the Ornstein-Zernike correlation length, and the resulting Widom line lies directly on the compressibility line computed using structure factor. Thus, we have abstained from presenting this in Fig. 5.1.

5.4 Machine Learning Framework

Since the supercritical phase can be viewed as a heterogeneous mixture of gas-like and liquid-like particles, it is impossible to ascertain the identity of the local states through standard order parameters. We circumnavigate this difficulty through the use of machine learning (ML). In our previous work [16] we were able to classify the state of particles below the critical point—in the coexistence region—and consequently recreate the MIPS binodal. Here we can rely on a similar strategy, but now we will focus on predicting the local state of individual particles in the supercritical region.

We are solving a binary classification problem using a combination of supervised and semi-supervised ML frameworks. Our model is structured in two steps: the first being a supervised deep neural network (DNN) and the second being a semi-supervised graph neural network (GNN). The DNN takes particle features and makes an initial prediction on the state of each particle given as a probability of the particle being in the dense phase (positive case). The label probability is then one-hot-encoded and compared against the true labels designated for each particle. Our focus is on predicting in the supercritical region, which allows us to use the homogeneous dense and dilute phases below the critical point for training data.

Once the DNN model is trained, we then predict on points of the phase diagram in the supercritical region. From the initial prediction, we take the most confident

labels—those with >90% probability of predicting a given phase—and use them as the label. Next, we convert the simulation snapshot from which the feature data was taken into a graph form (as was done in [16]). The confident labels from the DNN, the graph, and the feature data are then used as inputs for the semi-supervised GNN. The GNN uses a particle's labeled neighbors to influence its predicted state. Once a label is obtained, the probabilities for the label from each model are averaged together to yield the final label prediction. The GNN step is important for making final decisions because the distribution of features for each phase are expected to be more similar in the supercritical region. We can formulate the problem in this way because GNNs have a history of performing well on semi-supervised node labeling problems like we have here [25–27]. Our GNN layers are based on the graph attention network (GAT), which quantifies the importance of neighboring nodes through self-attention [28]. For both models, our loss function is taken to be binary cross-entropy (shown in Eq. (3) of [16]).

Particle Features

Particle features considered are presented in Table 5.1 The set of features chosen include the Voronoi volume fraction computed from a Voronoi tessellation $\phi^{voro} = \pi a^2 / v^{voro}$, the number of neighbors in the k^{th} Voronoi shell, and the average volume fraction of particles in the k^{th} Voronoi shell, where v^{voro} is the Voronoi volume of the particle of interest and $k = 1, 2, 3$. We also utilize the hexatic and translational order parameters, ψ_6 and $G_6(\mathbf{r}_{ij})$ respectively, as a metric for structure in the system. Both order parameters are split into their real $\Re(\cdot)$ and imaginary $\Im(\cdot)$ parts, angular component $(\cdot)_\theta$, and absolute value $|\cdot|$, turning each into four distinct features. The order parameters and Voronoi analysis were carried out using the Freud software package [29]. Additionally, we consider the particle speed U and the correlation between the force acting on a particle and it's orientation $\mathbf{F}_i \cdot \mathbf{q}_i$. Each feature, along with its description and formula are presented in Table 5.1.[1]

The initial set of features has been paired down using a boosted random forest and feature importance analysis with XGBoost. We first rank features by importance and remove highly collinear features of low importance. After a feature is removed the importance is calculated again and the process is repeated until the most collinear features have been removed while maintaining those which are highly important.

[1]The order parameters are left as one feature each as dividing them into their components is straightforward and requires no conceptual leaps.

Table 5.1: The list of per particle features used to predict the local state of active particles in the supercritical region.

Feature	Description	Formula
ϕ^{voro}	Voronoi volume fraction.	$\phi^{voro} = \frac{a^2\pi}{v^{voro}}$
N_k	Number of neighbors in k^{th} Voronoi shell.[a]	–
ϕ_k^{voro}	Voronoi volume fraction averaged over k^{th} shell Voronoi neighbors.	$\phi_k^{voro} = \sum_j^{N_k} \phi_j^{voro}$
$\mathbf{F}_i \cdot \mathbf{q}_i$	Force-orientation correlation of particle i.	–
U_i	Speed of particle i with drag coefficient ζ.	$U_i = \frac{1}{\zeta}\lvert\mathbf{F}_i\rvert$
ψ_6	The hexatic order parameter of particle i.[b]	$\psi_6 = \frac{1}{N}\sum_j^N e^{\mathrm{i}6\theta_{ij}}$
$G_6(\mathbf{r}_{ij})$	The translational order parameter computed for particle i and Voronoi neighbors j.[c]	$G_6(\mathbf{r}_{ij}) = \sum_j^N \psi_6(i)\psi_6^*(j)$

[a] $k \leq 3$.
[b] θ_{ij} is the angle between the vector connecting particle i and neighbor j and reference angle $(0, 1)$.
[c] $\mathbf{r}_{ij}$ is the vector connecting particle pair i, j.

Training Data

The training data was obtained from simulations below the critical point either in the coexistence region or within either single homogeneous phase. If a (Pe_R, ϕ) pair lay outside the binodal (see Fig. 5.2), then every particle in the corresponding simulation was labeled according to the phase predicted from the phase diagram. For phase points inside the binodal, we used an image labeling procedure to find boundaries of the given dense and dilute regions, taking special care to stay far away from interfaces or ambiguous data. This was used to balance the number of dense particles used for training as the dense branch of the binodal is close to close-packing ($\phi_{cp} \sim 0.91$). Our image labeling procedure is outlined in appendix 5.7.

5.5 Machine-Learned Widom Line

Now that we have a model to predict the local state of particles in the supercritical region, we can investigate the Widom line from the perspective of phase fraction.

Ha *et al.* [17] show that the Widom line exists at the point of equal phase fraction using a free energy argument, based on the free energy of mixing. We can attempt to do a similar thing here for active systems. If we take the free energy of mixing to be

$$G^{act} = \phi_g G_g^{act} + \phi_l G_l^{act} - T_s \Delta_{mix} S^{act}, \tag{5.6}$$

where G^{act} is the active, nonequilibrium Gibbs free energy of the mixture, G_g^{act} is the Gibbs free energy of the gas, G_l^{act} is the free energy of the liquid, $\Delta_{mix} S^{act}$ is the entropy of mixing, ϕ_g is the fraction of gas-like particles, ϕ_l is the fraction of liquid-like particles, and T_s has been factored out of the activity to make something analogous to a temperature (we will see that splitting the activity in this manner is not essential at the end of our analysis). Using the definition of entropy from information theory gives an entropy of mixing in terms of the two phase fractions, like in traditional thermodynamics. This allows us to write the mixing entropy as $\Delta_{mix} S^{act} = k_s \sum_i \phi_i \ln \phi_i$, where $i = g, l$ represents a phase in the mixture. If we minimize G^{act}—as should be the case for coexistence—then we can get an expression for the difference between the free energies of each phase $\Delta G = (G_g^{act} - G_l^{act})/k_s T_s$ in terms of the gas fraction

$$\Delta G = 1 + 2\phi_g + \ln\left(\frac{1-\phi_g}{\phi_g}\right). \tag{5.7}$$

Since the Widom line can be thought of as an extension of coexistence, we can now attempt to minimize ΔG, which gives the criterion for the Widom line as $\phi_g = 1/2$, just like what was shown for passive Lennard-Jones fluids [17].

Now that we have a phase fraction criterion we can attempt to predict where the Widom line is located using our ML model. For each (Pe_R, ϕ) pair, we predict the phase of each particle in a simulation snapshot and compute the fraction of each phase. This process is repeated for multiple time points (separated by at least $1000\tau_R$). The predictions at the time points are then averaged—to minimize the impacts of noise and instantaneous fluctuations—yielding a prediction of the phase fraction at that particular phase-point.

Figure 5.2 presents our initial machine-learned Widom line (black circles) compared to the Widom lines computed from our response functions (similar to Fig. 5.1). When setting the phase fraction equal we see that the Widom line computed from

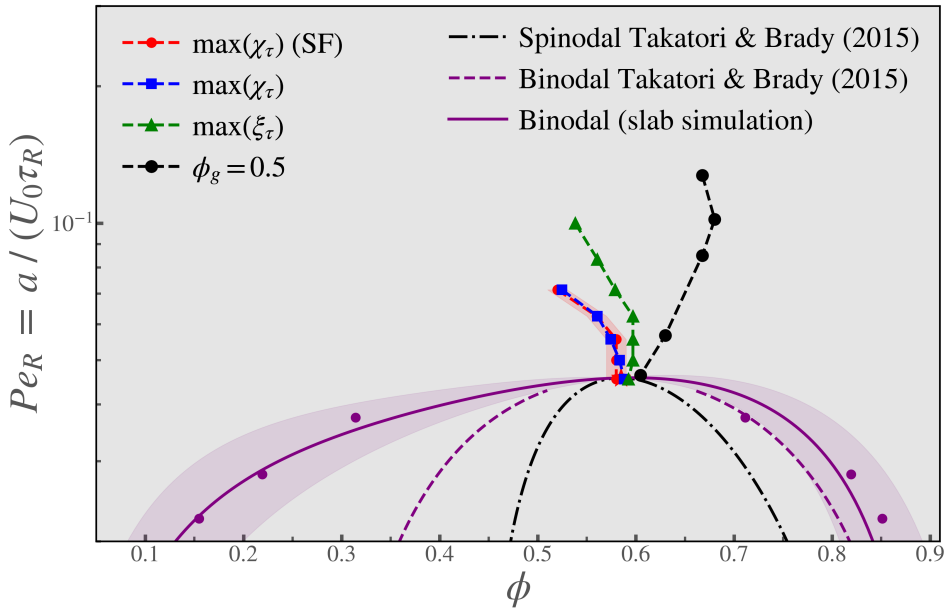

Figure 5.2: The Widom line computed from the equal phase fraction of gas-like $\phi_g = 0.5$ to liquid-like particles (black circles) compared to the Widom line computed from maximum in the compressibility (red circle and blue square) and density fluctuations (green triangle). The spinodal (black dash dotted line) and binodal (purple dashed) from Takatori and Brady [1] is shown along with the binodal computed from slab simulations (purple solid line).

phase fraction retains the same curvature as the line computed from the maximum of compressibility but is shifted towards higher system densities. We notice that the maximum compressibility line stays to the left of the critical isochore ($\phi^{crit} \sim 0.58$), whereas the equal phase fraction and density fluctuation (ξ_τ) lines curve to the right of this critical isochore (an increase in density) before eventually curving back towards lower densities as activity decreases. Ha *et al.* showed that the equal phase fraction criterion matches with the local maximum of the specific heat in Lennard-Jones fluids [15], which also shows an increase in density as you move away from the critical point before eventually decreasing back towards the critical isochore again [18]. The curvature of the maximum χ_τ lines behaves qualitatively similar to those of Lennard-Jones [18] and van der Waals [18, 19] fluids on the temperature–density plane. Similarly to equilibrium fluids, the active Widom lines converge near the critical point but rapidly diverge as activity increases.

5.6 Conclusions and Future Works

We have computed the Widom line in supercritical suspensions of ABPs using the local maximum of compressibility and equal phase fraction of gas and liquid-like particles motivated by a free energy of mixing argument. The Widom line shows a decrease in density as activity increases, when computed from the maximum of compressibility χ_τ, just like in Lennard-Jones fluids as temperature increases. If the supercritical phase is treated as a heterogeneous mixture of gas-like and liquid-like particles, then one can create an additional criterion for the Widom line given by when the fraction of each are equal. This balance of phase fraction is derived by minimizing the free energy of mixing and subsequently minimizing the difference in the free energy of each pure phase [15]. This serves as a proxy for maximizing the density fluctuations in the system and is found to occur when the gas phase fraction $\phi_g = 0.5$.

To compute the phase fraction of the system, we have developed a machine learning model which predicts the local state of each particle in the suspension based on single-particle properties and local structure (similar to the procedure outlined in [16]). From the predicted phase fractions, we predicted the Widom line based on the aforementioned criteria. Our equal phase fraction Widom line shows an increase in density as activity increases, followed by a decrease back towards the critical isochore. Similar nonmonotonic behavior as a function of activity is seen in the Widom line computed from the density fluctuations. This behavior shows good qualitative agreement with the behavior observed in Lennard-Jones and van der Waals fluids.

The Widom line may be defined using the local maximum of the correlation length [24]. From this perspective, one could use the Ornstein-Zernike correlation length, similarly to Brazhkin et al. [19], but this is not the true correlation length in the system [24]. The true correlation length is found from the decay of the total correlation function $h(\mathbf{r}) = g(\mathbf{r}) - 1$. We were unable to confidently compute the correlation length in this fashion as $g(r)$ did not fully decay in our simulations due to finite-size effects. Long-range fluctuations become increasingly prominent when activity increases, necessitating larger simulation boxes to allow the radial distribution function to fully decay. As such a more in-depth study on the decay of $h(\mathbf{r})$ is required to compute the true correlation length and any resulting Widom line for a supercritical active suspension.

Additionally, we suggest exploring the use of other response functions in active

systems. We began with compressibility since it can be well defined and it behaves like a thermodynamic response function [9]. Other traditional response functions may have active analogues as well. Others have theorized the form of the heat capacity of ABPs [1], but to our knowledge, there have been no further explorations into these response functions.

Appendix

5.7 Labeling Difficult Data

We developed a pipeline for autonomously labeling dense particles using image analysis to generate training labels for particles inside the coexistence envelope. The procedure for analysis is as follows. First, we load the simulation trajectory. We then render and save an image of the trajectory at the instance in time of interest, with particles colored based on their Voronoi density (see Fig. 5.3). The scale for the color at this stage is not important as the maximum and minimum values are set based on the individual snapshot to provide the highest pixel contrast. Image rendering and Voronoi calculations were performed using the Ovito visualization tool [30].

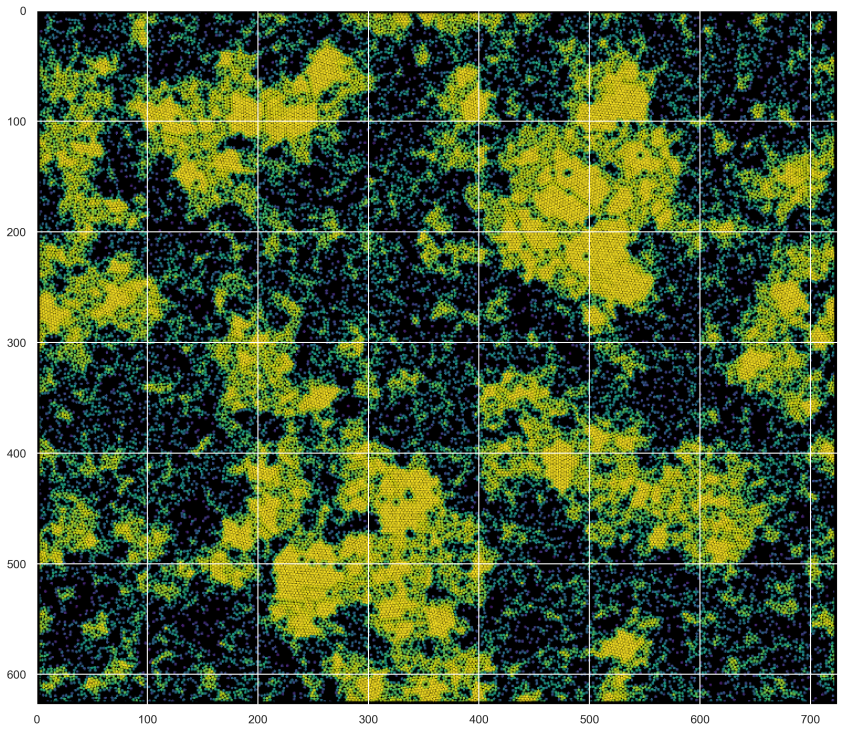

Figure 5.3: A snapshot of a Brownian dynamic simulation, within the coexistence region, colored by Voronoi density.

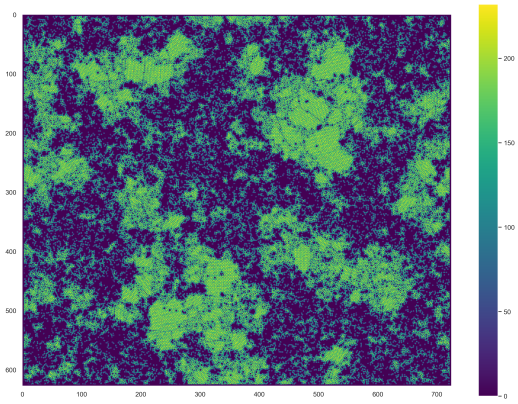

Figure 5.4: The BD simulation snapshot from Fig. 5.3 with color converted to a scale from 0–256.

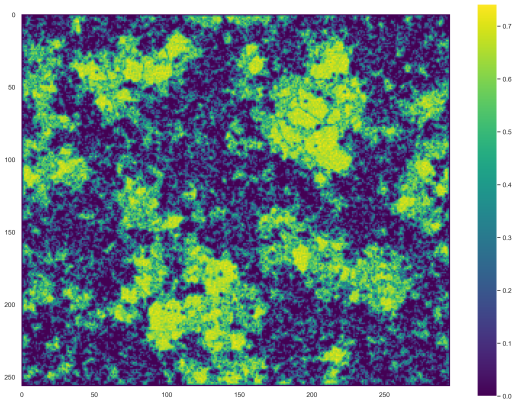

Figure 5.5: Figure 5.4 rescaled such that simulation box size can be mapped 1:1 to the image size in pixels and color is normalized from 0 to 1.

Next, the image pixel values are converted from RGBA to RGB, then to grayscale to give a single channel value for the pixel color (see Fig. 5.4). The simulation trajectory is then scaled such that the simulation box size matches with the pixel size of the image. This creates a 1:1 mapping from particle positions to pixel locations. Figure 5.5 illustrates the scaling of Fig. 5.4, with the single-channel pixel values normalized to be from 0 to 1.

Once the image has been rescaled we apply a 3×3 median-value filter to the image. The filter takes the median value for pixels in a 3 by 3 box and applies that value to each pixel in that box. The filter is then shifted over and the process is repeated until the entire image has been masked. This filtering step coarsens the color values slightly, removing fluctuations and dead pixel zones (see Fig. 5.6). After filtering, we make a histogram for the pixel values to make thresholds based on high and low-intensity regions. Figure 5.7 depicts the histogram for Fig. 5.6, with lower threshold (green line) and upper threshold (red line). These thresholds are picked such that they are outside local maximums on the histogram. These local maxima can be thought to represent the phases in the system, with the two maxima on the right side of the upper threshold representing the disordered dense and crystalline populations, respectively. The lower threshold is determined by forcing a minimum value difference between it and the upper threshold. This helps ensure that the lower threshold does not contain any portion of the dense population.

We perform contour tracing using the determined thresholds to capture high-intensity and low-intensity regions of the image (see Fig. 5.8). The contours encap-

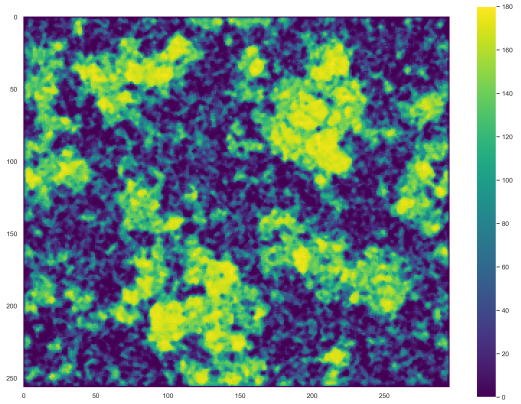

Figure 5.6: Figure 5.5 after applying a 3×3 filter median value filter.

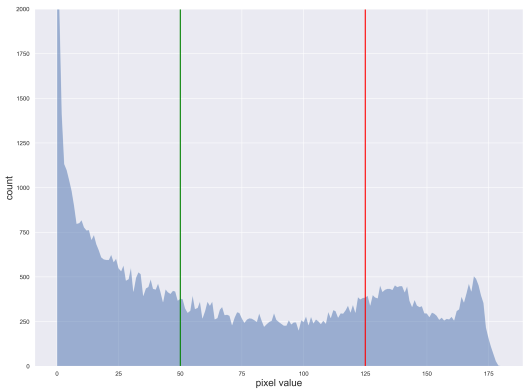

Figure 5.7: Histogram of pixel intensity of Fig. 5.6 with low (green line) and high (red line) pixel intensity thresholds.

sulate regions of a specific pixel intensity that have a minimum pixel count (roughly 50 for low intensity and 120 for high-intensity regions). This prevents contours from being placed around small regions in the image that may be rather ambiguous. Particles are then labeled based on which contour encapsulates them. Labeled particles are shown overtop the grayscale, filtered image in Fig. 5.9. The visible regions of gray are those which we neglect thanks to our separation of threshold values. By

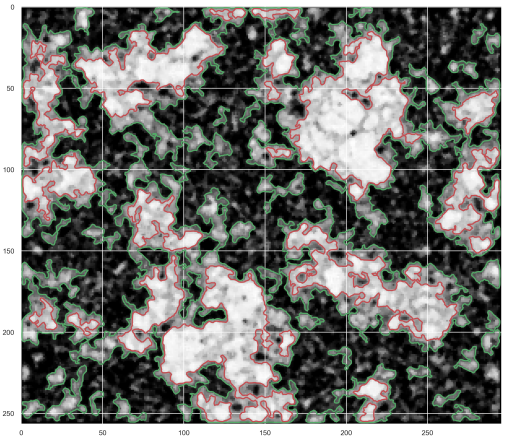

Figure 5.8: Contours based on pixel intensity cutoffs in Fig. 5.7, with red and green contours surrounding high and low intensity regions, respectively. Only contours that contain more than 50 (low intensity) or 125 (high intensity) pixels are shown.

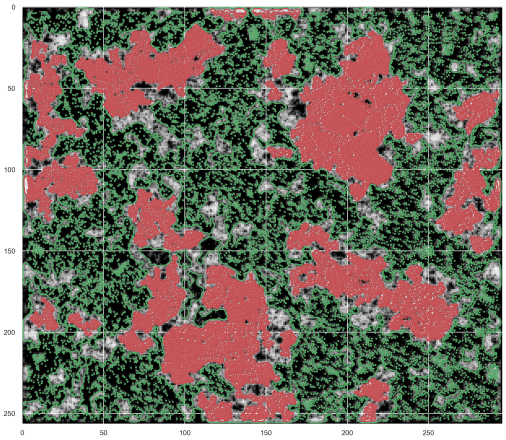

Figure 5.9: Particles in the BD simulation snapshot labeled dense (red) or dilute (green) based on the contour they are encased by from Fig. 5.8 shown overtop a grayscale representation of the filtered image in Fig. 5.6.

ensuring a large contrast difference, we have avoided the ambiguity presented by the interface between the two phases. Also, we avoid rapidly fluctuating regions by using minimum values for contour size. The particle labels are then saved and these can be used as additional training data for our deep learning model mentioned in section 5.4.

References

[1] S. C. Takatori and J. F. Brady, "Towards a thermodynamics of active matter", en, Physical Review E **91**, 032117 (2015).

[2] D. Levis, J. Codina, and I. Pagonabarraga, "Active Brownian equation of state: metastability and phase coexistence", Soft Matter **13**, 8113–8119 (2017).

[3] A. Patch, D. Yllanes, and M. C. Marchetti, "Kinetics of motility-induced phase separation and swim pressure", Physical Review E **95**, 1–9 (2017).

[4] J. Stenhammar, D. Marenduzzo, R. J. Allen, and M. E. Cates, "Phase behaviour of active Brownian particles: The role of dimensionality", Soft Matter **10**, 1489–1499 (2014).

[5] A. Wysocki, R. G. Winkler, and G. Gompper, "Cooperative motion of active Brownian spheres in three-dimensional dense suspensions", EPL **105** (2014).

[6] Y. Fily and M. C. Marchetti, "Athermal Phase Separation of Self-Propelled Particles with No Alignment", Physical Review Letters **108**, 235702 (2012).

[7] B. Partridge and C. F. Lee, "Critical motility-induced phase separation belongs to the Ising universality class", Physical Review Letters **123**, 068002 (2018).

[8] J. T. Siebert, F. Dittrich, F. Schmid, K. Binder, T. Speck, and P. Virnau, "Critical behavior of active Brownian particles", Physical Review E **98** (2018).

[9] A. R. Dulaney, S. A. Mallory, and J. F. Brady, "The "isothermal" compressibility of active matter",
A.R.D. participated in the conception of the project, performed the calculations, analyzed the data, and participated in the writing of the manuscript. (2020),

[10] M. Herrero, J. A. Mendiola, A. Cifuentes, and E. Ibáñez, *Supercritical fluid extraction: Recent advances and applications*, Apr. 2010.

[11] E. Kiran, P. G. Debenedetti, and C. J. Peters, eds., *Supercritical Fluids* (Springer Netherlands, Dordrecht, 2000).

[12] G. Brunner, "Applications of Supercritical Fluids", Annual Review of Chemical and Biomolecular Engineering **1**, 321–342 (2010).

[13] D. Bolmatov, V. V. Brazhkin, and K. Trachenko, "Thermodynamic behaviour of supercritical matter", Nature Communications **4**, 1–7 (2013).

[14] H. E. Stanley, *Introduction to Phase Transitions and Critical Phenomena* (Oxford University Press, 1971).

[15] M. Y. Ha, T. J. Yoon, T. Tlusty, Y. Jho, and W. B. Lee, "Widom Delta of Supercritical Gas-Liquid Coexistence", Journal of Physical Chemistry Letters **9**, 1734–1738 (2018).

[16] A. R. Dulaney and J. F. Brady, "Machine Learning for Phase Behavior in Active Matter Systems",
A.R.D. participated in the conception of the project, developed the models, analyzed the data, and participated in the writing of the manuscript. (2020),

[17] M. Y. Ha, T. J. Yoon, T. Tlusty, Y. Jho, and W. B. Lee, "Widom Delta of Supercritical Gas-Liquid Coexistence", Journal of Physical Chemistry Letters **9**, 1734–1738 (2018).

[18] V. V. Brazhkin, Y. D. Fomin, A. G. Lyapin, V. N. Ryzhov, and E. N. Tsiok, "Widom line for the liquid-gas transition in Lennard-Jones system", Journal of Physical Chemistry B **115**, 14112–14115 (2011).

[19] V. V. Brazhkin, Y. D. Fomin, V. N. Ryzhov, E. E. Tareyeva, and E. N. Tsiok, "True Widom line for a square-well system", Physical Review E **89**, 042136 (2014).

[20] P. F. McMillan and H. E. Stanley, "Going supercritical", Nature Physics **6**, 479–480 (2010).

[21] G. G. Simeoni, T. Bryk, F. A. Gorelli, M. Krisch, G. Ruocco, M. Santoro, T. Scopigno, D. Bolmatov, V. V. Brazhkin, and K. Trachenko, "The Widom line as the crossover between liquid-like and gas-like behaviour in supercritical fluids", Nature Physics **6**, 503–507 (2010).

[22] S. C. Takatori and J. F. Brady, "A theory for the phase behavior of mixtures of active particles", Soft Matter **11**, 7920–7931 (2015).

[23] S. C. Takatori, W. Yan, and J. F. Brady, "Swim Pressure: Stress Generation in Active Matter", en, Physical Review Letters **113**, 028103 (2014).

[24] D. Stopper, H. Hansen-Goos, R. Roth, and R. Evans, "On the decay of the pair correlation function and the line of vanishing excess isothermal compressibility in simple fluids", Journal of Chemical Physics **151** (2019).

[25] J. Bruna, W. Zaremba, A. Szlam, and Y. LeCun, "Spectral Networks and Locally Connected Networks on Graphs", (2013).

[26] M. Defferrard, X. Bresson, and P. Vandergheynst, "Convolutional Neural Networks on Graphs with Fast Localized Spectral Filtering", Advances in Neural Information Processing Systems, 3844–3852 (2016).

[27] B. Xu, J. Huang, L. Hou, H. Shen, J. Gao, and X. Cheng, "Label-Consistency based Graph Neural Networks for Semi-supervised Node Classification", SIGIR 2020 - Proceedings of the 43rd International ACM SIGIR Conference on Research and Development in Information Retrieval, 1897–1900 (2020).

[28] P. Veličković, A. Casanova, P. Liò, G. Cucurull, A. Romero, and Y. Bengio, "Graph attention networks", in 6th international conference on learning representations, iclr 2018 - conference track proceedings (Oct. 2018).

[29] V. Ramasubramani, B. D. Dice, E. S. Harper, M. P. Spellings, J. A. Anderson, and S. C. Glotzer, “freud: A Software Suite for High Throughput Analysis of Particle Simulation Data”, Computer Physics Communications **254** (2019).

[30] A. Stukowski, “Visualization and analysis of atomistic simulation data with OVITO-the Open Visualization Tool”, Modelling and Simulation in Materials Science and Engineering **18**, 015012 (2010).

Chapter 6

MACHINE LEARNING THE INTERFACE IN PHASE SEPARATING ACTIVE MATTER

The novel swim pressure, while not a true pressure, is still critical for determining the phase behavior of active Brownian particles (ABPs). In this chapter, we present a mechanical argument highlighting that there is a jump in fluid pressure at the phase interface of phase-separated ABPs, and we show that this pressure gradient is balanced by the increase in swim pressure measured at the interface. We present the initial steps in providing evidence for the importance of the interface. Using machine learning we have shown that it is possible to predict whether a particle is a part of the interface or either bulk phase. By classifying particles in the system as such, it becomes possible to compute the particle phase pressure difference between the bulk phases and the increase in swim pressure at the interface. We conclude this chapter by discussing ideas for future works and further extensions into the application of machine learning for active systems.

6.1 Introduction

Phase behavior in active matter systems has been a prominent area of research over the past decade with a growing body of computational and theoretically driven work [1–12]. While the interest in developing a full nonequilibrium thermodynamic framework to describe these systems remains a primary area of focus [11, 13, 14], many have opted to focus strictly on mechanics as a means to characterize these behaviors [4, 15–17]. The well-defined forces, stresses, and dynamics present can be readily computed even if the systems lie far from equilibrium. The active pressure being a large contributor to much of the understanding of these systems [15, 18, 19], by describing the instability of expanding bacterial droplets [20], the stability criteria for the motility-induced phase separation [4, 12, 21], and the partitioning in confined active matter [22]. However, the use of the active pressure was found to give a strongly negative surface tension between stable coexisting phases [16, 23]. This oddity led to the current understanding, that the novel swim pressure—a portion of the active pressure—does not behave like a "true" pressure [17], even though active particles exert a greater pressure on boundaries than their passive counterparts.

In this chapter, I discuss the importance of the swim pressure for understanding phase-separating active systems and show how it behaves like a typical pressure in certain contexts of coexistence. This chapter is outlined as follows. In section 6.2, we demonstrate—using mechanical arguments—how the swim pressure enters into the coexistence criterion at the phase interface. In section 6.3, we discuss the machine learning framework used to validate our mechanical perspective, which predicts whether a particle is contributing to the dilute or dense phase or the interface. We follow up in section 6.4 by showing our predictions for particle labels and discussing how these labels allow us to compute the pressure independently in the bulk phases or at the phase boundary. Finally, in section 6.5, we discuss our ongoing work towards determining the role of the swim pressure in describing phase behavior in active systems and outline future directions in which we can take the research presented in this thesis.

6.2 Swim Pressure at the Interface

For two phases to coexist they must be at mechanical equilibrium, meaning the pressure in each phase must be equal. The phase pressures can be written as $P_i = p^i_f + \Pi^i_p$ for $i = l, g$, where p^i_f is the fluid pressure in phase i, Π^i_p is the particle pressure of phase i, and l and g denote the liquid and gas phases, respectively.

The particle pressure $\Pi_p^i = nk_BT + \Pi_p^{col}$ is the sum of the osmotic and collisional pressures. For systems at equilibrium, we know that the chemical potential of the fluid in each phase must be equal, which forces the fluid pressure of each phase to be equal, leaving just the particle phase pressures to be balanced in our mechanical equilibrium constraint. However, if the suspension is active, then there is a jump in polar order at the phase boundary, causing a jump in the swim pressure. This jump in swim pressure must be balanced by a jump in the fluid pressure to prevent net fluid flow from the dense phase.

The mechanical reasoning for this fluid pressure increase is as follows. At low Reynolds number, conservation of mass is given by the continuity equation $\nabla \cdot \mathbf{u} = 0$, where $\mathbf{u} = \mathbf{u}_p\phi + \mathbf{u}_f(1-\phi)$ is the velocity of the suspension, $\mathbf{u}_p$ and $\mathbf{u}_f$ are the velocities of the particle and fluid phases, respectively, and ϕ is the volume fraction of the particle phase. Conservation of momentum in the suspension gives $\nabla \cdot \boldsymbol{\sigma} = 0$, where the stress $\boldsymbol{\sigma} = \boldsymbol{\sigma}^f + \boldsymbol{\sigma}^p$ is a sum of the fluid stress and particle stress. The fluid stress $\boldsymbol{\sigma}^f = -p_f\mathbf{I}$ can be written in terms of the fluid phase pressure. The particle phase stress $\boldsymbol{\sigma} = -nk_BT\mathbf{I} - n\langle \mathbf{x}\mathbf{F}^p \rangle$ comes from the osmotic pressure and interparticle or collisional stress (given as the first moment of the interparticle force), where $\langle ... \rangle$ is an average over particles in the suspension. Next, we can look at the conservation equation for the number density. We can start by writing a Smoluchowski equation describing the evolution of probability density for particle positions $P(\mathbf{x}, \mathbf{q})$ in position and orientation space at steady state

$$\begin{aligned} \nabla \cdot \mathbf{j}_T + \nabla_R \cdot \mathbf{j}_R &= 0, \\ \mathbf{j}_T = \mathbf{u}P + U_0\mathbf{q}P + \mathbf{u}P - D_T\nabla P, \\ \mathbf{j}_R &= -D_R\nabla_R P. \end{aligned} \tag{6.1}$$

Here, U_0 is the intrinsic swim speed, D_T is the translational thermal diffusivity, D_R is the rotational diffusivity, and $\nabla_R = \mathbf{q} \times \nabla_q$ is the appropriate rotational gradient operator. Averaging Eq. (6.1) over orientations gives a conservation equation for the number density n

$$\begin{aligned} \nabla \cdot \mathbf{j}_n &= 0, \\ \mathbf{j}_n = \mathbf{u}n + U_0\mathbf{m} - D_T\nabla n, \end{aligned} \tag{6.2}$$

where $\mathbf{j}_n$ is the number density flux and $\mathbf{m} = \int \mathbf{qq} P \, d\mathbf{q}$ is the polar order. Multiplying $P(\mathbf{x}, \mathbf{q})$ by $\mathbf{q}$ and integrating gives the polar order conservation equation

$$\begin{aligned} \nabla \cdot \mathbf{j}_m + d(d-1) D_R \mathbf{m} &= 0, \\ \mathbf{j}_m = \mathbf{um} + U_0 \mathbf{Q} + \frac{U_0}{d} n\mathbf{I} - D_T \nabla \mathbf{m}, & \end{aligned} \tag{6.3}$$

where $\mathbf{j}_m$ is the polar order flux, d is the number of rotational dimensions, and $\mathbf{Q} = \int [\mathbf{qq} - (1/d)\mathbf{I}] P \, d\mathbf{q}$ is the nematic order tensor.

There is no net flux of particles or fluid across the phase boundary, giving $\mathbf{j}_n = 0$. Now, if we rewrite $D_T \nabla n$ in terms of the particle stress we have $0 = \mathbf{u}n + U_0 \mathbf{m} + (1/\zeta) \nabla \cdot \boldsymbol{\sigma}^p$, where ζ is the translational drag coefficient. Solving for $\mathbf{m}$ in Eq. (6.3) we get $\mathbf{m} = -1/[(d-1)D_R] \nabla \cdot \mathbf{j}_m$, which can be substituted into our number density flux. The contribution from the fluid drops to zero because there is no net fluid flux. The resulting flux expression is

$$\begin{aligned} 0 &= \frac{1}{\zeta} \left(\nabla \cdot \boldsymbol{\sigma}^p - \frac{\zeta U_0 \tau_R}{d(d-1)} \nabla \cdot \mathbf{j}_m \right), \\ &= \frac{1}{\zeta} \nabla \cdot \left(\boldsymbol{\sigma}^p - \frac{\zeta U_0 \tau_R}{d(d-1)} \mathbf{j}_m \right), \end{aligned} \tag{6.4}$$

where $\tau_R = D_R^{-1}$ is the timescale for reorientation. The second term is the swim stress $\boldsymbol{\sigma}^{swim} = -\zeta U_0 \tau_R / [d(d-1)] \mathbf{j}_m$.

Combining the suspension stress balance with the flux expression from the number density conservation, we get the following:

$$\begin{aligned} 0 &= \nabla \cdot \boldsymbol{\sigma}, \\ &= \nabla \cdot (\boldsymbol{\sigma}^f + \boldsymbol{\sigma}^p), \\ &= \nabla \cdot (\boldsymbol{\sigma}^f - \boldsymbol{\sigma}^{swim}), \end{aligned} \tag{6.5}$$

which is rewritten to give

$$\begin{aligned} \nabla \cdot \boldsymbol{\sigma}^f &= \nabla \cdot \boldsymbol{\sigma}^{swim}, \\ -\nabla p_f &= \nabla \cdot \boldsymbol{\sigma}^{swim}, \\ \nabla p_f &= \nabla \Pi^{swim}, \end{aligned} \tag{6.6}$$

where Π^{swim} is the swim pressure [4, 18]. Thus, we see that the gradient in swim pressure is balanced by a gradient in the fluid pressure in the opposite direction to prevent the net flux of fluid. Our mechanical equilibrium constraint can then be written as

$$\begin{aligned} P_l &= P_g, \\ p_f^l + \Pi_p l &= p_f^g + \Pi_p^g, \\ (\Pi_p^l - \Pi_p^g) &= -(p_f^l - p_f^g), \\ \nabla \Pi_p &= -\nabla p_f, \\ \nabla \Pi_p &= -\nabla \Pi^{swim}, \\ \Pi_p^l + \Pi^{swim,l} &= \Pi_p^g + \Pi^{swim,g}, \\ \Pi^{act,l} &= \Pi^{act,g}. \end{aligned} \tag{6.7}$$

Now we have that the active pressure must be equal in both phases. However, Omar et al. [17] showed that the swim pressure is not a *true pressure*, meaning that it is not a pointwise defined surface force. Instead, we know that swim pressure arises from the self-generated active force density on a particle. Our mechanical balance then implies that this large surface force density must be balanced by the particle phase pressure difference between the two bulk phases.

6.3 Multi-phase Machine Learning Model

To determine if this force density does balance the difference in bulk phase pressures, we must find a way to determine whether a particle is contributing to the interface or not. We turn towards machine learning as it has proven to be a useful tool in determining the local state of particles in simulation [24, 25]. We will follow a similar procedure to that done in [25], but we will be solving a multi-class classification learning problem as opposed to a binary classification problem. Our objective will be to label particles as belonging to the dense or dilute phase or the interface.

Learning Framework

As we are attempting to predict three separate labels, we have chosen to use the cross-entropy loss function, a generalization of the binary cross-entropy loss defined by Eq. (4.3). The loss is written as

$$L = -\sum_{c=1}^{M} y_{o,c} \ln p_{o,c}, \tag{6.8}$$

where M is the total number of classes (three in our case), $y_{o,c}$ is a binary indicator determining if c is the correct class for observation o, and $p_{o,c}$ is the predicted probability of observation o being of class c.

We frame this problem as a supervised learning problem, as was done in previous chapters. However, we have not yet attempted the use of graph neural networks (GNNs) for this classification problem. We expect the addition of a GNN to have no loss in performance from the additional class label as they have shown excellent ability to handle highly multi-labeled systems [26–29]. Our initial model is a boosted random forest comprised of 90 predictors for 15 boosting rounds created using the XGBoost software package [30]. Though our boosted random forest currently outperforms our neural networks, we have yet to perform any hyperparameter optimizations for our neural network as of yet.

Particle Features and Data Sets

The features used in this work are identical to those used in Chapters 4 and 5, with one additional feature. As we are adding another class to predict—and it is very similar to the other two classes—it is useful to add a feature that helps isolate the third class. While the addition of such a feature is not necessary, it does increase prediction accuracy dramatically. As such, we have added the correlation between the particle orientation and the spatial gradient of the number density $\mathbf{q} \cdot \nabla n$. This feature isolates the interface particles as there is a noticeable increase in density across the interface, whereas the density is fairly homogeneous out in the bulk of either phase. Particles facing into the phase boundary will have positive values of $\mathbf{q} \cdot \nabla n$, while those pointing out will have negative values. This provides a way to distinguish between particles actively swimming into the boundary and those that are about to leave. A schematic of the different cases is presented in Fig. 6.1.

To compute this order parameter we first need to approximate the density gradient throughout the system. We start by computing the Voronoi number density of each particle averaged with its first shell neighbors. Using the first-shell average smooths out small fluctuations that are present from momentary particle collisions, as this parameter must be computed for each time step. We then generate a two-dimensional spline of the averaged number densities using a radial basis function interpolation,

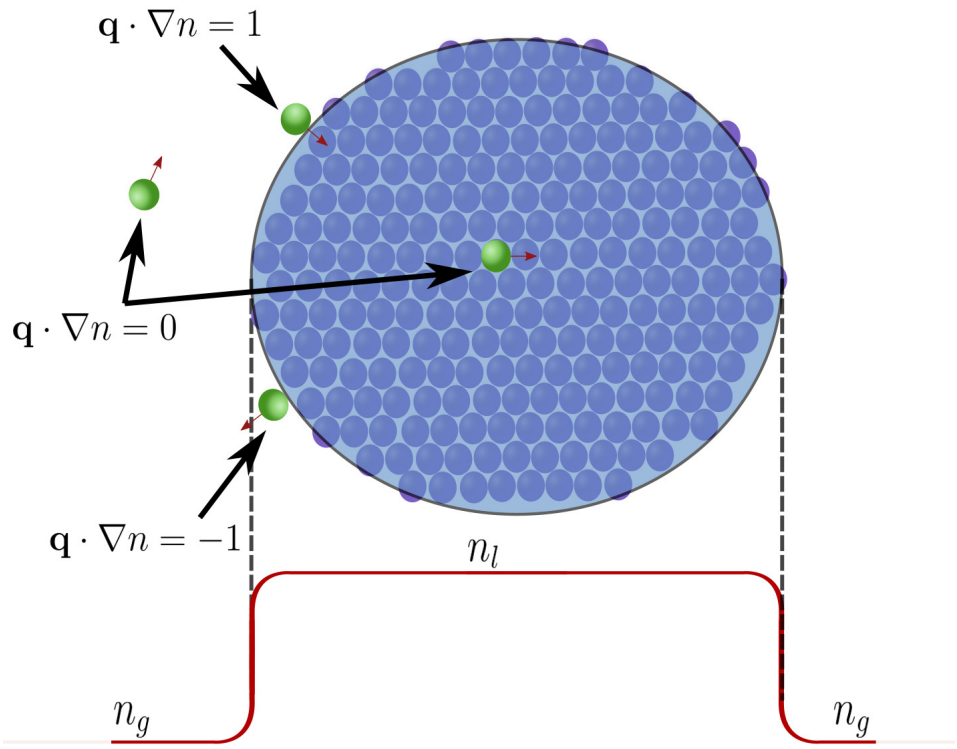

Figure 6.1: Schematic of active Brownian particles in the dilute region (white space), at the phase boundary (shown by a black outline), or in the dense phase (blue). The value of $\mathbf{q} \cdot \nabla n$ is given for each particle shown in green. The red line represents the density profile as one moves from the dilute phase to the center of the dense phase and back out.

taking the center of mass of each particle to be the location for its density value. From this continuous approximation for the density we can compute the components of the gradient by taking the difference of the density values at points $\pm\Delta x$ or $\pm\Delta y$ ($n(x + \Delta x, y) - n(x - \Delta x, y)$ and $n(x, y + \Delta y) - n(x, y - \Delta y)$) through a simple finite-difference method, with $\Delta x = \Delta y = 3a$ where a is the radius of a particle.

Similarly to what was described in Chapter 5, we use labeled Brownian dynamic (BD) simulation data of 2-D suspensions of ABPs from different (Pe_R, ϕ) pairs from within the coexistence region, where $Pe_R = a/\ell$ is the reorientation Péclet number, $\ell = U_0\tau_R$ is the persistence length of ABPs, and $\phi = n\pi a^2$ is the packing fraction (see Appendix 6.7 for details of our simulations). The difficulty here is that we need to separate our training and testing data, but we are restricted to the two-phase portion of the active phase diagram. We randomly select 60% of the simulations in the coexistence region to be used for training, 20% to be used for

validation, and the remaining 20% for testing. Once we have split the simulations into these categories, we record which belongs to each to maintain consistency during our modeling process. Fortunately, we are also able to use data outside of coexistence as additional training points for dilute and dense phase particles. It is important to consider the distribution of the labeled phases present in our training and validation data. If the distribution of labels is unbalanced, then our model may erroneously start to always predict the dominant label or never predict the minority label to reduce the loss function. Since the interface is only present around the bulk phases, we find that our number of interface training points is roughly 1e−3% of the available data we have for either bulk phase. To avoid the issue of unbalanced data we first undersample our majority phases, that is we randomly select a portion of the data to use and throw the rest out. This is not the ideal scenario as it requires wasting much of the data collected. Thus, we also use oversampling to bolster the number of interface points. Oversampling is performed by creating an F-dimensional response surface in feature space (where F is the number of features) of interface particles and interpolating within the space to generate synthetic data points. This is generally a safe method for oversampling the data since the different classes are expected to cluster together in feature space. We only oversample enough data to make 50% of the actual data, ensuring that our collected data is the majority of what is learned.

6.4 Interfacial Prediction

Using the boosted random forest model mentioned in section 6.3, we have obtained initial predictions for particle labels. Figures 6.2, 6.3, 6.4, and 6.5 present the values for our order parameter $\mathbf{q} \cdot \nabla n$ and our initial labels for systems in the dilute phase, dense phase, near the critical point, and deep within the coexistence region, respectively. The dilute and dense predictions (Figs. 6.2 and 6.3, respectively) show that our model is capable of predicting the bulk phases even though the number of possible classes has increased.

As activity increases just beyond the critical point, we see our model starts predicting interfacial particles (see Fig. 6.4). For the homogeneous cases our interface-specific feature looked fairly homogeneous, but once the system phase separates the interface feature appears to outline all of the dense phase clusters. This trend is very clearly learned, as the interface (red) predicted particles only appear around the dense phase.

Looking now at the interfacial feature for a strongly phase-separated system (see Fig. 6.5 (left)) we see that the positive values form a shell around the dense phase—

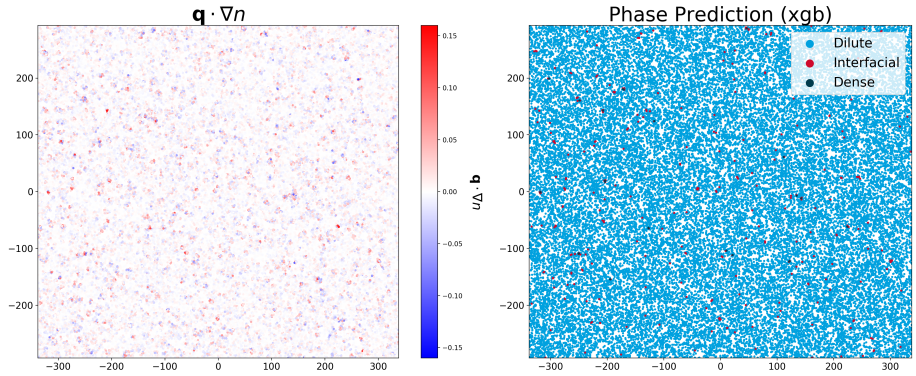

Figure 6.2: The $\mathbf{q} \cdot \nabla n$ correlation (left) and phase predictions (right) for a representative BD simulation at $Pe_R = 0.045$ and $\phi = 0.1$.

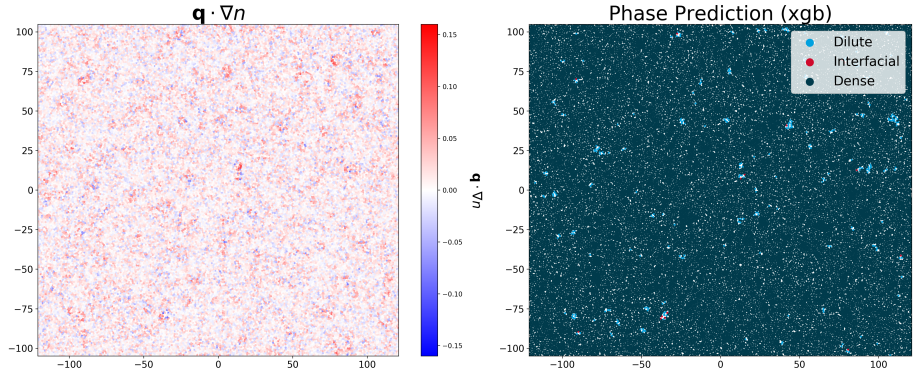

Figure 6.3: The $\mathbf{q} \cdot \nabla n$ correlation (left) and phase predictions (right) for a representative BD simulation at $Pe_R = 0.5$ and $\phi = 0.78$.

as we saw for the weakly phase-separated system—but the shell is multiple particles thick. From the predictions in Fig. 6.5 (right), it is clear that the dense and dilute phase are well predicted, but the interface appears to be underrepresented. The shell of interfacial particles predicted around the dense phase is not continuous around the entire dense cluster.

It is clear that the lack of well-labeled interface particles is contributing to the failed predictions for this class. As such, we propose adding a time-dependent labeling scheme that involves looking at particle positions one time step before and after the frame of interest to determine if a particle remains at the interface or not. This should increase the number of labeled interface particles. Since we know the swim pressure is caused by the net polar order at the boundary, it would also be helpful to use local approximations for the polar order as an additional feature for use in prediction. The goal is to capture the entire interface and not just the external

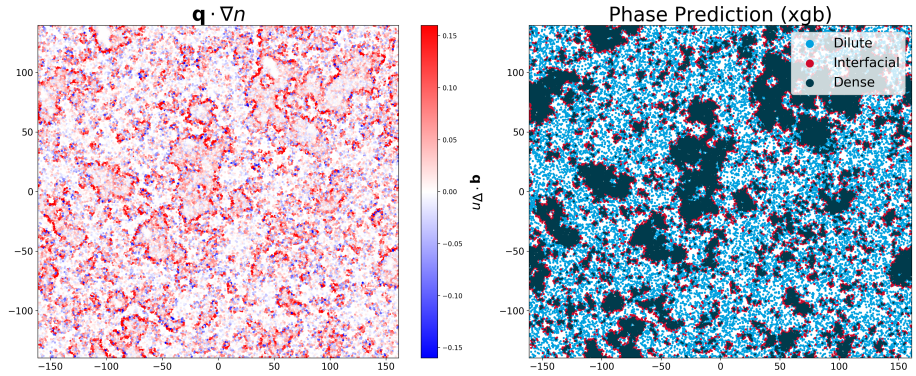

Figure 6.4: The $\mathbf{q} \cdot \nabla n$ correlation (left) and phase predictions (right) for a representative BD simulation at $Pe_R = 0.036$ and $\phi = 0.44$.

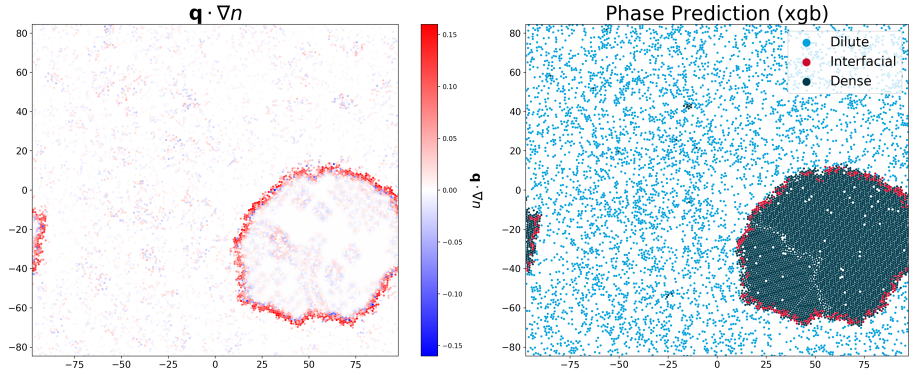

Figure 6.5: The $\mathbf{q} \cdot \nabla n$ correlation (left) and phase predictions (right) for a representative BD simulation at $Pe_R = 0.01$ and $\phi = 0.3$.

particles in contact with the dilute phase.

6.5 Conclusion

We have presented a mechanical argument for the necessary inclusion of the swim pressure when determining phase behavior in repulsive ABPs. From this perspective, we have shown that even though we broadly neglect the fluid, it must be considered as active particles continue to apply a force on the fluid even if they are not moving. (Similarly, active particles moving on a substrate, or dry active matter, would continue to apply a traction force on the substrate). Thus, the jump in swim pressure at the phase boundary must be balanced by a fluid pressure jump to prevent a net flux of fluid from one phase into another.

We have presented our initial effort for providing evidence about the importance of the swim pressure at the interface. Our initial machine learning model is capable of

predicting which particles are a part of the phase interface but still under predicts this group (even for strongly phase-separated systems). The next steps for this work in progress include refining this model using more sophisticated methods for labeling training data and adding local structure into the model through the application of graph neural networks (as was done in Chapters 4 and 5). Once we have a confident model, we can compute the pressure from particles in either bulk phase and compare their difference to the swim pressure measured in the interface.

6.6 Future Directions

The works presented in this thesis have laid a sturdy foundation upon which we can build. The majority of our work involving machine learning has revolved around making predictions at the particle level for the simplest case of phase separation in ABPs. As such, we have neglected certain aspects in our considerations that can be added. One such aspect is the inclusion of the hexatic transition. Two dimensional hard disks undergo a continuous, crystalline phase transition driven by geometric constraints. Once the system has become dense enough ($\phi \sim 0.71$), a crystalline transition is seen forming a hexatic phase. This transition exists in active hard disks as well. Some have included this transition in the construction of active phase diagrams [31], but it is widely neglected. Adding such a transition would require a machine learning model to learn the density-driven separation as well as an order-disorder transition. Evidence to support this undertaking is presented in Chapter 4 by the learned importance of the third-shell Voronoi densities, which serve as a proxy for the third shell in the radial distribution function.

In a similar vein, we can attempt to recreate this work for polydisperse systems. With roughly 10% polydispersity, the hexatic transition does not occur. This would provide a much cleaner representation of the dense branch of the MIPS binodal. This also brings about an interesting challenge in that the densities—one of the most informative features—are explained by an additional distribution as the particle radius can vary. This variance also mildly affects the interparticle interactions, but this is unlikely to cause much issue.

Lastly, we can approach the problem of phase separation at the system level as opposed to the particle level. We currently use graph neural networks to make node-level predictions, but we could as easily use them to predict labels for entire graphs. Therefore, it should prove possible to—in an unsupervised framework—predict whether a graph represents a homogeneous dilute, homogeneous dense, or

phase-separated system. Graph neural networks generalize well for unsupervised graph-level predictions [29] and can be used on graphs of different sizes. Once predictions are made for each of the regions of the phase diagram, a clustering algorithm can be used to determine the breakdown of the phases, which completely avoids the labeling issue presented earlier in this chapter. This formulation can even be adapted to an online learning structure where the clustering is adapted as more data points are added. Allowing one to build the phase diagram incrementally as data is acquired.

Appendix

6.7 Simulation Details

We simulate overdamped active Brownian particles. Each particle of radius a exerts a self-propulsive force $\mathbf{F}^{swim} = \zeta U_0 \mathbf{q}$ to move at speed U_0 in a direction $\mathbf{q}$ through a medium with resistance ζ. These particles undergo random reorientations via a stochastic torque $\mathbf{L}^R$ on a timescale τ_R. Particles interact with each other through a repulsive Weeks-Chandler-Anderson (WCA) potential with a cutoff distance $r_cut = (2a)2^(1/6)$ and potential depth of $\epsilon = 200aF^{swim}$. The equations of motion are given by the Langevin equations

$$0 = -\zeta \mathbf{U}_i + \mathbf{F}_i^{swim} + \mathbf{F}_i^P, \tag{6.9}$$

$$0 = -\zeta_R \mathbf{\Omega}_i + \mathbf{L}_i^R, \tag{6.10}$$

where $\mathbf{U}_i$ is the speed of particle i, $\mathbf{F}^P = \sum_{j \neq i} \mathbf{F}_{ij}^{wca}$ is the interparticle force given by the sum of the pairwise WCA forces for of all particles j on particle i, ζ_R is the resistance from the medium against rotations, and $\mathbf{\Omega}_i$ is the angular velocity. The angular velocity is related to particle orientations via $\partial \mathbf{q}_i / \partial t = \mathbf{\Omega}_i \times \mathbf{q}_i$. The stochastic torque is zero mean and has variance $2\zeta_R^2 \delta(t)/\tau_R$.

References

[1] F. Ginelli, F. Peruani, M. Bär, and H. Chaté, "Large-scale collective properties of self-propelled rods", Physical Review Letters **104**, 1–4 (2010).

[2] Y. Fily and M. C. Marchetti, "Athermal Phase Separation of Self-Propelled Particles with No Alignment", Physical Review Letters **108**, 235702 (2012).

[3] J. Palacci, S. Sacanna, A. P. Steinberg, D. J. Pine, and P. M. Chaikin, "Living Crystals of Light-Activated Colloidal Surfers", en, Science **339**, 936–940 (2013).

[4] S. C. Takatori and J. F. Brady, "Towards a thermodynamics of active matter", en, Physical Review E **91**, 032117 (2015).

[5] A. Wysocki, R. G. Winkler, and G. Gompper, "Cooperative motion of active Brownian spheres in three-dimensional dense suspensions", EPL **105** (2014).

[6] J. Stenhammar, D. Marenduzzo, R. J. Allen, and M. E. Cates, "Phase behaviour of active Brownian particles: The role of dimensionality", Soft Matter **10**, 1489–1499 (2014).

[7] V. Prymidis, S. Paliwal, M. Dijkstra, and L. Filion, "Vapour-liquid coexistence of an active Lennard-Jones fluid", The Journal of Chemical Physics **145**, 124904 (2016).

[8] B. van der Meer, V. Prymidis, M. Dijkstra, and L. Filion, "Predicting the phase behavior of mixtures of active spherical particles", The Journal of Chemical Physics **152**, 144901 (2020).

[9] D. Levis, J. Codina, and I. Pagonabarraga, "Active Brownian equation of state: metastability and phase coexistence", Soft Matter **13**, 8113–8119 (2017).

[10] S. Chakraborti, S. Mishra, and P. Pradhan, "Additivity, density fluctuations, and nonequilibrium thermodynamics for active Brownian particles", Physical Review E **93**, 052606 (2016).

[11] T. Speck, "Stochastic thermodynamics for active matter", Epl **114** (2016).

[12] S. Paliwal, J. Rodenburg, R. Van Roij, and M. Dijkstra, "Chemical potential in active systems: Predicting phase equilibrium from bulk equations of state?", New Journal of Physics **20**, 015003 (2018).

[13] C. Nardini, É. Fodor, E. Tjhung, F. van Wijland, J. Tailleur, and M. E. Cates, "Entropy Production in Field Theories without Time-Reversal Symmetry: Quantifying the Non-Equilibrium Character of Active Matter", Physical Review X **7**, 021007 (2017).

[14] D. Mandal, K. Klymko, and M. R. DeWeese, "Entropy Production and Fluctuation Theorems for Active Matter", Physical Review Letters **119**, 1–6 (2017).

[15] A. P. Solon, Y. Fily, A. Baskaran, M. E. Cates, Y. Kafri, M. Kardar, and J. Tailleur, "Pressure is not a state function for generic active fluids", Nature Physics **11**, 673–678 (2015).

[16] A. Patch, D. M. Sussman, D. Yllanes, and M. C. Marchetti, "Curvature-dependent tension and tangential flows at the interface of motility-induced phases", Soft Matter **14**, 7435–7445 (2018).

[17] A. K. Omar, Z.-G. Wang, and J. F. Brady, "Microscopic origins of the swim pressure and the anomalous surface tension of active matter", PHYSICAL REVIEW E **101**, 12604 (2020).

[18] S. C. Takatori, W. Yan, and J. F. Brady, "Swim Pressure: Stress Generation in Active Matter", en, Physical Review Letters **113**, 028103 (2014).

[19] A. P. Solon, J. Tailleur, M. E. Cates, J. Stenhammar, M. Kardar, R. Wittkowski, Y. Kafri, M. Kardar, Y. Kafri, M. E. Cates, and J. Tailleur, "Pressure and Phase Equilibria in Interacting Active Brownian Spheres", en, Physical Review Letters **114**, 198301 (2015).

[20] A. Sokolov, L. D. Rubio, J. F. Brady, and I. S. Aranson, "Instability of expanding bacterial droplets", en, Nature Communications **9**, 1322 (2018).

[21] A. P. Solon, J. Stenhammar, M. E. Cates, Y. Kafri, and J. Tailleur, "Generalized thermodynamics of phase equilibria in scalar active matter", Physical Review E **97**, 020602 (2018).

[22] C. M. Kjeldbjerg and J. F. Brady, "Theory for the Casimir effect and the partitioning of active matter", Soft Matter (2020).

[23] J. Bialké, J. T. Siebert, H. Löwen, and T. Speck, "Negative Interfacial Tension in Phase-Separated Active Brownian Particles", (2015).

[24] M. Y. Ha, T. J. Yoon, T. Tlusty, Y. Jho, and W. B. Lee, "Widom Delta of Supercritical Gas-Liquid Coexistence", Journal of Physical Chemistry Letters **9**, 1734–1738 (2018).

[25] A. R. Dulaney and J. F. Brady, "Machine Learning for Phase Behavior in Active Matter Systems",
A.R.D. participated in the conception of the project, developed the models, analyzed the data, and participated in the writing of the manuscript. (2020),

[26] T. N. Kipf and M. Welling, "Semi-Supervised Classification with Graph Convolutional Networks", (2016).

[27] P. Veličković, A. Casanova, P. Liò, G. Cucurull, A. Romero, and Y. Bengio, "Graph attention networks", in 6th international conference on learning representations, iclr 2018 - conference track proceedings (Oct. 2018).

[28] J. Zhang, X. Shi, J. Xie, H. Ma, I. King, and D.-Y. Yeung, *GaAN: Gated Attention Networks for Learning on Large and Spatiotemporal Graphs*, tech. rep. ().

[29] Z. Wu, L. Li, Y. Yang, P. Hu, Y. Li, S.-Y. Yang, L. V. Wang, and W. Gao, "A microrobotic system guided by photoacoustic computed tomography for targeted navigation in intestines in vivo", Science Robotics **4**, eaax0613 (2019).

[30] T. Chen and C. Guestrin, "XGBoost: A scalable tree boosting system", in Proceedings of the acm sigkdd international conference on knowledge discovery and data mining, Vol. 13-17-August-2016 (Aug. 2016), pp. 785–794.

[31] J. U. Klamser, S. C. Kapfer, and W. Krauth, "Thermodynamic phases in two-dimensional active matter", Nature Communications **9** (2018).